NICOLAUS COPERNICUS UNIVERSITY IN TORUŃ
FACULTY OF PHYSICS, ASTRONOMY AND INFORMATICS

Neurotoxic ligands interactions with insects membrane proteins

Beata Niklas

Dissertation for a doctoral degree

Supervisors:
Prof. Bruno Lapied
Prof. dr hab. Wiesław Nowak

Toruń 2023

European Funds
Knowledge Education Development

European Union
European Social Fund

Acknowledgments

At the very beginning, I would like to thank my Supervisors, Prof. Wiesław Nowak and Prof. Bruno Lapied, for their endless support and for pushing me to dive deep into science. Due to their kindness, patience, and smile that brightened even the hardest day, doing research was not as scary as it could be but it was rather an amazing adventure. I am immensely grateful for all relevant comments and for the fact that I could always count on professors' help.

I could not forget to thank all members of the Theoretical Biophysics Group for their eagerness to give me countless directions, and to my co-authors, Prof. Maria Stankiewicz and Dr. Milena Jankowska, for their contribution and the friendliest atmosphere I could dream of.

I would also like to thank the National Science Centre (under grants no. 2016/23/B/ST4/01770 and 2021/41/N/NZ3/02165) for their financial support and both the Centre of Informatics Tricity Academic Supercomputer & Network (CI TASK) and the Interdisciplinary Centre for Mathematical and Computational Modeling (ICM) for providing computer facilities to conduct my research. This work was also supported by the project POWR.03.05.00–00-Z302/17 Universitas Copernicana Thoruniensis in Futuro-IDS "Academia Copernicana".

Finally, I would like to express my deepest gratitude to my mother, who was always there for me, with whom I could share not only moments of joy and satisfaction but also my worries, doubts, and frustrations.

Table of contents

1. List of abbreviations

AS – allosteric site

ASA – solvent accessible surface area

BSA – buried surface area

cryo-EM – cryo-electron microscopy

CC – central cavity

CV – collective variables

DCJW – N-decarbomethoxyllated JW062

DDT – dichlorodiphenyltrichloroethane

ECL – extracellular loop

GPCR – G protein-coupled receptor

ICL – intracellular loop

IG – inactivation gate

kdr – knockdown resistance

mAChR – muscarinic acetylcholine receptor

MD – molecular dynamics

NAG – N-acetylglucosamine

NAM – negative allosteric modulator

OS – orthosteric site

PAM – positive allosteric modulator

PD – ion-conducting pore domain

PDB – Protein Data Bank

P-loop – pore loop

RMSD – root mean square deviation

RRCS – residue-residue contact score

SCBI – sodium channel blocker insecticide

SSF – smina scoring function

VGSC – voltage-gated sodium channel

VSD – voltage sensor domain

WHO – The World Health Organization

WT – wild type

2. Abstract of the doctoral thesis entitled: “Neurotoxic ligands interactions with insects membrane proteins”

Mosquitoes and other insects spread a number of dangerous diseases, including malaria, denga, or yellow fever, and the increasing range of their occurrence due to climate change poses a growing threat. Insects also destroy approximately 20% of crop yields, which poses a tremendous challenge in ensuring the food security of the growing world's population. The main method of limiting the spread of pest insects is the use of repellents and insecticides that interact with the nervous system proteins. However, commonly used chemicals lose their efficacy due to the growing resistance. Therefore, it is necessary to understand the molecular mechanisms of action of the available chemicals and the resistance to them to develop new methods of insect control.

The aim of this study was to perform a detailed analysis of the physicochemical interactions between selected neurotoxic ligands and two target proteins: (1) muscarinic receptors, responsible for recognizing olfactory stimuli, and (2) voltage-gated sodium channels, which play a crucial role in neural conduction and are a molecular target of the most commonly used insecticides. The results are presented in three articles included in the doctoral thesis.

Firstly, using computer simulations of docking and molecular dynamics on a scale of hundreds of nanoseconds, we contributed to expanding the knowledge of allosteric pathways of structural signal propagation in the muscarinic receptor (Article I). Ligand binding induces the allosteric pathway of conformational changes that correspond to the function of the target protein. The models of insect proteins built in this study, as well as the model of the cell membrane in which they are anchored, enabled the examination of differences in the action of ligands on human and insect receptors, which is crucial for designing selective agents. Additionally, the class of photoactive ligands proposed here can serve as an excellent tool in research on neural conduction.

Secondly, we compared the binding of four peptide toxins from sea anemones to the voltage-gated sodium channel of the cockroach *Periplaneta americana*. The results of molecular modeling are consistent with the electrophysiological experiments presented in Article II. A better understanding of the fast inactivation process and its inhibition by neurotoxins can contribute to the development of selective insecticides, as well as new analgesics.

Finally, based on the analysis of the dissociation pathways of a sodium channel blocker insecticide DCJW, we identified its' entry route into the mosquito channel inner pore. We also explained the role of the mutation causing resistance to this class of neurotoxins, as well as the molecular basis of the increased toxicity of the metabolite compared to the pre-insecticide. We also identified the amino acid residues that constitute the binding site of two groups of insecticides – channel blockers and pyrethroids. Mutations in these residues may be involved in the mechanism of cross-resistance. The results are presented in a form of a preprint to the manuscript that is in review (Article III).

In summary, the results of computer modeling presented in the doctoral thesis significantly broaden the knowledge of the molecular mechanisms of action of repellents and insecticides. Simulations at the scale of individual atoms enabled the examination of the response of target proteins to the binding of neurotoxic ligands, contributing to a better understanding of biophysical processes such as fast inactivation of the voltage-gated sodium channel or activation of muscarinic receptor. These findings may aid in the development of new insecticides and painkillers with improved effectiveness and selectivity.

3. Streszczenie rozprawy doktorskiej pt. „Oddziaływania neurotoksycznych ligandów z białkami błonowymi owadów”

Komary i inne owady roznoszą szereg niebezpiecznych chorób, takich jak malaria, denga, czy żółta febra, a zwiększający się przez zmiany klimatyczne zasięg ich występowania stanowi coraz poważniejsze zagrożenie. Insekty niszczą blisko 20% upraw rolnych, co w kontekście wzrostu liczby ludności i braku dostępnych terenów pod nowe uprawy, stwarza wyzwanie w zapewnieniu bezpieczeństwa żywnościowego wzrastającej liczby ludności. Główną metodą ograniczania rozprzestrzeniania się owadzich szkodników jest stosowanie repelentów i insektycydów – molekuł oddziałujących z białkami układu nerwowego. Powszechnie używane środki chemiczne tracą jednak skuteczność ze względu na postępującą odporność owadów. Konieczne jest więc poznanie mechanizmów molekularnych działania wykorzystywanych neurotoksyn i odporności na nie, by opracować nowe metody kontroli insektów.

Celem badań poznanie natury oddziaływań fizykochemicznych pomiędzy wybranymi neurotoksycznymi ligandami i reprezentantami dwóch klas białek targetowych: (1) receptorami muskarynowymi, odpowiedzialnymi m.in. za rozpoznawanie bodźców zapachowych; (2) bramkowanymi napięciem kanałami sodowymi odgrywającymi kluczową rolę w przewodnictwie nerwowym, stanowiącymi cel molekularny najpowszechniej używanych insektycydów. Do badań wykorzystano metody biofizyki obliczeniowej, metody bioinformatyczne i elektrofizjologiczne. Wyniki przedstawione zostały w formie trzech artykułów, stanowiących główną część rozprawy.

Wiązanie liganda indukuje zmiany konformacyjne odpowiadające za funkcję receptora. Stosując komputerowe symulacje dokowania i dynamiki molekularnej w skali setek nanosekund, przyczyniłam się do poszerzenia wiedzy o allosterycznych ścieżkach propagacji sygnału strukturalnego receptora muskarynowego z rodziny receptorów sprzężonych z białkiem G (Artykuł I). Opracowane przeze mnie modele receptora owadziego i kotwiczącej go owadziej błony komórkowej umożliwiły zbadanie różnic strukturalnych w działaniu ligandów na receptory ludzkie i owadzie, co ma duże znaczenie dla projektowania selektywnych środków. Ponadto podjęłam próbę zaprojektowania nowej klasy fotoaktywnych ligandów odstraszających owady, które mogą stanowić świetne narzędzie w badaniach przewodnictwa nerwowego, umożliwiając jego kontrolę za pomocą fotonów.

Porównałam również sposoby wiązania czterech toksyn peptydowych z ukwiałów do bramkowanego napięciem kanału sodowego karaczana *Periplaneta americana*. Wyniki

modelowania molekularnego są spójne z eksperymentami elektrofizjologicznymi prezentowanymi w Artykule II. Lepsze zrozumienie procesu szybkiej inaktywacji i jego blokowania przez neurotoksyny może przyczynić się do powstania selektywnych insektycydów, a także nowych leków przeciwbólowych.

Na podstawie analizy ścieżek dysocjacji owadobójczego liganda z grupy blokerów kanału sodowego – DCJW – określiłam drogę wejścia insektycydu do miejsca wiązania w kanale komara. Ponadto wyjaśniłam rolę mutacji powodującej odporność na tę klasę neurotoksyn oraz podstawę molekularną zwiększonej toksyczności metabolitu w porównaniu z preinsektycydem. Wyznaczyłam również reszty aminokwasowe stanowiące miejsce wiązania dwóch grup insektycydów – blokerów i pyretroidów, których mutacje mogą być zaangażowane w mechanizm odporności krzyżowej. Wyniki zaprezentowane zostały w formie preprintu manuskryptu, który został wysłany do recenzji (Artykuł III).

Podsumowując, wyniki modelowania komputerowego prezentowane w rozprawie w znaczny sposób pogłębiają wiedzę o mechanizmach molekularnych działania środków odstraszających owady. Symulacje w skali pojedynczych atomów umożliwiły zbadanie odpowiedzi białek targetowych na wiązanie neurotoksycznych ligandów, przyczyniając się do lepszego zrozumienia podstawowych procesów biofizycznych, takich jak szybka inaktywacja kanału sodowego czy aktywacja receptora muskarynowego.

4. Introduction

4.1 Motivation

Arthropod bloodsucking species provide an excellent transportation route for hundreds of viruses, bacteria, protozoa, and helminths between their vertebrate hosts. In the 17th through the early 20th centuries, diseases spread by hematophagous insects were responsible for more human death than all other causes combined [1]. At the turn of the 19th and 20th centuries, upon the discoveries of transmission cycles of most insect-borne diseases, prevention programs aimed at vector elimination were implemented. The effective use of repellents and insecticides contributed greatly to successes in insect control and eradication of vector-borne diseases outside of Africa. However, a number of diseases began to reemerge in the 1970s due to insecticide resistance combined with demographic changes and re-invasion of the species [1]. Nowadays, 68 malaria-endemic countries have confirmed resistance to pyrethroids, the major class of insecticides and the only one used for indoor nets impregnation. Resistance to organochlorines, carbamates and organophosphates, which are used for indoor residual spraying, is also widespread [2]. The World Health Organization (WHO) notes that more than half of the human population is at risk of mosquito-borne diseases. Resistance threatens to significantly increase the incidence of malaria and other vector-borne diseases.

Furthermore, it is estimated that arthropods destroy up to 20% of crops annually. Losses in crop production due to insect pests increase with rising temperatures in all climate models [3]. Meeting the food requirements of the growing human population will be a global challenge this century [4] as nearly all the cultivable land is already cultivated. Thus, crop protection must be improved for future food security.

Insects can also cause structural damage to materials and buildings. Invasive species disrupt the balance of natural ecosystems posing a threat to biodiversity.

Insects are thus the costliest animal group to human society and the development of effective methods to control them is one of the world's most important and urgent needs [4]. However, the development of new chemicals recently plateaued and the negative environmental impact of some insecticides led to their withdrawal from use. Therefore, continued research is needed to improve our understanding of insecticide action and resistance, as well as to develop more sustainable and effective pest management strategies.

In this study, we focus on two targets for neurotoxic agents exerting insecticidal activity: muscarinic acetylcholine receptors and voltage-gated sodium channels. These membrane proteins are described in the 4.2 section.

4.2 Biomolecules studied

4.2.1 G protein-coupled receptors

G protein-coupled receptors (GPCRs), also known as seven transmembrane receptors, are the largest and the most diverse group of membrane proteins in eukaryotes, encoded by over 800 genes in humans [5]. They respond to a great variety of stimuli that include photons, ions, odorants, tastants, vitamins, neurotransmitters, hormones, growth factors, intermediary metabolites, and products from commensal bacteria that are translated into intracellular signals *via* their binding partners such as G proteins or β-arrestins [6]. Acting as signal transducers, GPCRs play a critical role in the regulation of nearly all cellular and physiological processes, thus being the most intensively studied therapeutic target. To this date, nearly 1/3 of all modern drugs act through GPCRs [6, 7].

Based on sequence homology and functional similarity, six main families of GPCRs are distinguished: Class A (rhodopsin-like), Class B (secretin receptor family), Class C (metabotropic glutamate), Class D (fungal mating pheromone receptors), Class E (cyclic AMP receptors) and Class F (frizzled/smoothened). Since classes D and E are not present in vertebrates, an alternative classification scheme "GRAFS" (Glutamate, Rhodopsin, Adhesion, Frizzled/Taste, Secretin) was proposed for mammalian GPCR repertoire [8]. Among them, the rhodopsin family is the largest and its members recognize the most diverse array of ligands. Furthermore, approximately 100 orphan receptors exist, i.e. those for which the endogenous ligand was not found and whose function is still not known [9]. Therefore, the identification of endogenous ligands for orphan receptors (so-called “deorphanization”) allows the exploration of previously unknown physiological processes giving the opportunity to create new drugs [10].

Since 2000, when the first high-resolution crystal structure of GPCR was obtained [11], with the development of innovative protein engineering and crystallography techniques, we can observe rapid growth in the number of solved structures [7]. The emergence of experimental structures was the milestone in understanding how GPCRs function with the

greatest contribution coming from Brian Kobilka and Robert Lefkowitz, who were honored with the Nobel Prize in 2012.

All GPCRs share the same basic architecture: each receptor consists of seven transmembrane helices and a short amphipathic helix that lies parallel to the cytoplasmic surface of the membrane (Figure 1). Helices are linked by three extracellular loops (ECL1-ECL3) which modulate ligand access and three intracellular loops (ICL1-ICL3) that form a region for binding of cytosolic signaling proteins. The polypeptide chain starts with its amino terminus on the extracellular side and ends with its carboxyl terminus on the intracellular side after spanning the membrane seven times. The residues of the helical bundle form a conserved network of non-covalent contacts for the GPCR fold [12].

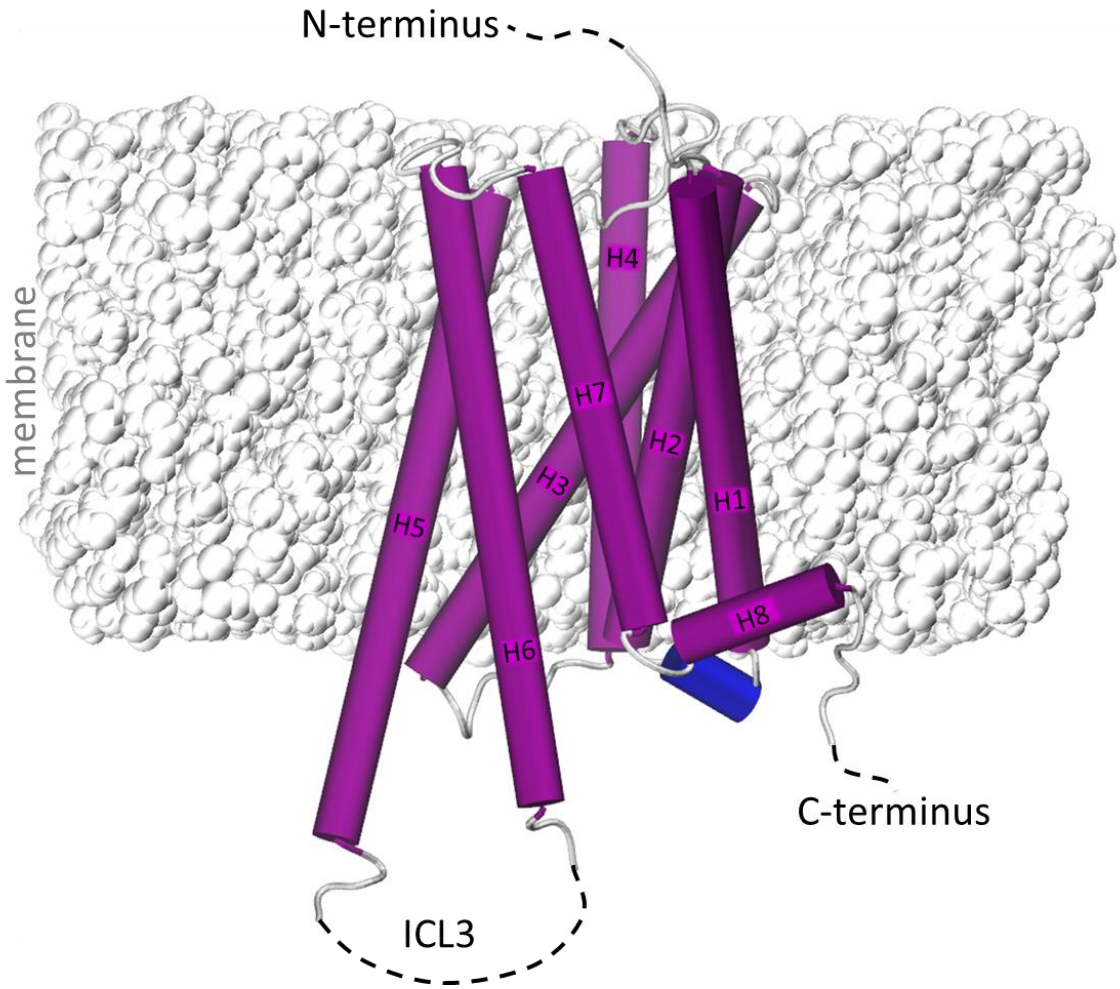

Figure 1. **General structure of G protein-coupled receptors.** The X-Ray structure of M1 receptor (PDB: 5CXV [13]) embedded in a DOPC lipid model with seven transmembrane helices (H1-H7) and the amphipathic helix H8 shown in purple. The not resolved amino terminus, carboxyl terminus, and the third intracellular loop (ICL3) are marked by dashed lines.

The simplest macroscopic model of receptors is restricted to active and inactive states, with an allosteric transition mediating the change between them [14]. However, one should remember that GPCRs are flexible proteins that are in dynamic equilibrium among multiple active- and inactive conformations which can be preferentially stabilized by ligands binding to topologically distinct sites [14, 15].

Extracellular ligand binding to a GPCR initiates a series of conformational changes in the receptor leading to coupling and activation of the cytosolic proteins thus converting a signal into a cellular response. The allosteric changes within receptors are facilitated by the existence of several energy minima and low energy barriers between the conformational states [16]. The most common feature of GPCR activation is a large outward movement of the sixth helix on the intracellular side. Together with smaller rearrangements of other helices, it creates a cavity for binding of the heterotrimeric G protein and/or β-arrestin [17].

In addition to regulating the receptor activity and thus the degree of the overall signaling response, ligands can also selectively activate certain signaling pathways to the relative exclusion of others [18]. In other words, different ligands acting at the same receptor can stabilize distinct receptor conformations linked to diverse functional outcomes. In some cases, one signaling pathway is responsible for the therapeutic effects while the other one might lead to side effects [19]. This phenomenon, known as biased agonism or functional selectivity, is exploited in pharmacology. Modern drugs incorporating ligand bias (so-called biased magic shotguns) [19] could be particularly valuable in the treatment of complex central nervous system disorders such as depression or schizophrenia [20].

There are two main biological properties with which the candidate compounds are typically described: affinity - the strength of ligand binding to receptor, and efficacy - the magnitude of cellular response. In pharmacology, affinity is defined as the extent or fraction to which a drug binds to receptors at any given concentration. It is inversely proportional to the dissociation constant of a ligand (K_D). Efficacy (also known as intrinsic activity) is the ability of a drug to elicit a physiological response when interacting with a receptor. For full agonists the efficacy is equal to 1, for partial agonists it is between 0 and 1, while for competitive antagonists the efficacy is equal to 0 [21]. The receptor–G protein association rate correlates positively with agonist efficacy [22].

The traditional method of GPCRs-based drug discovery has been to target the region occupied by the given receptor's endogenous agonist, named the orthosteric site [23]. Leading molecules acts as agonists by mimicking the response of endogenous ligand, or as antagonists, by blocking the endogenous ligand action. However, orthosteric sites exhibit a high degree of

conservation and thus orthosteric ligands are not subtype-specific. Thus, side effects are quite common. To overcome this problem in pharmacology and to design drugs that would selectively bind target receptors, researchers are focusing on allosteric sites, which are topographically distinct and more variable GPCR binding sites.

The allosteric ligands, in addition to acting independently *via* the allosteric site, can modulate the efficacy of the orthosteric ligand on the further signaling pathway. Positive allosteric modulators (PAMs) enhance the activity of orthosteric ligands while negative allosteric modulators (NAMs) inhibit them. Neutral allosteric ligands do not affect the orthosteric ligands, but block the actions of PAMs or NAMs on the same allosteric site *via* a steric interaction. Moreover, one ligand can be PAM for a given agonist, but NAM for the other [24]. Surprisingly, some ligands may be even both agonists and antagonists at different functions mediated by the same receptor [25].

Single-molecule microscopy experiments revealed that GPCRs are not randomly distributed on a plasma membrane, but are concentrated in nanodomains at least partially constituted by cytoskeleton [26]. Actin fibers, microtubules, and clathrin-coated pits form barriers to diffusion and anchor membrane proteins. In these low potential energy areas – called hot spots – GPCRs accumulate and transiently interact with G proteins. Most probably, the existence of such nanodomains enables the production of rapid, local signals which give different biological responses in topographically distinct areas [22]. Recent studies show that GPCRs are found in all membranous organelles within cells including endosomes, mitochondria, Golgi apparatus, endoplasmic reticulum, and nucleus [27]. As the action of ligands depends on the organelle their target receptors are located in, the location bias emerged as a new way for GPCRs functional selectivity [28].

Muscarinic acetylcholine receptors (mAChRs), the subfamily of rhodopsin family GPCRs, modulate a wide range of physiological functions, such as heart rate, airway constriction, eye and intestinal smooth muscle contraction, and glandular secretions [29]. Being involved in learning, memory, and cognition, they are also implicated in many neurological disorders, such as Alzheimer's disease, schizophrenia, and addictions [30].

In mammals, there are five distinct mAChR subtypes, denoted M1 to M5 (and encoded by the genes *CHRM1* to *CHRM5*) with unique distribution in central and peripheral nervous systems. M1, M3, and M5 preferentially couple to $G_{\alpha q/11}$ effector proteins to increase inositol 1,4,5-phosphate signaling and intracellular calcium. M2 and M4 couple to $G_{\alpha i/o}$ proteins leading to the inhibition of adenylyl cyclase activity and prolongation of potassium channel or nonselective cation channel opening [31]. M1 and M3 subtypes were shown to interact with

the repellent DEET [32], which acts as a behavior-modifying agent but can also directly act on both insects' peripheral and central nervous systems. The olfactory- and contact-mediated effects of DEET are distinct [33], therefore deep investigation is required for the better understanding of the mode of action of repellents.

Insects mAChRs are divided into three subfamilies (A, B, and C) among which mAChR-A is most closely related to human M1 [34, 35]. Recently, mAChR-A which is highly expressed in the insects' antennal lobe [36], was shown to have a strong behavioral impact on odor responses through olfactory receptor neurons [37]. These receptors play a key role in learning how to associate odors with unpleasant experiences [38]. Focusing on the differences in response to ligand binding to human and insect mAChRs is crucial in the development of novel, resistance-breaking repellents that would have no adverse effects in humans.

As GPCRs require conformational changes to transmit the signal into the cell, it is critical to understand the molecular basis of these changes at an atomistic level. Molecular docking followed by molecular dynamics (MD) simulations provide the opportunity to take a close look at multiple conformational states of a single receptor thus broadening the knowledge of how they respond to different classes of ligands.

4.2.2 Voltage-gated sodium channels

Ion channels are pore-forming proteins that allow a regulated flow of ions across cell membranes thus playing a principal role in regulating cellular excitability and control of homeostasis. As key proteins in the propagation of nerve signals, they modulate sensory perception, muscle activity (including the heartbeat), secretion of hormones and cytokines, transepithelial transport of salt and water, the immune response, cell proliferation, motility, and volume [39]. Ion channel malfunctions caused by inherited mutations are responsible for debilitating diseases called "channelopathies". These include cystic fibrosis, hypertension, defective insulin secretion, cardiac arrhythmias, epilepsy, ataxia, deafness, chronic pain, and kidney stones [39, 40]. Approximately 13.5% of all drugs approved by the Food and Drug Administration target ion channels, making them the second largest protein target family after GPCRs [41]. The majority of these drugs have been developed through traditional pharmacology methods without a clear understanding of their specific targets. Despite attempts to use high-throughput molecular techniques, the discovery of new drugs that target ion channels has been difficult [42].

Two fundamental properties distinguishing ion channels from simple aqueous pores are:

- high selectivity through the narrowest part of the channel (the selectivity filter) while retaining high permeability (conduction rates close to the free diffusion limit);
- pore gating - the tightly regulated mechanism of opening and closing of the pore in response to specific stimuli [43].

According to these features, ion channels are classified based on the ion type that they conduct and depending on the trigger of their opening into: ligand-gated (opening upon ligand binding), voltage-gated (opening upon change in the membrane potential), and lipid-gated (opening in response to lipid molecules such as phosphatidylinositol 4,5-bisphosphate or phosphatidic acid). From the latter category, we can distinguish mechanosensitive channels that are gated by lipid deformation in the membrane in response to mechanical force [44]. Additionally, the activity of some ion channels is sensitive to changes in temperature [45, 46].

Here, we focus on the channel types that are of critical importance in insect control, voltage-gated sodium channels (VGSCs). These proteins are wildly distributed in eukaryotes, including unicellular algae in which single-domain channels were identified, and prokaryotes. Nine subtypes of highly conserved VGSC have been identified in humans (hNav1.1-hNav1.9) with specific tissue-expression patterns. Nav1.1, Nav1.2, and Nav1.3 are mainly expressed in the central nervous system, Nav1.4 in skeletal muscles, Nav1.5 in cardiomyocytes, Nav1.6 in both central and the peripheral nervous system, while Nav1.7, Nav1.8, and Nav1.9 are highly expressed in the peripheral nervous system. In most insects, a single gene coding VGSC can be found but alternative splicing and RNA editing provide functional diversity of insects' sodium channels [47]. These multi-domain transmembrane proteins are responsible for the depolarizing phase of action potentials in nerves and muscles [48].

The structure of the α-subunit of metazoan VGSC consists of a single polypeptide chain that folds into four domains (DI-DIV) with six transmembrane helices (S1-S6) each (Figure 2). In each domain, helices S1-S4 constitute the voltage-sensing-domain (VSD) with a positively charged helix S4 acting as a voltage sensor. Helices S5 and S6, linked by membrane-reentrant pore loop (P-loop) comprising the selectivity filter DEKA motif, contribute to the ion-conducting pore domain (PD) [48]. Upon membrane depolarization, the outward movement of positively charged S4 helices generates the gating current, which triggers the activation of the channels leading to the sodium ions flow. The opening of the channel is followed by the fast inactivation process, in which the full outward movement of the S4 helix from VSDIV releases the inactivation gate (IG). The IG is a part of the cytoplasmic linker connecting DIII and DIV (DIII-DIV linker, see Figure 2), with the crucial

region centered on the Ile-Phe-Met motif in mammals and Met-Phe-Met in insects. When released, IG quickly (within 1-2 ms) occludes the inner pore of the channel, thus blocking sodium ions influx.

The β-subunits, built by an extracellular immunoglobulin-like domain and a single transmembrane helix, bind to the α-subunit to modulate the biophysical properties of VGSC such as voltage dependence of activation and inactivation. Moreover, β-subunits promote the expression and trafficking of α-subunit to the plasma membrane and modulate cell adhesion. Mutations in genes coding β-subunits are implicated in epilepsy, cardiac arrhythmia, neurodegenerative and mood disorders [49].

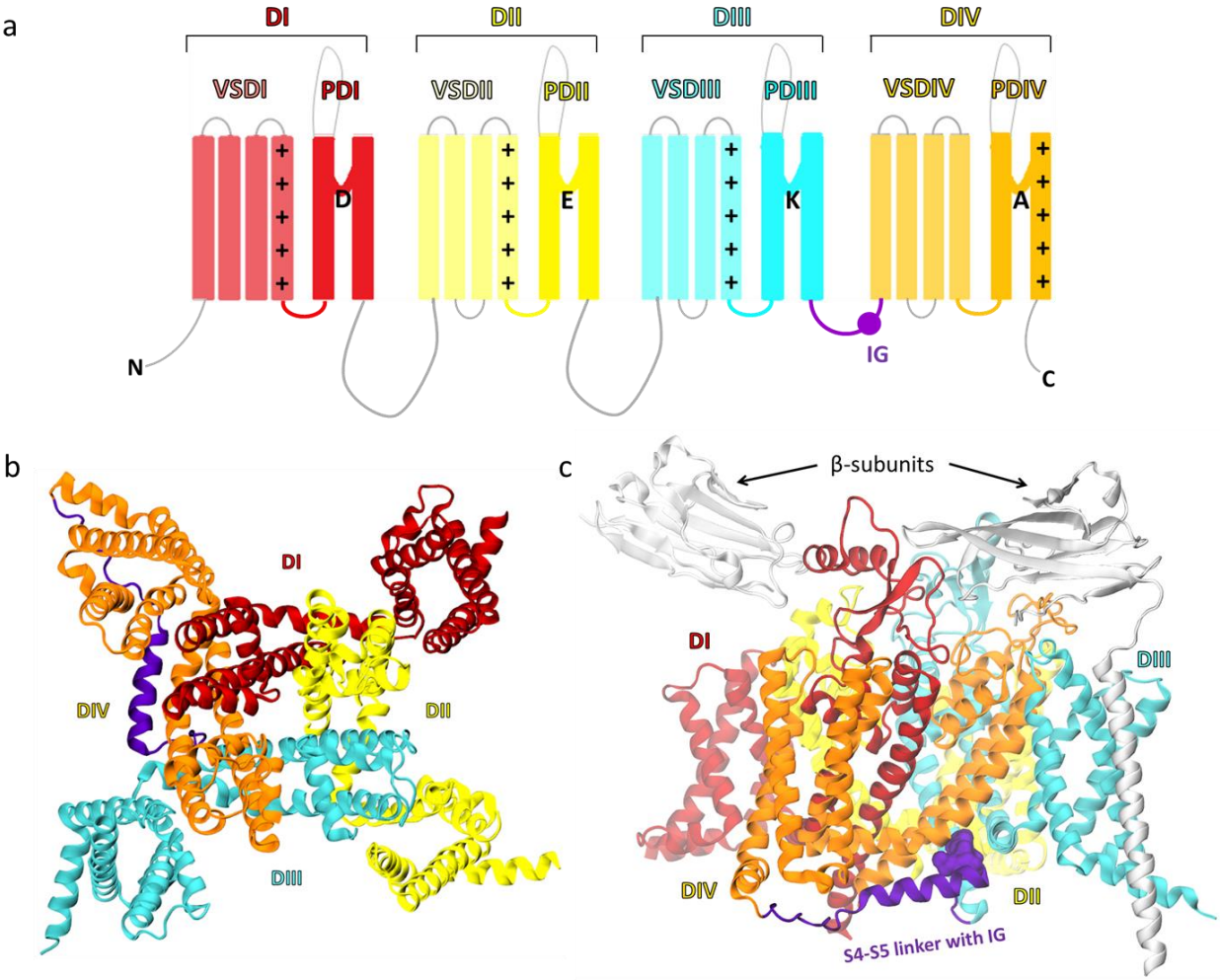

Figure 2. **Architecture of mammalian voltage-gated sodium channels.** (a) Topology of an α-subunit showing four homologous domains (DI-DIV) comprising six transmembrane helices each. The crystal structure of the inactivated-state human Nav1.7 channel (PDB: 6J8G [50]) in a top (b) and side view with β-subunits in grey (c).

Playing a critical role in the regulation of membrane excitability makes the VGSCs a significant target for a broad range of naturally occurring neurotoxins [51]. There are about 220,000 venomous species [52] that produce toxins for defense or predation. Perfected by millions of years of evolution, venom toxins became maximally efficient on a particular protein in the central nervous system. Those targeting VGSCs disrupt sodium conductance by blocking the ion-conducting pore or by altering gating [51]. Six main neurotoxin binding sites were described on the VGSCs distinguished by matters of localization but also by the results of neurotoxin action in a particular site [53]. In addition, two binding sites for synthetic compounds are discussed: the seventh for dichlorodiphenyltrichloroethane (DDT) and pyrethroid insecticides and the eighth for local anesthetics and sodium channel blocker insecticides (SCBIs) [54].

In this study, we investigate the interactions of VGSC with two groups of neurotoxins:

- peptide toxins from sea anemones – gating modifiers that are of great interest in the research of neuronal conductance modulation in both human and arthropods
- synthetic insecticides: SCBIs and non-ester pyrethroid etofenprox

4.3 Methods

Computational techniques play an important and continuously increasing role in the quest to understand and predict the biophysical phenomena arising from the structure and function of molecular systems (see Figure 3). They are particularly useful in studying biomacromolecules and their interactions with ligands thus being frequently used in drug design. The following subsection will introduce computational methods applied in this study: homology modeling, molecular docking, molecular dynamics (MD), and metadynamics simulations. For the review of the elecrophysiological measurements on Periplaneta americana nervous system see [55].

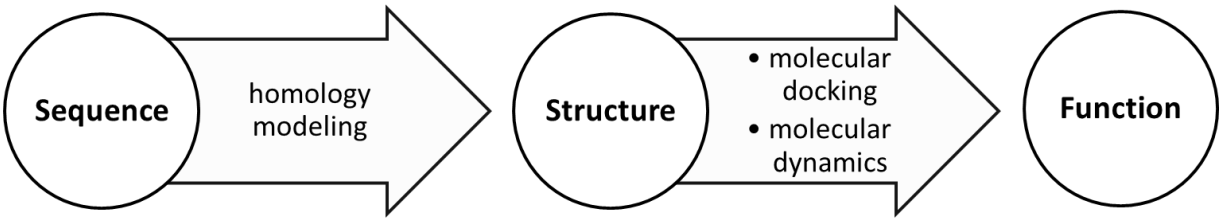

Figure 3. **The sequence-structure-function paradigm.** Computational methods applied in this study are listed to visualize the steps toward understanding the biophysical properties of investigated biomolecules.

4.3.1 Homology modeling

Homology modeling aims to predict the three-dimensional structure of a protein from its amino acid sequence based on the known structure of a related protein. This method is based on two main findings:

- The structure of a protein is uniquely determined by its amino acid sequence [56]
- In the course of evolutionary processes, the stability of protein structure tends to be relatively higher and exhibits slower rates of change compared to the associated sequence. Consequently, sequences of high homology adopt nearly identical structures, while even distantly related sequences display a propensity to fold into structurally similar conformations [57, 58].

The limit for the second rule has been found based on the analysis of more than a million sequence alignments between protein pairs of known structures [59] and is presented in Figure 4. Two protein sequences can be regarded as homologous and therefore adopt the same structure if their sequence identity falls into the region marked as a safe zone. If the identity value of two sequences falls into the twilight zone, other method should be applied, e.g. *de novo* modeling.

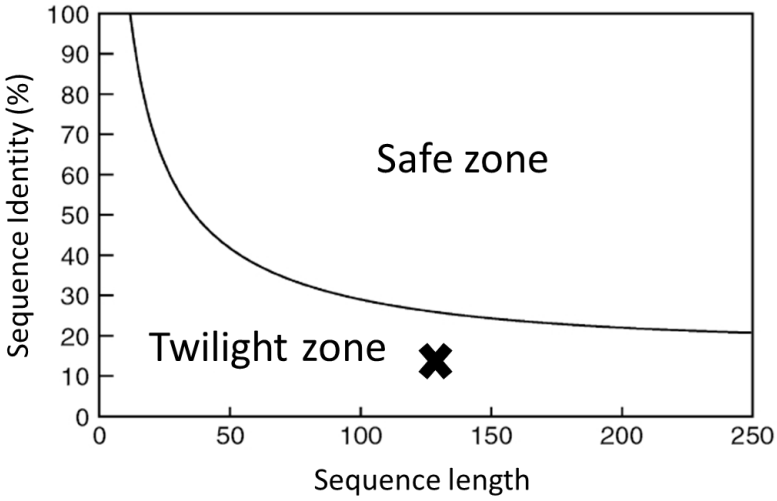

Figure 4. **The zones of protein sequence alignments.** Two protein sequences can be regarded as homologous folding into the same structure if their percentage sequence identity falls into the region marked as a safe zone. For sequence identity values falling below the zone boundary, marked as the twilight zone, homologous relationships are less certain and thus models cannot be reliably determined using homology modeling. Based on the analysis of Rost [59], figure derived from [58] with modifications.

This *in silico* method can be summarized in the following steps. First, a suitable template protein is identified based on its sequence similarity to the target protein. Next, the template structure is aligned with the target sequence and the resulting alignment is used to guide the construction of the backbone, followed by modeling of loops and side chains. Finally, the model is refined and optimized to improve its accuracy and reliability. In addition, validation of the output should be performed to find regions that might need further improvement.

This powerful tool has been the prerequisite of countless computational studies of proteins and their interactions with ligands.

4.3.2 Molecular docking

In the field of molecular modeling, docking is a computational method for predicting binding sites and poses of ligands on their macromolecular target and the associated binding affinities of the complex (Figure 5). The basic tools of the docking programs are search algorithm and energy scoring function used for generating and evaluating the ligand conformations within the receptor sites according to the intermolecular interaction energy, respectively.

The rigid docking refers to the “lock-and-key” model in which the correct orientation of a ligand, the “key”, has to be found to fit in the protein and thus open up the “lock”. In this model, the importance of geometric complementarity between the investigated molecules is emphasized, being directly proportional to the binding affinity. However, the real ligand binding conditions involve high flexibility of both ligand and its target protein. Thus, the “induced fit” model has been developed in which both molecules change their conformation to fit each other well forming a stable, low-energy complex [60]. The ability to effectively manage the inherent molecular flexibility of a target protein and accurately depict the binding affinity of a complex are the key challenges in the continuous effort in docking methodologies development [61].

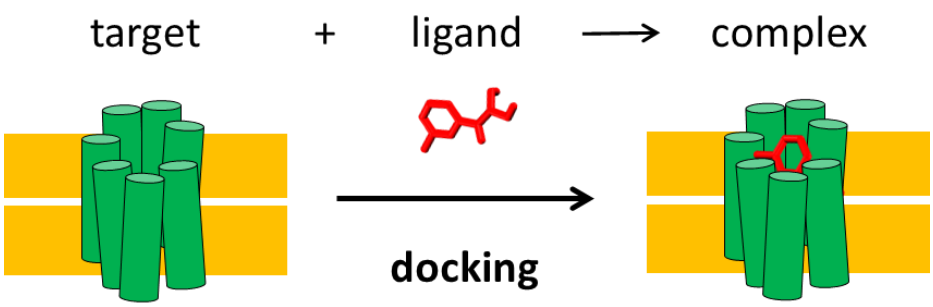

Figure 5. **The schematic view of molecular docking.** This computational method aims to find the binding mode of ligand in the target protein to form a stable complex. Here, the repellent DEET (red) binds to the orthosteric site of GPCR (green).

To evaluate the accuracy of a given docking software to predict the ligand binding modes on a target protein, the re-docking procedure is applied. Here, the crystallographic structures of ligand-bound proteins are compared to the docking results obtained by removing the ligand from the binding pocket and docking it again. When the root mean square deviation (RMSD) of the Cartesian coordinates of ligand atoms is below the 2 Å threshold, the docking is regarded as successful [62].

The key steps in molecular docking workflow are common to all protocols. Those include the preparation of both protein and ligand structures, selection of putative binding region if such data is available, running the docking program, and the evaluation of the results. The protein preparation involves the removal of water molecules, ions, or other ligands from the crystallographic structure, and filling the missing atoms. Energy minimization is then required to remove any steric clashes or other structural abnormalities. To find low-energy ligand conformations that are favorable for binding, a conformational search or energy minimization can be performed. One should also ensure that the protonation, tautomeric, and stereoisomeric forms of the ligand are correct. If there is no information regarding the location of ligand binding site, the search space should incorporate the whole protein surface to run a so-called “blind docking”. If the mutagenesis data on active site residues are available, the search space can be reduced to limit the computational time and increase the probability of reliable results. Upon completion of these steps, the docking software is run to generate possible protein-ligand complexes by systematically varying the position of the ligand within the target protein. The generated complexes are then scored and ranked based on their binding affinities. Each docking software has its own scoring function that incorporates various molecular descriptors, such as van der Waals interactions, electrostatic interactions, hydrogen bonding, desolvation effects, and the number of rotatable

bonds in the ligand. These are used to predict the binding energy of each complex. The greatest challenge for a user is to evaluate the docking results. It is highly advisable to take any available information into account to eliminate false positive poses.

Docking programs can be classified by their search algorithms into three categories: shape matching, systematic search (e.g. exhaustive search, fragmentation, and conformational ensemble), and stochastic search algorithms (Monte Carlo simulations, genetic algorithms, Tabu search, and swarm optimization methods) [63, 64]. Sampling refers to the allowed degree of binding site flexibility which can be alternatively represented by using multiple conformers or ensembles of rigid protein structures.

Presuming adequate search strategies, docking accuracy relies on the scoring function. Four classes of scoring functions are distinguished:

- force-field based scoring functions aim to quantify the actual molecular forces between a protein and a ligand by calculating the sum of the non-bonded (electrostatics and van der Waals) interactions using a set of derived force-field parameters such as AMBER or CHARMM;
- knowledge-based scoring functions are based on the statistical analysis of the interatomic contact frequencies and/or distances between the ligand and protein deposited in databases of experimental structures;
- empirical scoring functions estimate the binding affinity of a complex on the basis of a set of weighted energy terms, such as hydrogen bond, ionic interaction, hydrophobic effect, and desolvation. Coefficients are obtained from regression analysis fitted to a test set of crystal complexes with known binding affinities.
- consensus scoring functions combine several different scores to assess the docking conformation [65].

One of the most popular and highly cited academic docking program is AutoDock Vina [66]. Its empirical scoring function is based on pairwise interactions between atoms and includes Gaussian steric interaction terms, a finite repulsion term, piecewise linear hydrophobic and hydrogen-bond interaction terms, and an entropic term proportional to the number of rotatable bonds. The code uses an elaborated optimization method (Iterated Local Search global optimizer [67] which includes Broyden-Fletcher-Goldfarb-Shanno method [68]).Final scoring function is linearly reweighted to fit the score to free energies (kcal/mol). In the comparative assessment of scoring functions 2013, AutoDock Vina was found in the

first quarter among all methods tested and the best of all methods in terms of docking power with 93% of native poses in the three best-ranked ones [69].

In this study, we use smina, a fork for AutoDock Vina [66] that provides enhanced support for minimization and scoring [70]. The empirical scoring function of smina is designed based on a set of potential terms of AutoDock Vina and a high-quality data set of structures and affinities. In the Community Structure−Activity Resource 2011 exercise, smina outperformed AutoDock Vina in sampling low RMSD poses when cross-docking [70].

The complexes found using docking often serve as the starting points for MD or metadynamics simulations.

4.3.3 Molecular dynamics simulations

Molecular Dynamics (MD) simulations can serve as a computational microscope capturing the behavior of biomolecules at spatial and temporal resolution difficult to access experimentally, i.e. in the order of the hydrogen atom and femtosecond [71]. This state-of-the-art method, based on the numerical integration of Newton's equations of motion, aims to observe the natural time evolution (physical movement of atoms) of a system. It is commonly used to study the biophysical phenomenon in controlled conditions, as it enables modeling of dynamic processes thus helping to understand the properties of molecule assemblies and the interactions between remote parts of proteins. MD simulations are of particular importance for membrane proteins, as experimental characterization of their structural dynamics is challenging [72].

Recently, X-Ray crystallography and cryo-electron microscopy (cryo-EM) techniques have led to a bloom of published structures of membrane proteins. While being extremely valuable, they provide only a static, frozen view of a complex system which is not sufficient for understanding a full picture of their biological activity. Nowadays, practically all experimental structures of biomolecules are MD refined, which is particularly important for membrane proteins that suffer from the absence of lipid bilayer. Moreover, the development of highly parallelized and optimized hardware and software tools and thus the growing computing power allow studying molecular systems of hundreds of thousands of atoms on continuously increasing time scales (reaching milliseconds when dedicated supercomputers like Anton are used) [73]. Dynamic motions on larger timescales connect structure and function complementing the sequence-structure-function paradigm (see Figure 3).

The MD time step (10^{-15} s) involves a computationally demanding calculation of the forces acting on each atom in a system, followed by a less computationally expensive integration step that updates the positions of the atoms based on classical laws of motion [73]. Forces acting on a given atom are calculated using a force field mathematical model based on the positions of the other atoms and the network of covalent bonds connecting them. In commonly used biomolecular force fields, the total force acting on an atom is composed of two components:

- bonded forces that arise from interactions between small groups of atoms connected by one or more covalent bonds. These typically consist of bond stretching terms, angle bending terms, and terms describing the rotation of torsional angles;
- non-bonded component comprise point-charge Coulomb electrostatic interactions and van der Waals forces modeled by the Lennard-Jones potential which describes short range repulsion ($1/r^{12}$) and weak long-range attraction ($1/r^{6}$)

Among the most popular force fields are CHARMM [74], AMBER [75], GROMOS [76], and OPLS [77], the first three of which are often employed in biomolecular simulations, while the latter was originally developed to simulate condensed matter. These can be applied in the most popular MD software packages that support multiple force fields, such as NAMD [78], GROMACS [79], AMBER [80], CHARMM [81], or OpenMM [82].

In this study, we applied the CHARMM force field that presents the following general expression for the energy [83]:

$$E = E_{bonded} + E_{nonbonded}$$

$$E_{bonded} = \sum_{bonds} K_b (b - b_0)^2 + \sum_{angles} K_\theta (\theta - \theta_0)^2 + \sum_{\substack{improper \\ dihedrals}} K_\varphi (\varphi - \varphi_0)^2 + \sum_{dihedrals} \sum_{n=1}^{6} K_{\phi,n} (1 + \cos(n\phi - \delta_n)) \quad (1)$$

$$E_{nonbonded} = \sum_{\substack{nonbonded \\ pairs i,j}} \frac{q_i q_j}{4\pi D \|\mathbf{r}_i - \mathbf{r}_j\|} + \sum_{\substack{nonbonded \\ pairs i,j}} \varepsilon_{ij} \left[\left(\frac{R_{\min,ij}}{\|\mathbf{r}_i - \mathbf{r}_j\|} \right)^{12} - 2 \left(\frac{R_{\min,ij}}{\|\mathbf{r}_i - \mathbf{r}_j\|} \right)^{6} \right],$$

where: indeces i, j - denote atoms; r_i, r_j – denote positions of atoms; b are bond lengths; θ – bond angles; φ – improper angles; Ø - torsional angles; q_i, q_j – denote partial atomic charges; and other symbols are parameters depending on the amino acid and force field version used.

MD simulations are a valuable tool for several reasons. Primarily, they enable the precise determination of the position and motion of each atom at any given time, which is a challenging task with experimental techniques. Additionally, the simulation conditions can be accurately controlled, including the initial conformation of a protein, its post-translational modifications, mutations, and the presence of other molecules in its environment, as well as the protonation state, temperature, and voltage across a membrane. By comparing simulations performed under different conditions, the effects of various molecular perturbations can be identified [84].

Despite their many advantages, MD simulations also have the following important limitations that must be considered:

- Timescale: MD simulations are limited by the computing power to relatively short timescales that may not be enough to capture biophysical phenomena that take longer to occur
- Accuracy of force fields: force fields are inherently approximate and not reactive – covalent bond formation and breaking are not possible during simulations; polarization effects are not included – the redistribution of electrons around each atom in response to changes in the environment cannot be captured

These problems can be overcome by applying enhanced sampling techniques (see the 4.3.2 subsection) or quantum mechanics/molecular mechanics simulations. Force fields are continuously improved leading to improved accuracy and the development of sophisticated polarization algorithms.

Nevertheless, the greatest challenge is in analyzing the results. Precise specification of the most informative quantities and events a priori is not a trivial task. To derive highly valuable insights from simulations, it is crucial to analyze and interpret them while considering all experimental data for the molecular system being investigated. Such analyses typically involve both quantitative analysis and a meticulous visual inspection using molecular rendering software [84].

The emergence of high-quality crystal structures (with a resolution below 3.5 Å), together with increasing computing power, open the way to study such biophysical processes as ligand binding, membrane transport, and protein folding [71]. In this study, we apply MD to investigate the allosteric changes in mAChRs in response to repellent binding and the interactions of SCBIs with VGSC.

4.3.4 Metadynamics simulations

The use of equilibrium MD simulations as a computational microscope is limited by sampling difficulties when an energy barrier separating potential energy minima is high and thus the physical process occurs rarely [85]. The probability that the system will cross such barrier driven by a thermal fluctuation only is small as the system is likely to get stuck in a metastable state. According to the transition state theory, the time to cross a free energy barrier increase exponentially with its height. The timescales of MD runs usually do not allow the system to visit all the energetically relevant configurations which is known as the ergodicity problem [86]. Therefore, enhanced sampling methods should be applied to accelerate conformational transitions between metastable states [87].

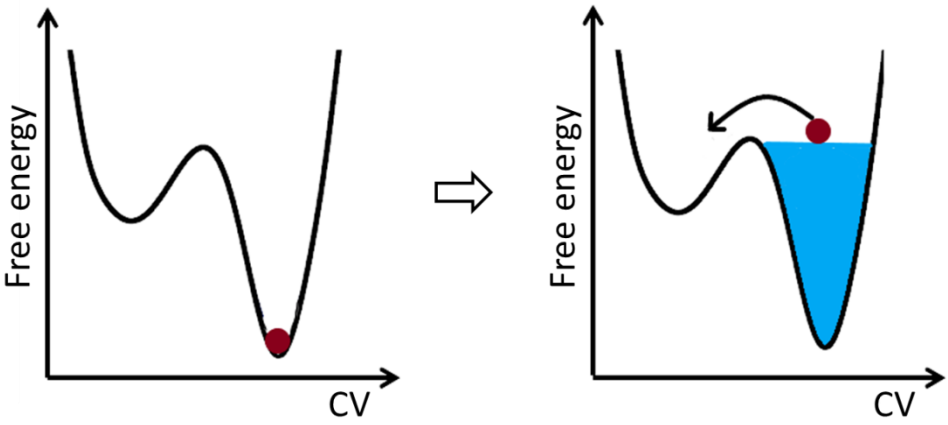

Figure 6. **A schematic view of metadynamics concept**. A collection of Gaussian potentials (blue) is deposited to fill up a metastable state and the system (red dot) moves into the second metastable basin, overcoming in that way a large free energy barrier. Geometries of molecular systems are analyzed in terms of collective variables (CV).

Metadynamics is a technique used to enhance sampling of rare events and reconstruct a free-energy landscape of complex systems during atomistic simulations. Metadynamics allows the exploration of new reaction pathways by enabling the system to cross the free energy barriers by pushing it away from local free energy minima [86]. It is achieved by filling in the potential energy minima thus making the system escape from the metastable state. To do so, a set of low-dimensional descriptors − collective variables (CVs), i.e. functions of reaction Cartesian coordinates, has to be defined to describe the relevant degrees of freedom of the system. As the simulation progresses, the system is biased by a history-dependent potential that varies in response to the evolution of these collective variables. The small gaussian-shaped repulsive potentials are added at locations on the free energy landscape

that have already been explored, thereby discouraging the system from revisiting sampled configurations [85]. Filling in the energy wells allows the system to explore new regions. After a transient, the bias potential provides an unbiased estimate of the underlying free energy [86].

The usefulness of metadynamics largely depends on the appropriate choice of CVs that describe the relevant transitions. CVs have to distinguish between the initial and final state and describe all the relevant intermediates. They should include all the slow modes of the system while being limited in number [86]. Among the most frequently used CVs are interatomic distances, angles, dihedrals, coordination numbers, radius of gyration, dipole moment, or number of hydrogen bonds. CVs can be found by trial and error or selected automatically using approaches inspired by machine learning [87].

Metadynamics has been successfully applied to various biological problems, including protein folding, ligand binding, and conformational transitions in biomolecules. In this study, we use enhanced sampling techniques to find the entry route of insecticide to the ion-conducting pore of VGSC.

5. The aims of the study

The aims of the doctoral thesis were to:

- characterize the conformational changes in human M1 muscarinic receptor and in insect mAChR-A upon agonists and antagonists binding
- create a map of predicted subtle local changes in mAChRs related to agonists and antagonist action by the detailed analysis of the residue-residue contact score (RRCS) dynamic evolution
- propose a novel type of bitopic, photoswitchable compound with a potential repellent activity that would cause the desired effects in terms of RRCS in insect mAChR-A
- investigate the interactions between VSD of the cockroach VGSC with four peptide toxins from the sea anemones and compare their efficacy
- find the entrance pathway for N-decarbomethoxyllated JW062 (DCJW) insecticide to the central cavity of the ion-conducting pore of mosquito VGSC
- evaluate the impact of target site insensitivity conferring resistance to pyrethroids on SCBIs action on mosquito VGSC

The outcomes of the investigation framed above are presented in three original articles [88-90].

6. References

1. Gubler, D.J., *Resurgent vector-borne diseases as a global health problem.* Emerging infectious diseases, 1998. **4**(3): p. 442.
2. Riveron, J.M., et al., *Insecticide resistance in malaria vectors: an update at a global scale*, in *Towards malaria elimination-a leap forward*. 2018, IntechOpen.
3. Deutsch, C.A., et al., *Increase in crop losses to insect pests in a warming climate.* Science, 2018. **361**(6405): p. 916-919.
4. Bradshaw, C.J., et al., *Massive yet grossly underestimated global costs of invasive insects.* Nature communications, 2016. **7**(1): p. 12986.
5. Wise, A., K. Gearing, and S. Rees, *Target validation of G-protein coupled receptors.* Drug discovery today, 2002. **7**(4): p. 235-246.
6. Wacker, D., R.C. Stevens, and B.L. Roth, *How ligands illuminate GPCR molecular pharmacology.* Cell, 2017. **170**(3): p. 414-427.
7. Congreve, M., et al., *Impact of GPCR structures on drug discovery.* Cell, 2020. **181**(1): p. 81-91.
8. Fredriksson, R., et al., *The G-Protein-Coupled Receptors in the Human Genome Form Five Main Families. Phylogenetic Analysis, Paralogon Groups, and Fingerprints.* Molecular pharmacology, 2003. **63**(6).
9. Laschet, C., N. Dupuis, and J. Hanson, *The G protein-coupled receptors deorphanization landscape.* Biochemical pharmacology, 2018. **153**: p. 62-74.
10. Allen, J.A. and B.L. Roth, *Strategies to discover unexpected targets for drugs active at G protein-coupled receptors.* Annu Rev Pharmacol Toxicol, 2011. **51**: p. 117-44.
11. Palczewski, K., et al., *Crystal structure of rhodopsin: AG protein-coupled receptor.* Science, 2000. **289**(5480): p. 739-745.
12. Venkatakrishnan, A.J., et al., *Molecular signatures of G-protein-coupled receptors.* Nature, 2013. **494**(7436): p. 185-94.
13. Thal, D.M., et al., *Crystal structures of the M1 and M4 muscarinic acetylcholine receptors.* Nature, 2016. **531**(7594): p. 335-340.
14. Thal, D.M., et al., *Structural insights into G-protein-coupled receptor allostery.* Nature, 2018. **559**(7712): p. 45-53.
15. Frei, J.N., et al., *Conformational plasticity of ligand-bound and ternary GPCR complexes studied by 19F NMR of the β1-adrenergic receptor.* Nature communications, 2020. **11**(1): p. 669.
16. Manglik, A. and B. Kobilka, *The role of protein dynamics in GPCR function: insights from the β2AR and rhodopsin.* Current opinion in cell biology, 2014. **27**: p. 136-143.
17. Hilger, D., M. Masureel, and B.K. Kobilka, *Structure and dynamics of GPCR signaling complexes.* Nat Struct Mol Biol, 2018. **25**(1): p. 4-12.
18. Shonberg, J., et al., *Biased agonism at G protein-coupled receptors: the promise and the challenges--a medicinal chemistry perspective.* Med Res Rev, 2014. **34**(6): p. 1286-330.
19. McCorvy, J.D., et al., *Structure-inspired design of beta-arrestin-biased ligands for aminergic GPCRs.* Nat Chem Biol, 2018. **14**(2): p. 126-134.
20. Park, S.M., et al., *Effects of β-arrestin-biased dopamine D2 receptor ligands on schizophrenia-like behavior in hypoglutamatergic mice.* Neuropsychopharmacology, 2016. **41**(3): p. 704.
21. Salahudeen, M.S. and P.S. Nishtala, *An overview of pharmacodynamic modelling, ligand-binding approach and its application in clinical practice.* Saudi Pharmaceutical Journal, 2017. **25**(2): p. 165-175.
22. Calebiro, D. and M.L. Jobin, *Hot spots for GPCR signaling: lessons from single-molecule microscopy.* Curr Opin Cell Biol, 2019. **57**: p. 57-63.

23. Christopoulos, A., *Allosteric binding sites on cell-surface receptors: novel targets for drug discovery.* Nat Rev Drug Discov, 2002. **1**(3): p. 198-210.
24. Christopoulos, A., *Advances in G protein-coupled receptor allostery: from function to structure.* Mol Pharmacol, 2014. **86**(5): p. 463-78.
25. Urban, J.D., et al., *Functional selectivity and classical concepts of quantitative pharmacology.* J Pharmacol Exp Ther, 2007. **320**(1): p. 1-13.
26. Sungkaworn, T., et al., *Single-molecule imaging reveals receptor-G protein interactions at cell surface hot spots.* Nature, 2017. **550**(7677): p. 543-547.
27. Nezhady, M.A.M., J.C. Rivera, and S. Chemtob, *Location bias as emerging paradigm in GPCR biology and drug discovery.* Iscience, 2020. **23**(10): p. 101643.
28. Irannejad, R., et al., *Functional selectivity of GPCR-directed drug action through location bias.* Nature chemical biology, 2017. **13**(7): p. 799.
29. Nathanson, N.M., *Molecular properties of the muscarinic acetylcholine receptor.* Annual review of neuroscience, 1987. **10**(1): p. 195-236.
30. Kruse, A.C., et al., *Muscarinic acetylcholine receptors: novel opportunities for drug development.* Nat Rev Drug Discov, 2014. **13**(7): p. 549-60.
31. Eglen, R.M., *Muscarinic receptor subtype pharmacology and physiology.* Progress in medicinal chemistry, 2005. **43**: p. 105-136.
32. Abd-Ella, A., et al., *The Repellent DEET Potentiates Carbamate Effects via Insect Muscarinic Receptor Interactions: An Alternative Strategy to Control Insect Vector-Borne Diseases.* PLoS One, 2015. **10**(5): p. e0126406.
33. DeGennaro, M., et al., *orco mutant mosquitoes lose strong preference for humans and are not repelled by volatile DEET.* Nature, 2013. **498**(7455): p. 487-91.
34. Collin, C., et al., *Two types of muscarinic acetylcholine receptors in Drosophila and other arthropods.* Cellular and molecular life sciences, 2013. **70**(17): p. 3231-3242.
35. Xia, R.Y., et al., *A new family of insect muscarinic acetylcholine receptors.* Insect Mol Biol, 2016. **25**(4): p. 362-9.
36. Blake, A., et al., *Drosophila nervous system muscarinic acetylcholine receptor: transient functional expression and localization by immunocytochemistry.* Molecular pharmacology, 1993. **44**(4): p. 716-724.
37. Rozenfeld, E., H. Lerner, and M. Parnas, *Muscarinic Modulation of Antennal Lobe GABAergic Local Neurons Shapes Odor Coding and Behavior.* Cell Rep, 2019. **29**(10): p. 3253-3265 e4.
38. Bielopolski, N., et al., *Inhibitory muscarinic acetylcholine receptors enhance aversive olfactory learning in adult Drosophila.* Elife, 2019. **8**.
39. Hübner, C.A. and T.J. Jentsch, *Ion channel diseases.* Human molecular genetics, 2002. **11**(20): p. 2435-2445.
40. Jentsch, T.J., C.A. Hübner, and J.C. Fuhrmann, *Ion channels: function unravelled by dysfunction.* Nature cell biology, 2004. **6**(11): p. 1039-1047.
41. Overington, J.P., B. Al-Lazikani, and A.L. Hopkins, *How many drug targets are there?* Nature reviews Drug discovery, 2006. **5**(12): p. 993-996.
42. Clare, J.J., *Targeting ion channels for drug discovery.* Discovery medicine, 2010. **9**(46): p. 253-260.
43. Alberts, B., et al., *Ion channels and the electrical properties of membranes*, in *Molecular Biology of the Cell. 4th edition*. 2002, Garland Science.
44. Sukharev, S. and F. Sachs, *Molecular force transduction by ion channels–diversity and unifying principles.* Journal of cell science, 2012. **125**(13): p. 3075-3083.
45. Yao, J., B. Liu, and F. Qin, *Modular thermal sensors in temperature-gated transient receptor potential (TRP) channels.* Proceedings of the National Academy of Sciences, 2011. **108**(27): p. 11109-11114.
46. Chowdhury, S., B.W. Jarecki, and B. Chanda, *A molecular framework for temperature-dependent gating of ion channels.* Cell, 2014. **158**(5): p. 1148-1158.

47. Dong, K., et al., *Molecular biology of insect sodium channels and pyrethroid resistance.* Insect biochemistry and molecular biology, 2014. **50**: p. 1-17.
48. Jiang, D., J. Zhang, and Z. Xia, *Structural Advances in Voltage-Gated Sodium Channels.* Frontiers in Pharmacology, 2022. **13**.
49. O'Malley, H.A. and L.L. Isom, *Sodium channel β subunits: emerging targets in channelopathies.* Annual review of physiology, 2015. **77**: p. 481-504.
50. Shen, H., et al., *Structures of human Nav1.7 channel in complex with auxiliary subunits and animal toxins.* Science, 2019. **363**(6433): p. 1303-1308.
51. Catterall, W.A., et al., *Voltage-gated ion channels and gating modifier toxins.* Toxicon, 2007. **49**(2): p. 124-141.
52. Holford, M., et al., *Venoms to the rescue.* Science, 2018. **361**(6405): p. 842-844.
53. Stevens, M., S. Peigneur, and J. Tytgat, *Neurotoxins and their binding areas on voltage-gated sodium channels.* Frontiers in pharmacology, 2011. **2**: p. 71.
54. Silver, K.S., et al., *Voltage-gated sodium channels as insecticide targets.* Advances in insect physiology, 2014. **46**: p. 389-433.
55. Stankiewicz, M., M. Dąbrowski, and M.E. De Lima, *Nervous system of Periplaneta americana cockroach as a model in toxinological studies: a short historical and actual view.* Journal of Toxicology, 2012. **2012**.
56. Epstein, C.J., R.F. Goldberger, and C.B. Anfinsen. *The genetic control of tertiary protein structure: studies with model systems*. in *Cold Spring Harbor symposia on quantitative biology*. 1963. Cold Spring Harbor Laboratory Press.
57. Sander, C. and R. Schneider, *Database of homology-derived protein structures and the structural meaning of sequence alignment.* Proteins: Structure, Function, and Bioinformatics, 1991. **9**(1): p. 56-68.
58. Krieger, E., S.B. Nabuurs, and G. Vriend, *Homology modeling.* Structural bioinformatics, 2003. **44**: p. 509-523.
59. Rost, B., *Twilight zone of protein sequence alignments.* Protein engineering, 1999. **12**(2): p. 85-94.
60. Fan, J., A. Fu, and L. Zhang, *Progress in molecular docking.* Quantitative Biology, 2019. **7**: p. 83-89.
61. Guedes, I.A., C.S. de Magalhães, and L.E. Dardenne, *Receptor–ligand molecular docking.* Biophysical reviews, 2014. **6**: p. 75-87.
62. Morris, G.M. and M. Lim-Wilby, *Molecular docking.* Molecular modeling of proteins, 2008: p. 365-382.
63. Wang, Z., et al., *Comprehensive evaluation of ten docking programs on a diverse set of protein–ligand complexes: the prediction accuracy of sampling power and scoring power.* Physical Chemistry Chemical Physics, 2016. **18**(18): p. 12964-12975.
64. Dias, R., J. de Azevedo, and F. Walter, *Molecular docking algorithms.* Current drug targets, 2008. **9**(12): p. 1040-1047.
65. Meng, X.-Y., et al., *Molecular docking: a powerful approach for structure-based drug discovery.* Current computer-aided drug design, 2011. **7**(2): p. 146-157.
66. Trott, O. and A.J. Olson, *AutoDock Vina: improving the speed and accuracy of docking with a new scoring function, efficient optimization, and multithreading.* Journal of computational chemistry, 2010. **31**(2): p. 455-461.
67. Baxter, J., *Local optima avoidance in depot location.* Journal of the Operational Research Society, 1981. **32**(9): p. 815-819.
68. Nocedal, J. and S.J. Wright, *Numerical optimization*. 1999: Springer.
69. Gaillard, T., *Evaluation of AutoDock and AutoDock Vina on the CASF-2013 benchmark.* Journal of chemical information and modeling, 2018. **58**(8): p. 1697-1706.
70. Koes, D.R., M.P. Baumgartner, and C.J. Camacho, *Lessons learned in empirical scoring with smina from the CSAR 2011 benchmarking exercise.* Journal of chemical information and modeling, 2013. **53**(8): p. 1893-1904.

71. Dror, R.O., et al., *Biomolecular simulation: a computational microscope for molecular biology.* Annual review of biophysics, 2012. **41**: p. 429-452.
72. Dror, R.O., et al., *Exploring atomic resolution physiology on a femtosecond to millisecond timescale using molecular dynamics simulations.* Journal of General Physiology, 2010. **135**(6): p. 555-562.
73. Shaw, D.E., et al. *Millisecond-scale molecular dynamics simulations on Anton*. in *Proceedings of the conference on high performance computing networking, storage and analysis*. 2009.
74. MacKerell Jr, A.D., et al., *All-atom empirical potential for molecular modeling and dynamics studies of proteins.* The journal of physical chemistry B, 1998. **102**(18): p. 3586-3616.
75. Cornell, W.D., et al., *A second generation force field for the simulation of proteins, nucleic acids, and organic molecules.* Journal of the American Chemical Society, 1995. **117**(19): p. 5179-5197.
76. Oostenbrink, C., et al., *A biomolecular force field based on the free enthalpy of hydration and solvation: the GROMOS force-field parameter sets 53A5 and 53A6.* Journal of computational chemistry, 2004. **25**(13): p. 1656-1676.
77. Jorgensen, W.L., D.S. Maxwell, and J. Tirado-Rives, *Development and testing of the OPLS all-atom force field on conformational energetics and properties of organic liquids.* Journal of the American Chemical Society, 1996. **118**(45): p. 11225-11236.
78. Phillips, J.C., et al., *Scalable molecular dynamics with NAMD.* Journal of computational chemistry, 2005. **26**(16): p. 1781-1802.
79. Berendsen, H.J., D. van der Spoel, and R. van Drunen, *GROMACS: A message-passing parallel molecular dynamics implementation.* Computer physics communications, 1995. **91**(1-3): p. 43-56.
80. Pearlman, D.A., et al., *AMBER, a package of computer programs for applying molecular mechanics, normal mode analysis, molecular dynamics and free energy calculations to simulate the structural and energetic properties of molecules.* Computer Physics Communications, 1995. **91**(1-3): p. 1-41.
81. Brooks, B.R., et al., *CHARMM: the biomolecular simulation program.* Journal of computational chemistry, 2009. **30**(10): p. 1545-1614.
82. Eastman, P., et al., *OpenMM 7: Rapid development of high performance algorithms for molecular dynamics.* PLoS computational biology, 2017. **13**(7): p. e1005659.
83. Vanommeslaeghe, K. and A. MacKerell Jr, *CHARMM additive and polarizable force fields for biophysics and computer-aided drug design.* Biochimica et Biophysica Acta (BBA)-General Subjects, 2015. **1850**(5): p. 861-871.
84. Hollingsworth, S.A. and R.O. Dror, *Molecular dynamics simulation for all.* Neuron, 2018. **99**(6): p. 1129-1143.
85. Laio, A. and M. Parrinello, *Escaping free-energy minima.* Proceedings of the national academy of sciences, 2002. **99**(20): p. 12562-12566.
86. Barducci, A., M. Bonomi, and M. Parrinello, *Metadynamics.* Wiley Interdisciplinary Reviews: Computational Molecular Science, 2011. **1**(5): p. 826-843.
87. Bussi, G. and A. Laio, *Using metadynamics to explore complex free-energy landscapes.* Nature Reviews Physics, 2020. **2**(4): p. 200-212.
88. Niklas, B., et al., *Interactions of Sea Anemone Toxins with Insect Sodium Channel—Insights from Electrophysiology and Molecular Docking Studies.* Molecules, 2021. **26**(5): p. 1302.
89. Niklas, B., B. Lapied, and W. Nowak, *In search of synergistic insect repellents: Modeling of muscarinic GPCR interactions with classical and bitopic photoactive ligands.* Molecules, 2022. **27**(10): p. 3280.
90. Niklas, B., et al., *Toward overcoming pyrethroid resistance in mosquito control: the role of sodium channel blocker insecticides.* bioRxiv, 2023: p. 2023.03.29.534712.

7. List of articles included in the doctoral thesis

Accepted:

1. **Niklas B.**, Lapied B., Nowak W.,
In Search of Synergistic Insect Repellents: Modeling of Muscarinic GPCR Interactions with Classical and Bitopic Photoactive Ligands,
Molecules 2022, 27 (10), 3280-3303; IF=4.927
https://doi.org/10.3390/molecules26051302

cotribution: conceptualization; software; validation; investigation; data curation; visualization; writing - original draft preparation; writing - review and editing

2. **Niklas B.**, Jankowska M., Gordon D., Béress L., Stankiewicz M., Nowak W.,
Interactions of Sea Anemone Toxins with Insect Sodium Channel—Insights from Electrophysiology and Molecular Docking Studies,
Molecules 2021, 26 (5), 1302-1324; IF=4.927
https://doi.org/10.3390/molecules27103280

cotribution: computational part (methodology, software, validation, investigation, visualization, writing - original draft preparation); writing - review and editing

In review:

1. **Niklas B.**, Rydzewski J., Lapied B., Nowak W.,
Toward overcoming pyrethroid resistance in mosquito control: the role of sodium channel blocker insecticides,
Submitted to the International Journal of Biological Macromolecules; IF=8.025;
Deposited in the bioRxiv; doi: https://doi.org/10.1101/2023.03.29.534712

cotribution: conceptualization; formal analysis; methodology; resources; software; investigation; data curation; validation; visualization; writing - original draft preparation

8. Article I

In Search of Synergistic Insect Repellents: Modeling of Muscarinic GPCR Interactions with Classical and Bitopic Photoactive Ligands

molecules

MDPI

Article

In Search of Synergistic Insect Repellents: Modeling of Muscarinic GPCR Interactions with Classical and Bitopic Photoactive Ligands

Beata Niklas [1,2], Bruno Lapied [3] and Wieslaw Nowak [1,*]

[1] Institute of Physics, Faculty of Physics, Astronomy and Informatics, Nicolaus Copernicus University in Torun, 87-100 Torun, Poland; beata.niklas@doktorant.umk.pl
[2] Faculty of Biological and Veterinary Sciences, Nicolaus Copernicus University, Lwowska 1, 87-100 Torun, Poland
[3] University Angers, INRAE, SIFCIR, SFR QUASAV, F-49045 Angers, France; bruno.lapied@univ-angers.fr
* Correspondence: wiesiek@umk.pl

Abstract: Insect vector-borne diseases pose serious health problems, so there is a high demand for efficient molecules that could reduce transmission. Using molecular docking and molecular dynamics (MD) simulation, we studied a series of compounds acting on human and insect muscarinic acetylcholine receptors (mAChRs), a novel target of synergistic agents in pest control. We characterized early conformational changes of human M1 and fruit fly type-A mAChR G protein-coupled receptors (GPCRs) in response to DEET, IR3535, and muscarine binding based on the MD analysis of the activation microswitches known to form the signal transduction pathway in class A GPCRs. We indicated groups of microswitches that are the most affected by the presence of a ligand. Moreover, to increase selectivity towards insects, we proposed a new, bitopic, photoswitchable mAChR ligand—BQCA-azo-IR353 and studied its interactions with both receptors. Modeling data showed that using a bitopic ligand may be a promising strategy in the search for better insect control.

Keywords: GPCR modulators; docking; bitopic ligands; molecular dynamics; IR3535; DEET; muscarinic receptors; synergy

check for updates

Citation: Niklas, B.; Lapied, B.; Nowak, W. In Search of Synergistic Insect Repellents: Modeling of Muscarinic GPCR Interactions with Classical and Bitopic Photoactive Ligands. *Molecules* **2022**, *27*, 3280. https://doi.org/10.3390/molecules27103280

Academic Editors: Livia Basile and Salvatore Guccione

Received: 17 April 2022
Accepted: 18 May 2022
Published: 20 May 2022

1. Introduction

Mosquitos are the primary vectors of diseases such as malaria, yellow fever, dengue, chikungunya, West Nile, and Zika, which affect about 700 million and kill a million people each year. The World Health Organization (WHO) notes that more than half of the human population is currently at risk of mosquito-borne diseases. Moreover, there are concerns that progressive climate change may affect the extent of vector-borne disease outbreaks and insecticide sensitivity [1,2]. In 2019, malaria alone caused 229 million clinical episodes, which led to 409,000 deaths (WHO, World Malaria Report 2020). This primary life-threatening disease is transmitted through the bites of infected female *Anopheles* mosquitoes.

Currently, the primary way to reduce malaria transmission and protect individuals is through the usage of repellents and/or insecticides. However, most mosquito species have become resistant to frequently used insecticides such as organophosphates, carbamates, and pyrethroids [3,4]. Regarding repellents, i.e., volatile substances that make mosquitos escape from a source of smell [5,6], the most effective broad-spectrum insect repellent is *N*,*N*-Diethyl-3-Methylbenzamide (DEET) [7]. Although it is considered safe, several reports in the last decades have indicated its potential adverse effects on human health and the environment [8–12]. Another active ingredient of repellents, 3-(*N*-*n*-butyl-*N*-acetyl)-amino-propionic acid ethyl ester (IR3535), is apparently safer for mammals. Furthermore, it is also known that DEET and IR3535 can elicit diverse modes of action [13–17], and can display novel non-classical effects, that can represent an alternative in the Insect Resistance

Management for preventing the spread of mosquito-borne diseases. They can be used as a synergistic agent [18] to increase sensitivity to insecticides via a complex calcium-dependent intracellular signaling pathway following muscarinic acetylcholine receptor (mAChR) activation [19,20]. Searching for synergistic effects is becoming a popular strategy in the control of insect vector-borne diseases with a particular interest in the cholinergic system [21].

As acetylcholine (ACh) is the major signaling neurotransmitter in the insect nervous system, the ligand-gated ion channels named nicotinic acetylcholine receptors (nAChRs) are suitable targets for several classes of insecticides, including neonicotinoids, widely used in plant protection against insects since the late 1990s [22–24]. By contrast, mAChRs, which are G-protein-coupled receptors (GPCRs), are still unexploited in this area. However, recent studies have reported that insect mAChRs are interesting targets for repellents used as synergistic agents [18–20]. Both DEET and IR3535 were shown to interact with M1 andM3 mAChR subtypes at low concentrations inducing intracellular calcium rise that synergistically increase the insecticide efficacy when mixed with propoxur [19] and thiacloprid [20], respectively. This increased efficiency, based on the positive interaction between two compounds, represents a promising strategy to design more suitable approaches to control insect vector-borne diseases.

While mammalian mAChRs are divided into five subfamilies (M1–M5, Figure 1), three types have been identified in insects: type-A (mAChR-A), type-B (mAChR-B), and type-C (mAChR-C), and characterized in the fruit fly *Drosophila melanogaster* [25,26]. Very recently, mAChR-A have also been described in the malaria-spreading mosquito *Anopheles gambiae* [27]. The most closely homologous to the mammalian mAChRs is mAChR-A, which uses M1/M3/M5 types signaling pathways via activation of $G_{q/11}$ protein and phospholipase C, resulting in the release of Ca^{2+} from internal stores through inositol 1,4,5-trisphosphate [28]. Like human types, it is activated by ACh and muscarine (see structures in Figure 1) and fully inhibited by classical mAChR antagonists such as atropine.

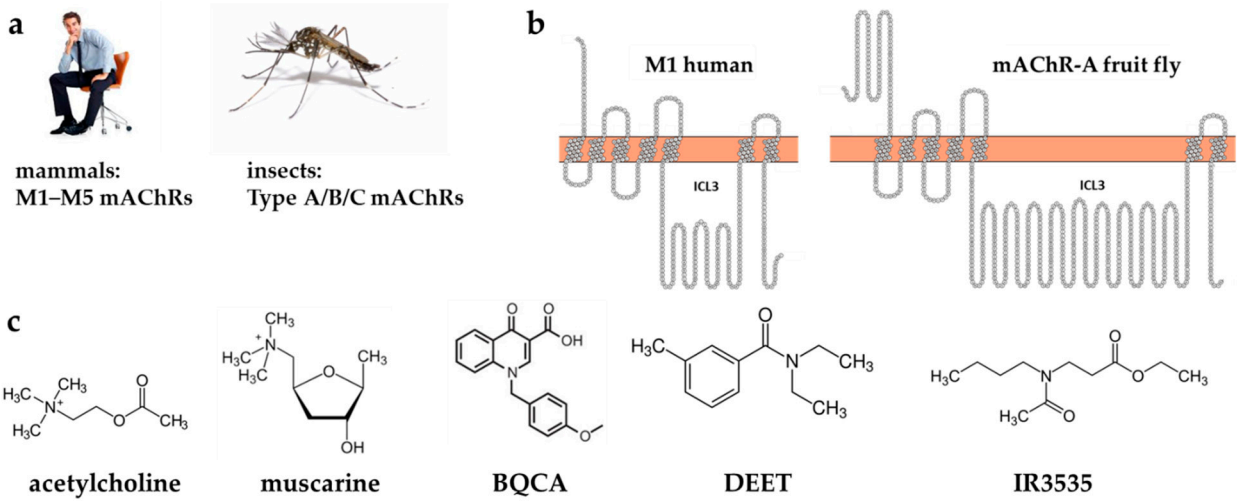

Figure 1. (**a**) Muscarinic acetylcholine receptors (mAChR) are divided into M1–M5 subtypes in mammals and A/B/C types in insects. (**b**) Snake plots [29] of human M1 (left) and fruit fly (*Drosophila melanogaster*) mAChR-A show the main structural features of a GPCR receptor—seven transmembrane helices linked by three extracellular and three intracellular loops among which the third one (ICL3) is the largest. Note that ICL3 is neither present in the human X-ray structure used in this study nor in the fruit fly homology model. (**c**) Structures of classical M1 agonists—acetylcholine, atropine; BQCA modulator and DEET and IR3535 repellents.

Using electropharmacological approaches together with the molecular docking of DEET and IR3535 to static human M1 and M3 receptor models, the ligand-receptor interac-

tions and their mode of action were described [19,20]. However, the expected conformational changes in receptor structure with repellents bound could not be observed with this approach. Here, for the first time, we report on the molecular dynamics (MD) simulations of both insect and human mAChRs with repellent bound ligands.

Recent progress in the structure determination of GPCRs [30,31] triggered numerous studies in virtual screening and structure-based molecular design, which led to the development of new ligands for these receptors. To overcome the problem of limited subtype selectivity in small molecules targeting the highly conserved orthosteric sites (OS), there is a shift towards the allosteric ligands that bind in spatially distinct and less conserved sites (allosteric sites, AS) [32,33]. Allosteric ligands, apart from acting as the subtype-selective agonist or inverse-agonists, can modulate the efficacy and potency of orthosteric ligands. This effect is desirable because when they are used in new repellent formulations, it may allow for the reduction of doses of active substances. The discovery of bitopic (or dualsteric) ligands that occupy both binding pockets simultaneously [34–36] inspired researchers to fuse known orthosteric ligands with their allosteric modulators [37–39]. This approach, although challenging, may lead to the development of high-affinity subtype-selective molecules limiting the off-target activity and side effects of drugs. Therefore, here we propose a novel bitopic compound acting on insect mAChR. To assure a proper distance between the AS and OS ligands and to add a new dimension to chemical pest control, we augmented our design with a light-sensitive unit.

A promising approach that allows for the precise, reversible, and real-time spatiotemporal control of biological signaling is to use light as an external trigger to change a ligand shape and its pharmacological properties. A widely used molecular scaffold that changes structure upon irradiation is azobenzene [40,41]. Azobenzene has two isomers: the thermally stable trans and the thermally unstable cis isomer. Photoswitches, such as azobenzene, can be introduced into the structure of the bioactive ligands to control the activity of the target protein [41]. The mAChRs were the first GPCRs from the rhodopsin family that were successfully modulated by light upon binding of photoswitchable azobenzene-derived ligands [42]. Here we propose one prototype of hypothetically photoactive compound BQCA-azo-IR3535 and model its dynamical interactions with human and insect mAChRs.

The fact that the ligand binds to the receptor manifest in structural changes, often occurring in a place remote from the receptor site. Extensive analysis of all available experimental GPCR structures led to the discovery of a common and conserved activation pathway in class A GPCRs [43]. In this pathway, 34 residue pairs (formed by 35 residues, total) link a ligand-binding pocket with the G protein-coupling region of GPRCs via previously known structural motifs. These include a previously known set of four molecular switches: W6.48 tryptophan toggle switch (in CWxP motif), Y7.53 tyrosine toggle switch (in NPxxY motif), ionic lock involving helices TM3 and TM6 (D/ERY motif in TM3) and 3–7 lock linking helices TM3 and TM7 in the ligand-binding site [44] as well as a sodium ion-binding allosteric site D2.50 [45]. The pathway starts from the ligand-binding region and ends at the G protein interface going through four layers that reflect consecutive stages of the receptor activation.

In this study, we present, for the first time, a homology-based model of insect mAChR-A that may serve as a base for computational studies of repellents-GPCRs interactions. Based on the conserved activation pathway of class A GPCRs [43], we investigate the allosteric changes in mAChRs evoked by selected repellents and M1 modulators binding. All-atom MD simulations enable us to track the subtle, local alterations in the human and insect receptors conformations that accompany an early stage of their activation. Finally, we propose a novel type of bitopic and photoswitchable compound with a potential repellent activity and investigate its effect on mAChR-A dynamics.

2. Results and Discussion

We analyze two closely related molecular GPCR systems: human M1 and insect mAChR-A. The first structure is based on the X-ray data, and the second one is a homology-

based model. One should remember that a direct comparison of results may be somewhat biased due to the hypothetical nature of the starting insect protein structure used for further MD modeling. However, due to the very good templates found for mAChR-A, this bias is acceptable. Reference human 150 ns MD GPCR data are used mainly to facilitate analysis and discussion for longer, 500 ns, insect mAChR-A trajectories.

2.1. Single Ligands Docking

2.1.1. Single Ligands Docking to Human M1 mAChR

In the first step, we performed the molecular docking of eight ligands to the X-ray structure of human M1 mAChR (PDB code: 5CXV) using SMINA code [46], a fork for AutoDock Vina [47]. Ligands selected included repellents (DEET, IR3535), M1 agonists (muscarine, acetylcholine, oxotremorine-M), antagonists (atropine, pirenzepine), and modulators (BQCA, benzoquinazolinone 12). We have chosen the lowest energy poses of each ligand for further analysis. All ligands except pirenzepine and benzoquinazolinone 12 (bqz-12) docked with the best-scored poses in M1 OS, identified by FTSite [48] before docking. Pirenzepine docked well to both orthosteric and allosteric sites, while bqz-12 docked only to the AS. The poses of DEET and IR3535 are shown in the Supplementary Material (SM) Figure S1d,e. Interactions plots for all ligands made using the PLIP server [49] can be found in the SM Figures S2–S5.

DEET and IR3535 occupy the same orthosteric binding site as indicated by the residues ($Tyr^{3.33}$, $Tyr^{7.38}$, $Tyr^{6.51}$, $W^{6.48}$) that gave the highest contribution to the SMINA scoring function (SSF), presented in SM Figure S1b. The experimental alanine substitution of a majority of those residues strongly reduced the affinity of the endogenous agonist acetylcholine and the classical antagonist [50]. Superscripts refer to the Ballesteros–Weinstein numbering [51].

The SSF for DEET is equal to −7.3 kcal/mol. DEET in this pose is stabilized by pi-stacking interaction with $Tyr381^{6.51}$, highly conserved in class A GPCRs. The highest contribution to the energy of binding gave interactions with the aromatic ring of DEET (the structure is shown in Figure 1c and the docking pose in SM Figure S1d). The binding affinity of IR3535 was slightly weaker with SSF = −6.26 kcal/mol.

2.1.2. Single Ligands Docking to the Insect mAChR-A Model

There are no experimental structures for any type of insect muscarinic receptors. To check how the effects of ligands binding manifest in insect type-A receptors, we build the homology model of a fruit fly (*Drosophila melanogaster*) mAChR-A protein (Figure 2a). As the cytoplasmic loop connecting TM5 and TM6 helices (ILC3) is very long (431 residues, more than a half of the whole receptor sequence length, see Figure 1b), the model could be built only after the removal of this intracellular part. Such simplification in GPCR structure modeling is a typical procedure. The dockings of DEET, IR3535, and muscarine were performed using the same protocol as for the human M1 described in the methods section.

In insect mAChR-A, the best docking score (i.e., low SFF value) was observed for DEET (−7.19 kcal/mol), followed by IR3535 (−6.08 kcal/mol). According to our approach, muscarine binds weaker to_mAChR-A (SFF = −5.79 kcal/mol). The order of these numbers is the same for the human M1 GPCR, but the binding affinity is predicted to be slightly weaker (ΔSFF = 0.1–0.2 kcal/mol). Similar to M1, in the insect receptor, the strongest stabilization of ligands comes from aromatic residues (five out of six presented in Figure 2e). The lists of most stabilizing residues in both receptors are identical (cf. Figure 2e and Figure S1b). Clearly, the tryptophan toggle switch ($Trp^{6.48}$) plays a major role in the OS of both receptors. This strong similarity in repellents' affinity to insect and human receptors may indicate possible physiological effects of DEET in humans, induced via the M1 activation pathway. The docking is only a computational procedure, sensitive to numerous parameters, including details of the hypothetical docking site geometry. However, it is an interesting observation that IR3535 shows weaker binding than DEET, so its negative effect is expected to be somewhat weaker.

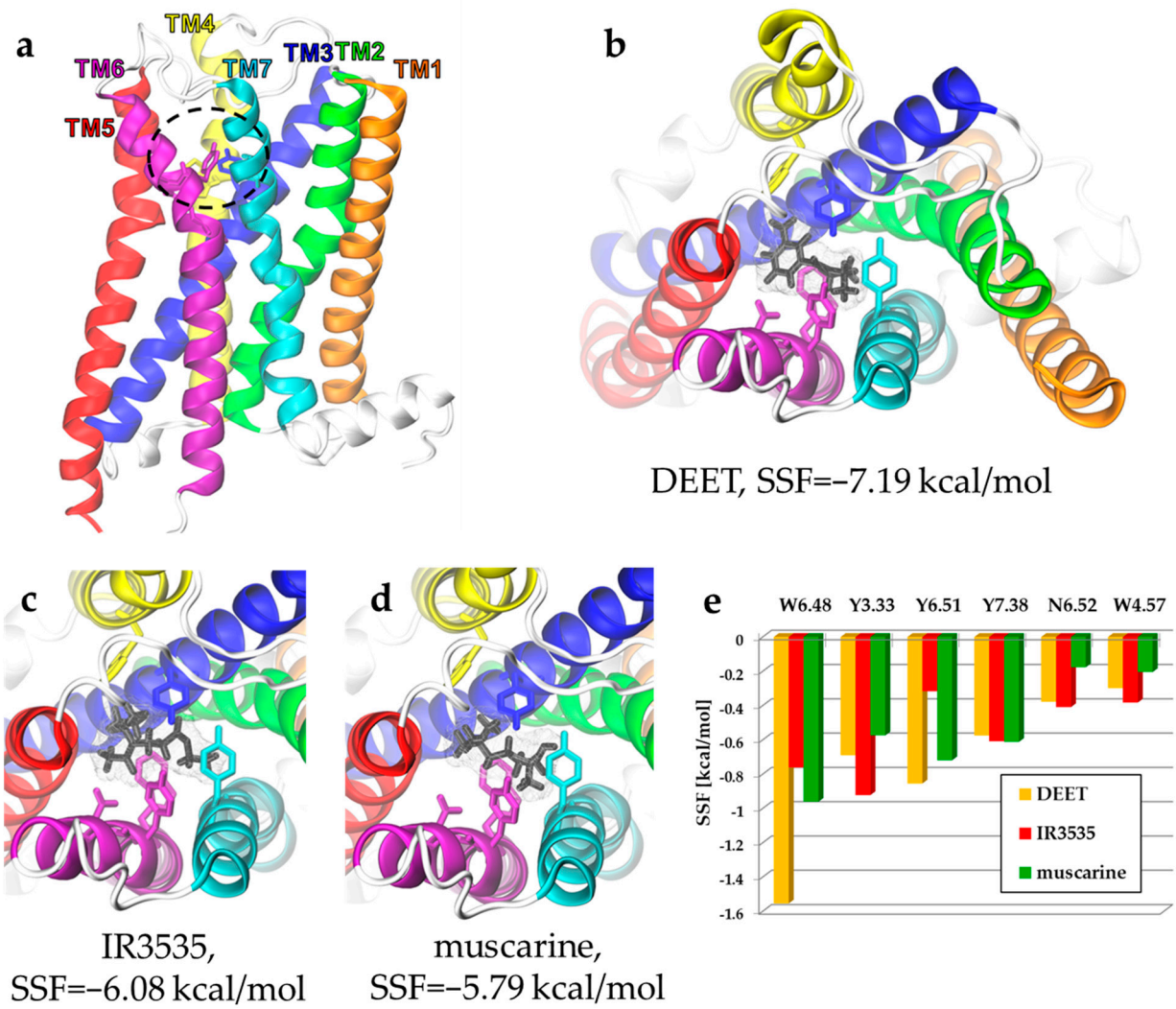

Figure 2. (**a**) The homology model of *Drosophila melanogaster* mAChR-A receptor based on the UniProtKB P16395 (ACM1_DROME) sequence and human M1 structure template (PDB code: 5CXV). The orthosteric binding-site region is marked with a black dashed line. (**b**–**e**) SMINA molecular docking of insect repellents DEET (**b**) and IR3535 (**c**) and classical agonist muscarine (**d**) to the homology model shown in (**a**). Top views are presented. (**e**) Docking energy decomposition presented as SMINA scoring function (SSF) in kcal/mol shows interacting ligand residues of the mAChR-A orthosteric binding site.

2.2. What Happens upon Ligand Biding? Dynamical Response of Human M1 Receptor

Ligands present in the orthosteric (or allosteric) site exert their biological roles by changing the conformation of GPCRs. The transduction of those signals to remote places such as the G-protein binding site requires mechanical interactions occurring within the receptor body. Tightly packed helices, present in the intramembrane part, facilitate this task but not all out of hundreds (>800) possible residue–residue contacts are critical for such signal transduction. The role of such contacts in M1 and mAChR-A has not been investigated thus far. The whole process of triggering a response to a ligand is too long for computational investigation, but the important initial stages of signal transduction may be monitored using MD simulations on hundreds of ns timescale. Thus, to get a dynamical picture of repellents induced changes in GPCRs, we performed MD simulations and analyzed closest contacts in regions delineated in extensive studies by Zhou et al. of all available X-ray type-A GPCR structures [43].

In the first step, the lowest energy docking poses were used as starting points for the MD simulations of the M1 receptor embedded in a lipid bilayer. We performed three repetitions of 150 ns long MD for M1 receptor without ligand (APO) with DEET, IR3535, and muscarine. RMSD plots indicate (data not shown) that reasonable convergence has been achieved in our relatively short simulations.

On a relatively short timescale exploited here, the analysis of contacts with the GetContacts server [52] or RRCS contact scores using a method introduced recently [43] may be illuminating.

RRCS is an atomic distance-based parameter that quantifies the strength of contact between residue pairs by summing up all possible inter-residue heavy atom pairs without weighting factors [43]. Not only does it capture side-chain repacking if the backbone atoms of the two residues are close to each other, but it also describes local contacts involving adjacent residues (excluding backbone atoms of residues that are within four amino acids in protein sequence). Thus, RRCS can be used as a quantitative descriptor of dynamical contact rearrangement in protein and a useful tool for the comparison of multiple receptor states. Zou et al. performed RRCS calculations on all available high-resolution 3D structures of class A GPCRs comparing their active and inactive states. The universal signal transduction path has been proposed consisting of 34 pairs of AA [43]. Unfortunately, it is not known how such RRCS values evolve over time, how they change upon ligand-binding, and to what extent the indicated critical contacts last.

2.2.1. GetContacts

To examine the initial response of the M1 receptor to the ligands, we calculated fractions of simulation frames in which a given residue pair, found in [43] as a part of the signal transduction pathway, form a contact. In Zhou et al. meta-analysis [43], two types of structural response upon ligand-binding were postulated: (i) some residue residue pairs increase their contact frequency in the activated form of GPCR with respect to the apo or inactivated protein, and (ii) other pairs decrease contacts frequency. Initially, we used for the analysis GetContacts server [52]. Here, Van der Waals contacts (vdw) between two atoms are registered if the distance between their centers is less than the sum of their van der Waals radii plus an epsilon value of 0.25 Å. Data for representative 14 pairs (out of 34 indicated by Zhou et al.) that exhibited the most profound variations between molecular systems are shown in Figure 3. Contacts between other residues pairs from the pathway set of Zhou et al. [43] were not affected by the presence/absence of our ligands.

Such a dynamic picture is very interesting. Indeed, all pairs which were predicted to decrease contacts upon agonist binding show a decrease in our MD calculated contact fraction (see Figure 3, left panel) and vice-versa: all residue pairs that should increase their contacts when the ligand comes into the orthosteric site do have substantially higher contact fraction (Figure 3, right panel). We estimated the global effect (GE) of ligand-binding using the following metric:

$$\mathrm{GE}+ = \sum_{i=1}^{7} \left(\mathrm{ACF}(+)_i^{\mathrm{APO}} - \mathrm{ACF}(+)_i^{\mathrm{LIG}}\right)^2$$

$$\mathrm{GE}- = \sum_{i=1}^{7} \left(\mathrm{ACF}(-)_i^{\mathrm{APO}} - \mathrm{ACF}(-)_i^{\mathrm{LIG}}\right)^2,$$

where ACF(+/−) are averaged contact fractions (see Figure 3) for gain and loss in contact frequency, respectively, LIG = DEET, IR3535, or muscarine.

From Table 1, one can see that DEET exerts its effect on M1 GPCR in a similar way as muscarine, but the decrease of frequency contacts (GE− = 0.829) is much weaker than that for muscarine (DE− = 1.682). IR3535 basically does not increase the contacts between critical pairs but strongly reduces that number for another set of residues, its GE− of 1.30 is close to GE− calculated for muscarine.

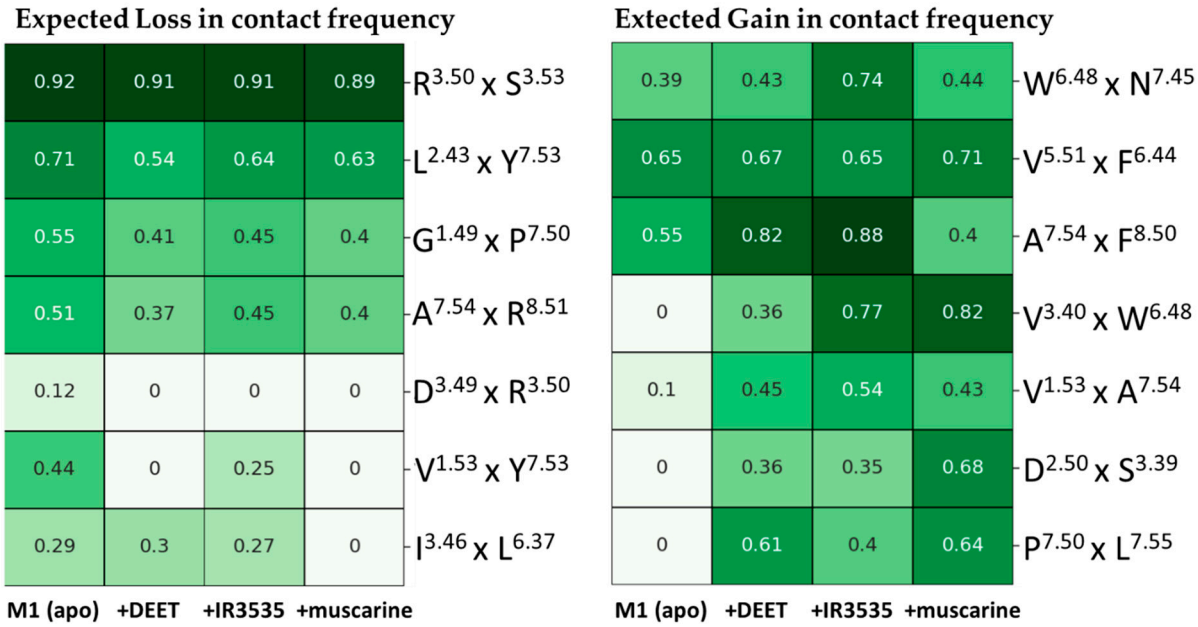

Figure 3. Average contacts as a fraction of total simulation time (450 ns) [52] observed for M1 apo and for M1 having DEET, IR3535, and muscarine ligands in the orthosteric site.

Table 1. Parametrization of global effects of ligands on averaged contact fractions.

Parameter	DEET	IR3535	Muscarine
GE+	0.276	0.070	0.334
GE−	0.829	1.300	1.682

We found that for our three agonists, in general, the highest gain in contact frequency in human M1 was observed between the tryptophan toggle switch Trp378$^{6.48}$ with Val113$^{3.40}$, the residue contributing to the sodium ion binding pocket Asp71$^{2.50}$ with Ser112$^{3.39}$ and between residues located on the H7 Pro415$^{7.50}$ and Lys420$^{7.55}$. Loss of contacts was noted in highly conserved DRY motif Asp122$^{3.49}$ × Arg123$^{3.50}$, Val46$^{1.53}$ with the tyrosine toggle switch Tyr418$^{7.53}$ and in interactions of I119$^{3.46}$ with the microswitch Lys367$^{6.37}$.

2.2.2. Analysis of Residue-Residue Contact Scores in Human M1

The recently proposed [43] residue–residue contact scores (RRCSs) are better suited for the analysis of the subtle effects in GPCR structure induced by ligands than the simple contact fraction presented in the previous section. RRCS takes into account further located atoms and is defined as:

$$\mathrm{RRCS} = \sum_{i \in A} \sum_{j \in B} \delta_{ij}$$

where,

$$\delta_{ij} = \begin{cases} 1 \; r_{ij} \leq r_{min}, \\ 0 \; r_{ij} \geq r_{max}, \\ \left((r_{max} - r_{min})^{-1}(r_{max} - r_{ij})\right) \text{ otherwise}, \end{cases}$$

and r_{ij} is the distance between i and j-th atom, and r_{min} = 3.23 Å and r_{max} = 4.63 Å. In our case, group A contains atoms of one residue of the investigated pair and group B consists of atoms belonging to the other residue in the analyzed pair.

We applied this approach to investigate differences in contacts between all 34 key residue pairs of the M1 receptor caused by agonist muscarine and repellents DEET and IR3535. Half of the 34 residue pairs contacts were not affected by interactions with ligands. Therefore, we limited the further analysis to nine pairs that increased contacts upon muscarine binding (Figure 4, green lines) and eight pairs that decreased (or loose) con-

tacts while ligand-bound (Figure 4, red lines). Among them, 5 were intrahelical and 12 were interhelical.

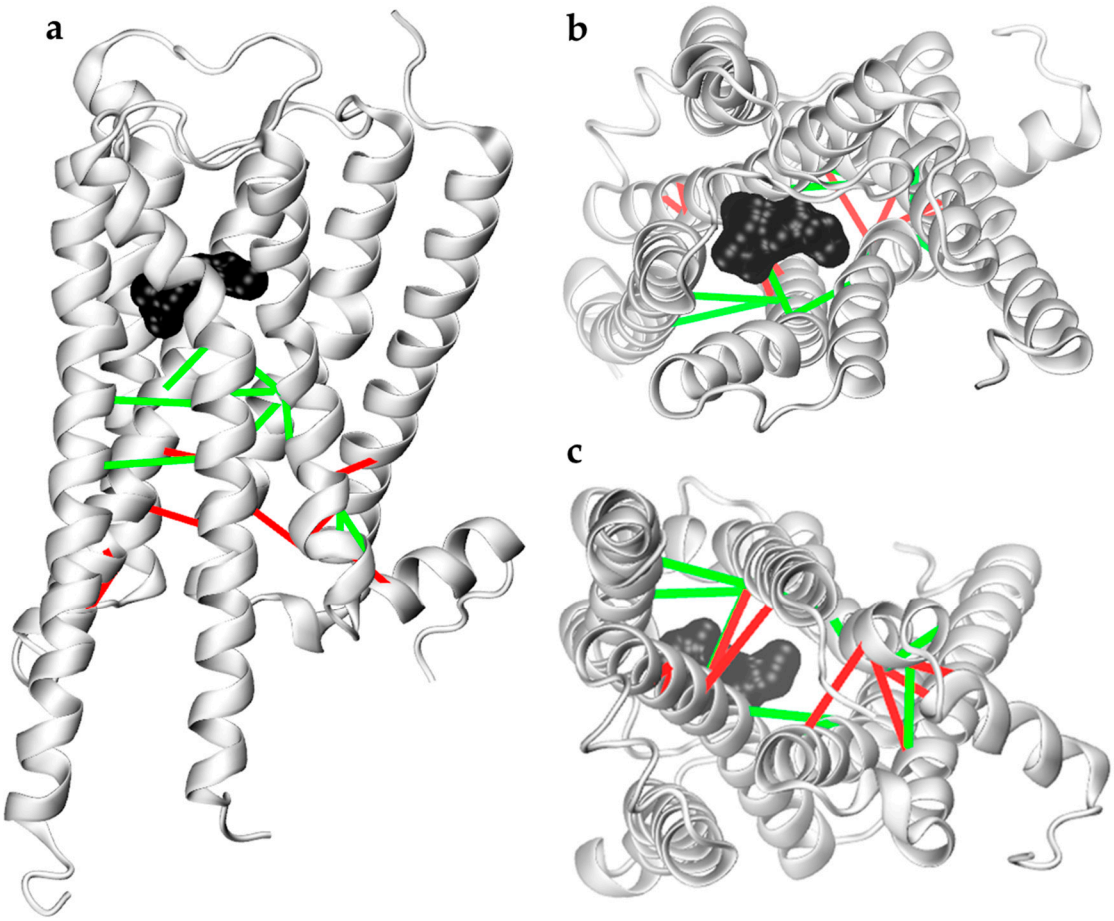

Figure 4. Contacts between key residue pairs involved in the first stage of M1 receptor activation discussed in this paper. (**a**) Side, (**b**) top, and (**c**) bottom views of M1 are shown with distances that increase (green) and decrease (red) upon activation, represented by lines. IR3535 is shown in black surface representation to indicate the position of the orthosteric binding site.

In Figure 5a,b we show RRCS histogram plots for the bare M1 receptor (apo, grey) and M1 with a ligand in its orthosteric site: muscarine (green), DEET (orange), and IR3535 (red). Figure 5a presents the contacts that were strengthened during activation, while in Figure 5b, the residue pairs that loosened contact during activation are shown. Histograms of the RRCSs for other interesting but less affected RRCS are presented in the SM Figure S6. The effect of muscarine is clearly seen as this ligand moved the mean RRCS values of M1 residue pairs towards the active form of GPCR (residue pairs from Figure 5a are much closer than in the apo form, while those in Figure 5b have loosened their short distances). We found that the effect of repellents was located somewhat in between APO and muscarine, and IR3535 increases contacts to a larger extent than DEET does. Notably, the indicated residues corresponded to the known, highly conserved classical points of GPCR activity regulation: the residue contributing to the sodium ion binding pocket Asp71$^{2.50}$, the hydrophobic lock Leu116$^{3.43}$, Asp122$^{3.49}$, and Arg123$^{3.50}$ from the DRY motif, the microswitch Leu367$^{6.37}$, the tryptophan toggle switch Trp378$^{6.48}$, and the tyrosine toggle switch Tyr418$^{7.53}$ [44].

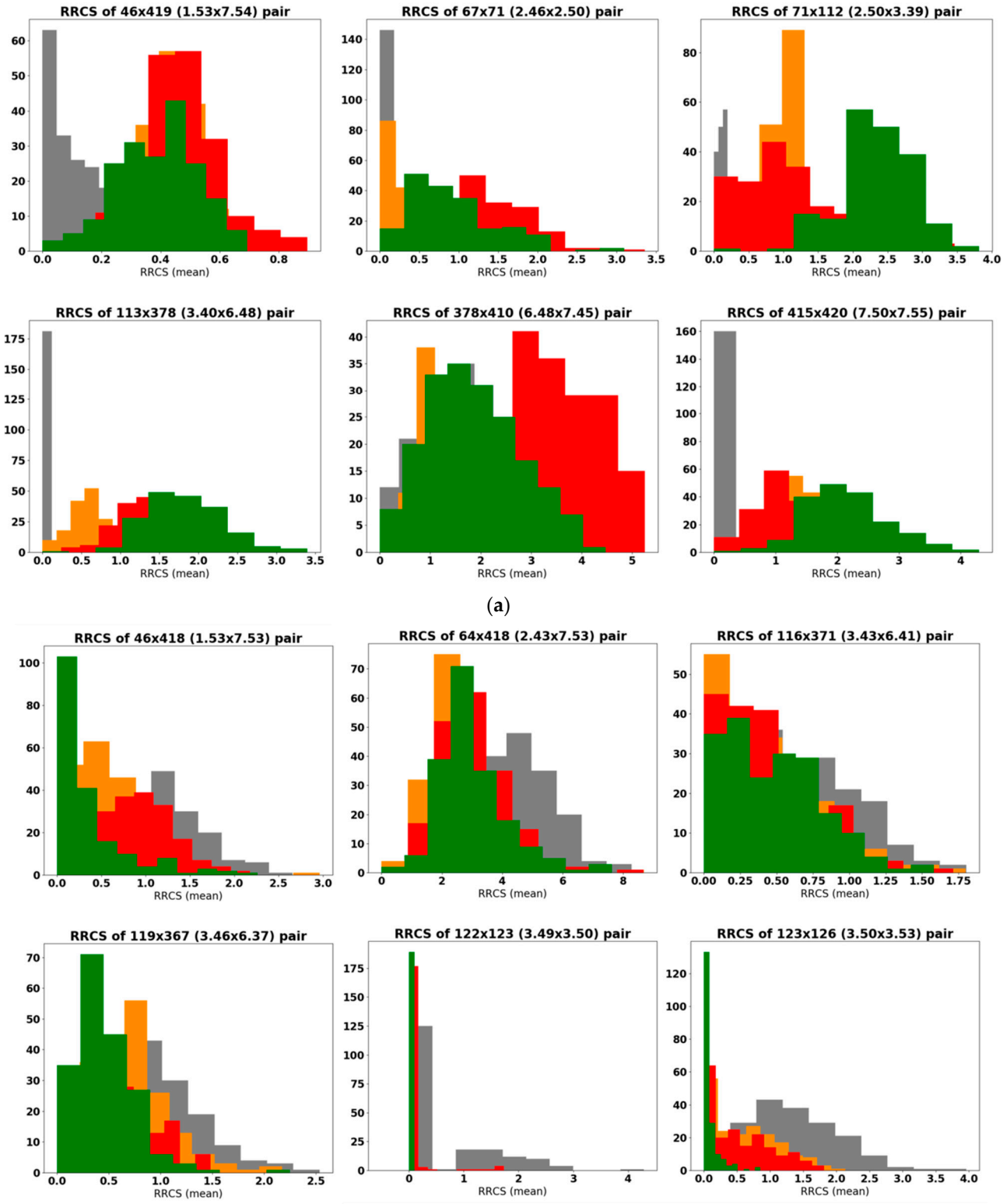

Figure 5. (**a**,**b**) Histograms of residue–residue contact scores (RRCSs). Sampling was 1 frame/0.8 ns of 150 ns MD simulation (average of 3 repetitions). Contacts that increase (**a**) and decrease (**b**) RRCS are shown for M1 apo receptor in grey, M1 with muscarine in green, M1 with DEET in orange, and M1 with IR3535 in red.

The shapes of the RRCS histograms allow for the qualitative assessment of the mobility of a given amino acid pair: the wider the distribution, the more flexible the re-

gion. In Figure 5a, we see a strong impact of the ligands on Val113$^{3.40}$ × Trp378$^{6.48}$ and Pro415$^{7.50}$ × Leu420$^{7.55}$ pairs, since, in M1 apo, there was no contact, but in the ligands' activated forms, such contacts were formed. Notably, the most important pairs involved in the GPCR activation process determined by the GetContacts server [52] were also independently discovered in our more precise RRCS analysis.

2.2.3. In Search for Repellent Modulation: Sequential Docking and Dynamics of the Human M1

In M1 GPCR, both OS and AS may be occupied by small ligands at the same time. We expect that an extra ligand in AS may enhance selectivity and the action of repellents by a positive allosteric modulation. To develop a bitopic ligand with a repellent function that could occupy both sites simultaneously, we examined how the presence of allosteric modulators influences the effect of repellents on the receptor structure. We docked pirenzepine to the M1 with DEET or IR3535 in the orthosteric site of M1 (Figure 6). The same study was repeated for the modulator/agonist BQCA. Those four systems dynamics were simulated (150 ns × 3 repetitions for each system) to monitor RRCSs structural parameters and to compare with the single ligand cases.

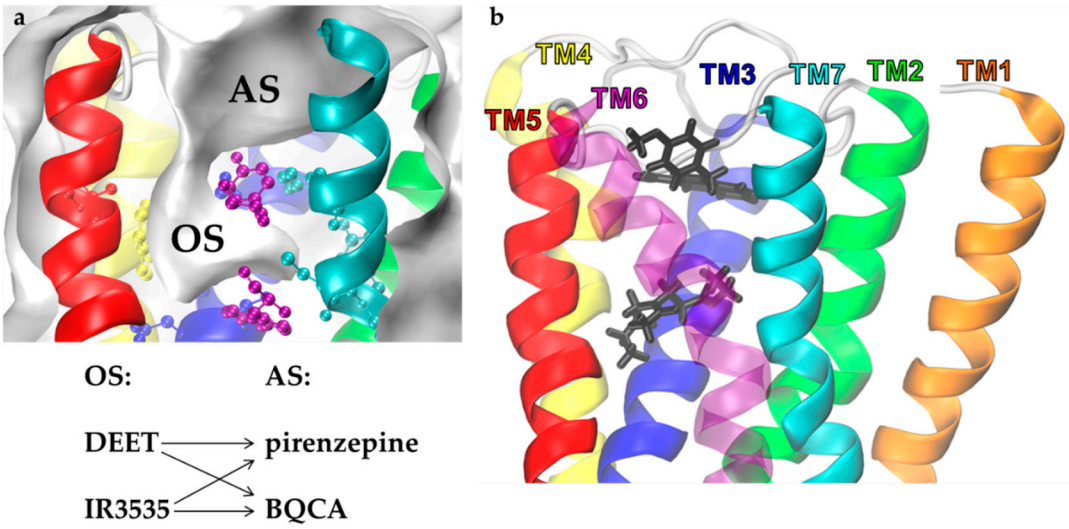

Figure 6. Multiple molecular docking of insect repellents and modulators to the human M1 muscarinic receptor. (**a**) Surface representation of orthosteric (OS) and allosteric (AS) sites of M1 receptor and scheme of multiple docking protocol. (**b**) Docking poses of IR3535 in the OS (bottom, black) and BQCA in the AS (top, black); the key residues of OS are marked.

We analyzed all pairs from the consensus signal transduction pathway in which RRCS were affected by DEET or IR3535 (see Figure 5a,b and Figure S7a,b), looking for the modulatory effect of allosteric ligands. The presence of both pirenzepine and BQCA reduced the impact of DEET on RRCS values (data not shown). We expected that those modulators would not potentiate DEET repellent activity.

More promising results were found for IR3535. While pirenzepine slightly and negatively modulated the action of IR3535, we observed symptoms of positive modulation of IR3535 impact on M1 by BQCA docked to AS (results of RRCSs from MD are presented in SM Figure S7a,b as reference data and are discussed further). Based on this observation, we proposed a new, possibly photoswitchable compound composed of BQCA, a linker, and IR3535 (BQCA-azo-IR3535). As a linker, we applied azobenzene since it has a proper size and useful photophysical properties. The structure of this test molecule is shown in Figure 7.

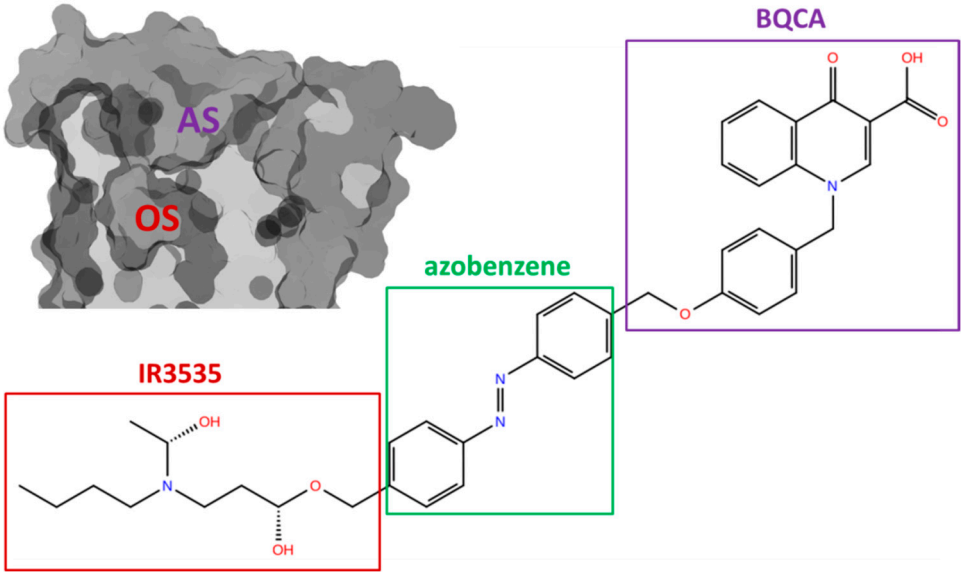

Figure 7. Structure of the bitopic, photoswitchable insect repellent BQCA-azo-IR3535 with parts that target orthosteric (OS, red) and allosteric (AS, violet) sites of the muscarinic acetylcholine receptor (left side) indicated in red and purple boxes, respectively.

2.3. Computer Modeling of Designed Bitopic Ligand (BQCA-azo-IR3535)

Bitopic ligands designed for better modulation of the mAChRs were studied in the past. For example, the M2 agonist Phthalimide-Azo-Iperoxo, which links the fragments of muscarinic agonist iperoxo and allosteric modulator W84 via azobenzene functional group, was proposed recently by Riefolo et al. [53]. Azobenzene in its ground state was extended, i.e., trans conformation. It activated the M2 receptors and can be reversibly photoswitched to enable precise spatiotemporal control of cardiac function [53]. Another bitopic ligand—BQCAAI—was obtained by connecting the agonist iperoxo with the positive allosteric modulator BQCA through an azobenzene linker as well. Strikingly, cis-BQCAAI acts as an antagonist (under 366 nm) of the M1 receptor, while trans-BQCAAI is an agonist (under dark conditions or 455 nm illumination) [39]. These results inspired us to search for a similar system with repellents as main part ligands. Using a molecular builder (see Methods), we drafted a skeleton and optimized the geometry of the BQCA-azo-IR3535 derivative (see Figure 7).

2.3.1. Bitopic BQCA-azo-IR3535 Ligand Effect on Human M1 GPCR

As expected, SMINA molecular docking of IR353-azo-BQCA to human M1 receptor showed that the IR3535 part occupies the orthosteric site, while the modulator part (BQCA) was docked in the allosteric site (see a comparison of IR353-azo-BQCA docking poses in human and insect receptor in SM Figure S8). The trans-azobenzene linker fits into a narrow grove connecting the pockets. The binding energy (SSF) was equal to −11.35 kcal/mol, while for IR3535 alone, SSF was −6.26 kcal/mol and for BQCA −8.6 kcal/mol. Thus, our bitopic ligand should have a higher affinity towards M1 than any of these two ligands.

The lowest energy pose of BQCA-azo-IR3535 was used for MD simulations (3 × 150 ns) of the ligated M1 receptor. The comparison of RRCS values for an M1 receptor with IR3535 alone and IR3535 together with unlinked BQCA and the receptor with BQCA-azo-IR3535 are shown in the histogram plots in SM Figure S7a,b.

Our large, bitopic ligand affects contacts between critical residues of human M1 in a way that is not a simple superposition of BQCA and IR3535 ligands effects (SM Figure S7a,b). In general, we do not observe the strengthening of contacts in the receptor with BQCA-azo-IR3535 (in comparison to the APO form), but rather the loosening of M1 packing is seen. In the RRCSs analyzed here, the contacts of helix H6 are present six times. This helix is particularly important since it made an outward movement upon GPCR activation. The

bitopic ligand exerted no modulatory effect in tightening contacts on those pairs. However, a strong loosening of H6 (Leu116$^{3.43}$ × Leu371$^{6.43}$ and Ile119$^{3.46}$ × Leu367$^{6.37}$) induced by this ligand was observed. Of special interest is the 116$^{3.43}$ × 371$^{6.41}$ pair, which, together with the 116$^{3.43}$ × 370$^{6.40}$, is known as the hydrophobic lock [44]. This region was loosened as 116$^{3.43}$ × 371$^{6.41}$ contacts decreased to zero in 1/3 of BQCA-azo-IR3535 simulation frames. Such reduction is even stronger than that induced by muscarine (Figure 5b). The effect of BQCA-azo-IR3535 on the Ile119$^{3.46}$ × Leu367$^{6.37}$ microswitch pair was comparable to that exerted by muscarine.

The MD results are encouraging in the sense that the good quality M1 structure was not affected much, and a strong affinity for the bitopic ligand was predicted. Now, we have a good reference point for more extensive MD studies of bitopic ligand action in insect mAChR-A.

2.3.2. Bitopic BQCA-azo-IR3535 Ligand and Insect mAChR-A Dynamics

We docked BQCA-azo-IR3535 ligand to human and insect GPCR models using the same methodology (Figure 8). Similar to the M1 receptor in mAChR-A, the BQCA part went to AS, and IR3535 part fit well into the orthosteric cavity. The total SSF value for the bitopic ligand-binding to the insect receptor equals −11.97 kcal/mol (while −11.35 kcal/mol was obtained for the human M1). The docking energy decomposition showed that the highest contributions to the binding of BQCA-azo-IR3535 again produced the aromatic residues (Figure 8b). Most of the binding energy came from the interaction of the repellent part with the OS. Only three of these residues (W$^{7.34}$, Y258 from the extracellular loop 2, and F$^{2.60}$) contributed to the BQCA part binding in the AS, while the T5.40 interacted with the azobenzene linker. The comparison of BQCA-azo-IR3535 docking poses to the aligned M1 human and insect mAChR-A structures, together with the energy decomposition, are provided in SM Figure S8. To investigate the differences between the repellents binding to the active state receptors, we performed docking of the DEET, IR3535, and BQCA-azo-IR3535 to the X-ray structure of human M1 in its active state (PDB code: 6OIJ) to the insect mAChR-A model built using this template, and also to the most recently released human M1 structure (PDB code: 6ZG9). SSF values can be found in the SM Table S1.

To assess the action of the BQCA-azo-IR3535 ligand on insect receptor dynamics, we performed longer MD simulations of mAChR-A without a ligand (APO) and with IR3535, muscarine, and bitopic ligands. Three independent 500 ns simulations were run for each system (note that the simulation time was over three times longer than for the human M1 receptor, so conformational space for the less reliable model is well sampled).

The protocol used was the same as for the M1 receptor (see Methods) with the plasma membrane composition modification to obtain more insect-like lipid content.

The plasma membrane in which receptors are embedded provided not only a neutral environment but also affected the ligand affinity [54]. The majority of MD simulations of membrane proteins had been performed assuming in human-like membrane models (usually phosphatidylcholine: POPC or DOPC). However, flies differ in their lipid composition from humans substantially. Insects have an inverted and four times higher phosphatidylethanolamine to phosphatidylcholine ratio than mammals [55]. Thus, using CHARMM-GUI [56], we created a heterogeneous bilayer model composed of: 38% DOPE, 18% DOPS, 16% DOPC, 13% POPI, 11% SM (CER180), 3% DOPG and 1% PALO 16:1 fatty acid. Data from the MD showed that BQCA-azo-IR3535 was more tightly bound to the insect receptor than to the human one (Figure 9). In Figure 9a, we present dynamical changes in values of SSF, which are proportional to binding affinity, for numerous MD structures "on-the-fly". Except for one "outlier" trajectory (grey in Figure 9a,c,d), we observed that the SFF for the bitopic ligand in insect GPCR for the first 150 ns is systematically lower (Figure 9a) than that calculated for the human M1. We extended our simulations for the insect mAChR-A, and, indeed, the good SFF values were kept low throughout the whole simulation. The same analysis performed for the IR3535 ligand showed no differences between those species (Figure 9b). This conclusion is supported by the convolutional neural

network (CNN) data (Figure 9c). The CNN scoring function, measured in "pK" units, may be easily converted to the ligand affinity, where 1 μM is 6, and 1 nM is 9, so the higher CNN, the better. Thus, affinity towards the humans calculated using GNINA software [57] was around 1 μM, and towards the insects, close to 10 nM. We inferred that the bitopic ligand should have a stronger physiological effect in insects than in humans.

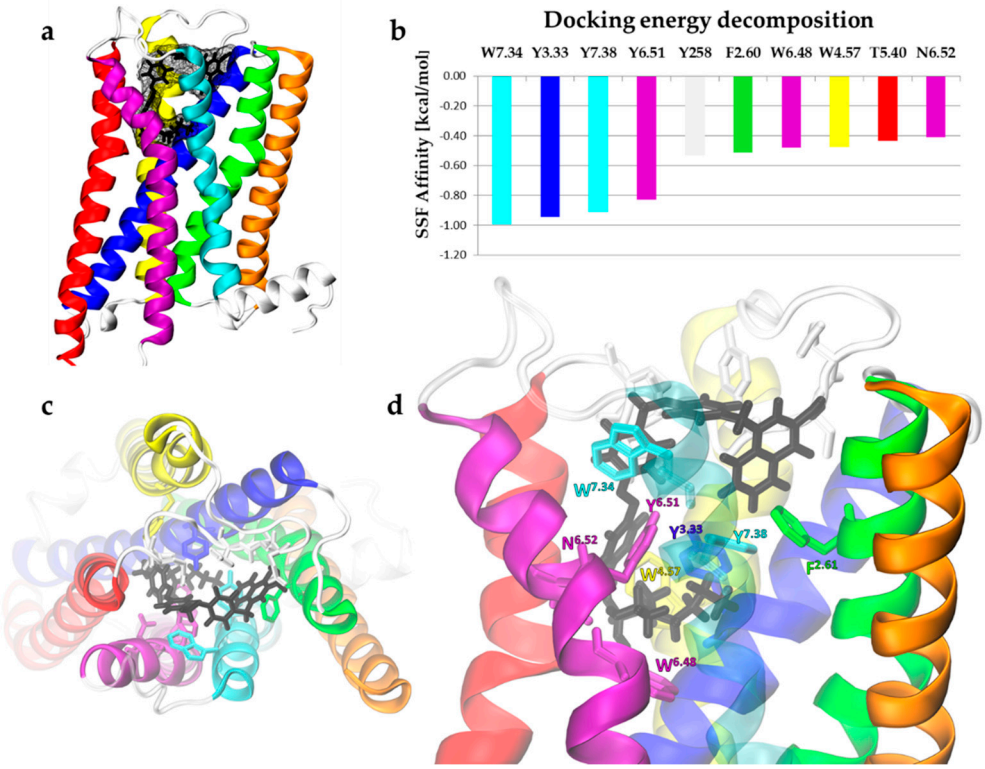

Figure 8. Molecular docking of bitopic ligand BQCA-azo-IR3535 to the homology model of *Drosophila melanogaster* mAChR-A. (**a**) Receptor structure with the ligand-bound (black licorice and surface representation). Note that intracellular loop 2 was removed from the model. (**b**) Docking energy decomposition shows residues giving the highest contribution to the affinity of ligand-binding. These residues are marked in (**d**). The top view (**c**) and the side view (**d**) of the BQCA-azo-IR3535 (black) docked to the mAChR-A.

The space occupied by the bitopic ligand in both receptors was very large. The overlaps of all positions occupied by non-hydrogen atoms of BQCA-azo-IR3535 (yellow) in M1 (blue) and mAChR-A (red) receptor during three repetitions of MD trajectories are shown in Figure 9e,f, respectively. The ligand was bound deeper in mAChR-A, and moved towards the sodium ion pocket identified as a highly conserved $D^{2.50}$ residue (Figures 9f and 10a). Note that one mAChR-A trajectory (shown in gray in Figure 9f) is perhaps an outlier: in the last 30% of the 500 ns trajectory, the ligand shows a tendency to leave the allosteric pocket. The evolution of the distance between the ligand and the $D^{2.50}$ residue is shown in Figure 9d. The small and flexible endogenous agonist acetylcholine was found to be able to diffuse from the OS into the new binding site next to the $D^{2.50}$ residue of M3 and M4 muscarinic receptors [58]. The sodium ion located at $D^{2.50}$ was present in inactive conformations of most GPCRs, but not in agonist-bound ones. As a negative allosteric modulator of receptor activation, it stabilized the inactive state of the receptor, decreased affinities for agonists, and enhanced affinities for some antagonists [59]. A strong sensitivity to the sodium ion has been shown for a negative allosteric modulator SB269652 that adopted an extended bitopic pose in the dopamine D2 receptor and completely lost its modulatory effect in the absence of sodium ion [60]. In turn, BMS986122, a positive allosteric modulator of the μ-opioid receptor, was found to exert its effect through disruption of the sodium binding,

thereby promoting receptor activation [61]. We speculate that a similar effect may happen for the BQCA-azo-IR3535 ligand-bound into mAChRs.

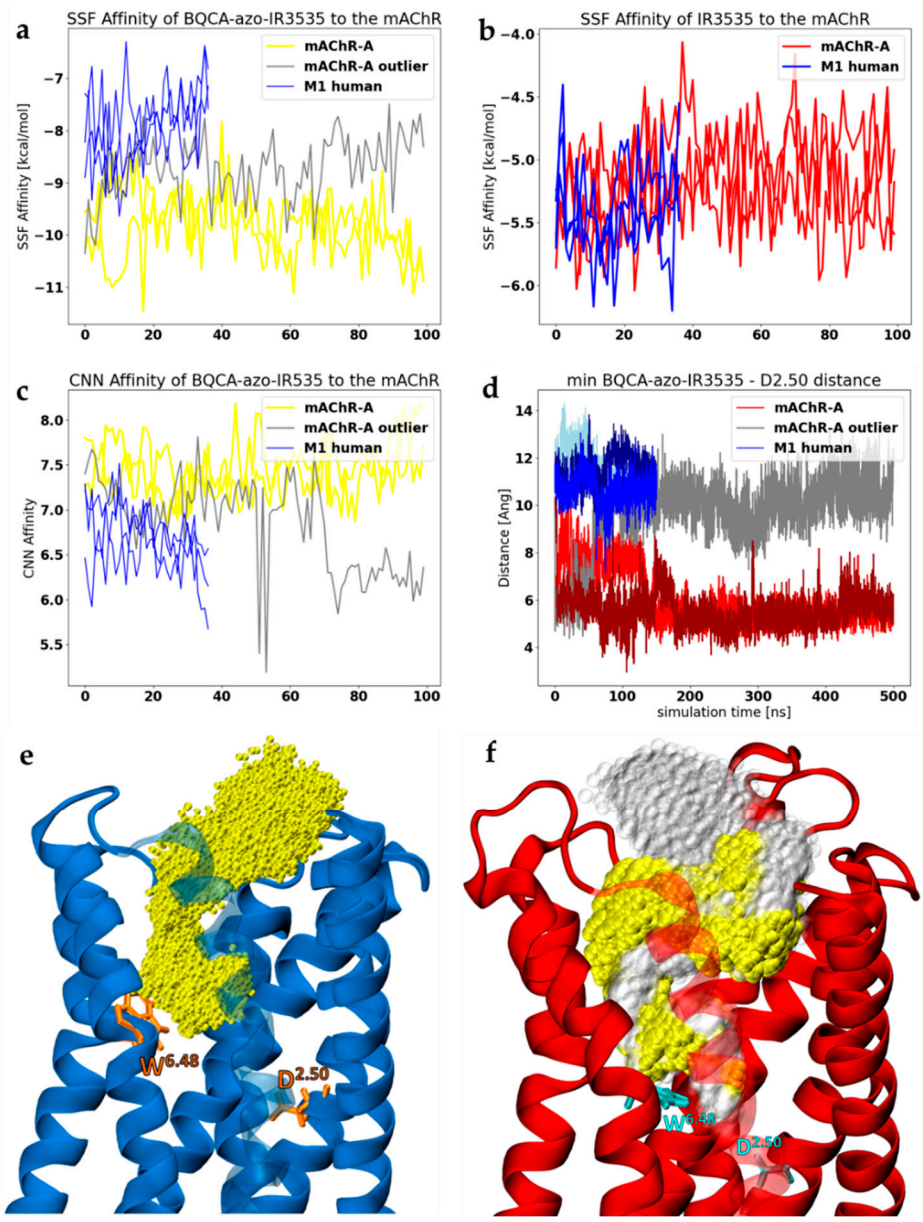

Figure 9. BQCA-azo-IR3535 interaction with mAChRs. The SSF affinity evolution for bitopic ligand (**a**) and IR3535 (**b**) are shown for mAChR-A and, for the reference, for the human M1 receptor. (**c**) The convolutional neural network (CNN) scoring function, measured in "pK" units where 1 μM is 6, 1 nM is 9, is plotted for BQCA-azo-IR3535 interaction with mAChRs. (**d**) The distance [Å] between the closest non-hydrogen atom of a ligand and the $D^{2.50}$ residue (sodium pocket) of human M1 (blue) and insect mAChR-A (red and grey). (**e**,**f**) Positions occupied by non-hydrogen atoms of BQCA-azo-IR3535 (yellow) in the human M1 receptor (**e**) and insect mAChR-A model (**f**). The $W^{6.48}$ and $D^{2.50}$ residues are marked (orange in human and cyan in insect mAChR) as indicators of the distance between ligand OS and the sodium ion-binding site. For all plots, data collected from the 3 × 500 ns MD simulation for the human M1 receptor and 3 × 500 ns for the insect mAChR-A are shown.

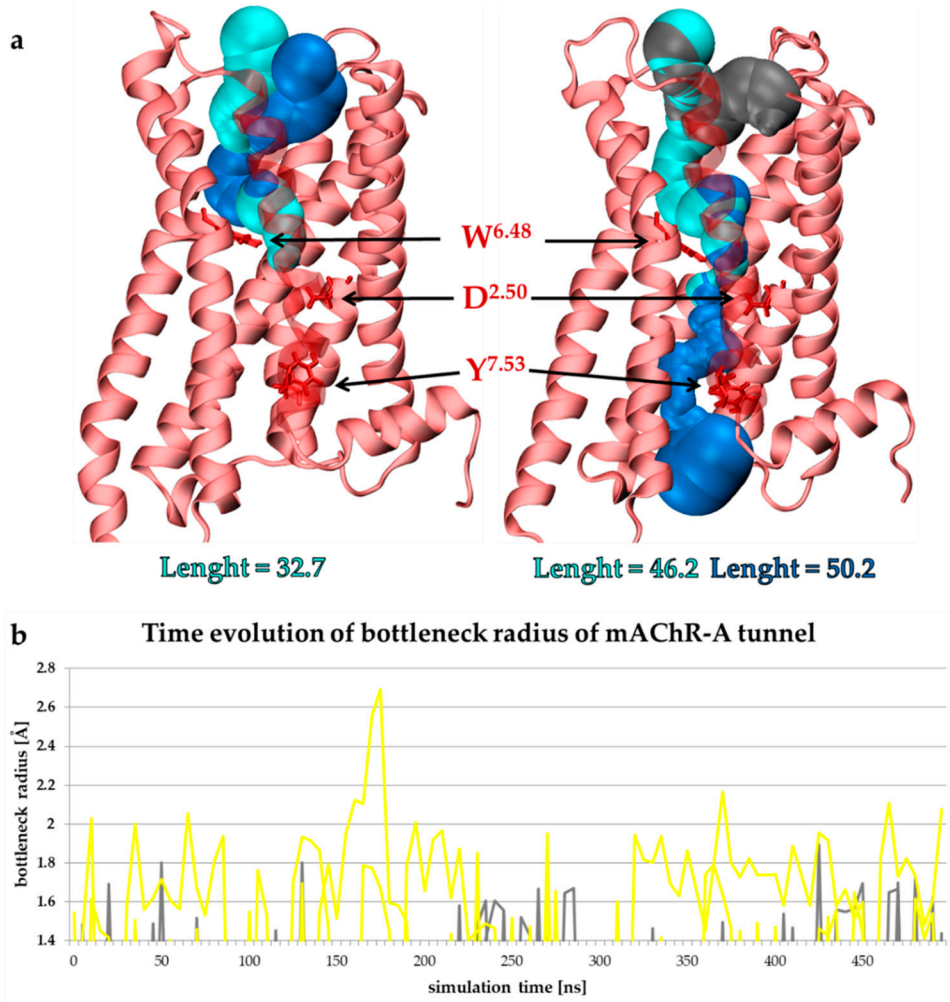

Figure 10. (**a**) Tunnels were found in insect mAChR-A receptor at the minimized and equilibrated structure (left) and in the representative MD snapshot of the receptor with BQCA-azo-IR3535 ligand. (**b**) The bottleneck radius of the tunnels created below the ligand-binding site allows water flow (i.e., with the bottleneck radius higher than 1.4 Å). In gray, the tunnels found in the 3 × 500 ns MD of the APO mAChR-A are shown, while in yellow, those found in the receptor with the bound BQCA-azo-IR3535. Tunnels were visualized using MOLE 2.0 [62], and the bottleneck analysis was performed with CAVER [63].

Water plays an important role in GPRC-mediated signaling. We investigated the formation of the tunnels in mAChR-A. (Figure 10). While the hydrophobic layer was present at t = 0 and water cannot flow through the receptor (Figure 10a, left panel), the presence of BQCA-azo-IR3535 ligand promoted the formation of a tunnel between the OS and the G-protein binding site (dark blue in Figure 10a, right panel). The bottleneck was formed by a tryptophan toggle switch $W^{6.48}$ (part of the CWxP motif). The disruption of water-mediated interactions between $W^{6.48}$ and $D^{2.50}$ was critical for the receptor activation, as the incoming water that passed the $W^{6.48}$ gate changed the conformation of the tyrosine toggle switch $Y^{7.53}$ (part of the NPxxY motif) to allow a continuous pathway of water molecules to the cytoplasm [44]. We investigated the dynamic changes of the bottleneck radius in 3 × 500 ns MD trajectories of mAChR-A with no ligand (APO, grey in Figure 10b) and with the bitopic-bound ligand (yellow in Figure 10b). The instances of bottleneck radius value >1.4 Å are shown to illustrate the fraction of MD in which the water flow is allowed. The difference between the APO and ligand-bound receptor conformation is evident.

Finally, we return to the RRCS analysis. Data for 500 ns long simulations for the insect APO mAChR-A and the receptor with muscarine, IR3535, and BQCA-azo-IR3535 ligands are presented in Figure 11a,b. In a few cases, significant changes in the RRCS patterns induced by ligands were observed. The most striking effect we saw was for the $Val^{3.40} \times Trp^{6.48}$ pair that corresponded to the tryptophan toggle switch: the bitopic ligand dramatically increased RRCS with respect to APO and muscarine forms.

A comparison of data presented in Figure S7a,b and Figure 11a,b may reveal possible differences in structural effects exerted by our bitopic ligand on human and insect receptors, respectively. Similar to human M1 GPRC, the bitopic ligand does not strikingly strengthen the mAChR-A contacts in the signaling pathway pairs (Figure 11a).

However, bitopic ligand decreases the contacts of some critical pairs in the insect receptor structure stronger than IR3535 or even stronger than muscarine (Figure 11b). Particularly interesting were the contacts involving the tyrosine toggle switch $Tyr^{7.53}$ (NPxxY motif): $Val^{1.53} \times Tyr^{7.53}$ and $Leu^{2.43} \times Tyr^{7.53}$. We recall that substantial dynamical changes of the NPxxY motif are typically observed when the GPCR is bound to its full agonist [64]. $Tyr^{7.53}$ was found to switch between three rotameric conformations affecting water flow through the receptor. Upon GPCR activation, a hydrophobic layer breaks as a continuous water channel is formed from the ligand-binding pocket to the cytoplasm [64]. This postulate is in accordance with our analysis of the water tunnel formation (Figure 10) in mAChR-A with BQCA-azo-IR3535.

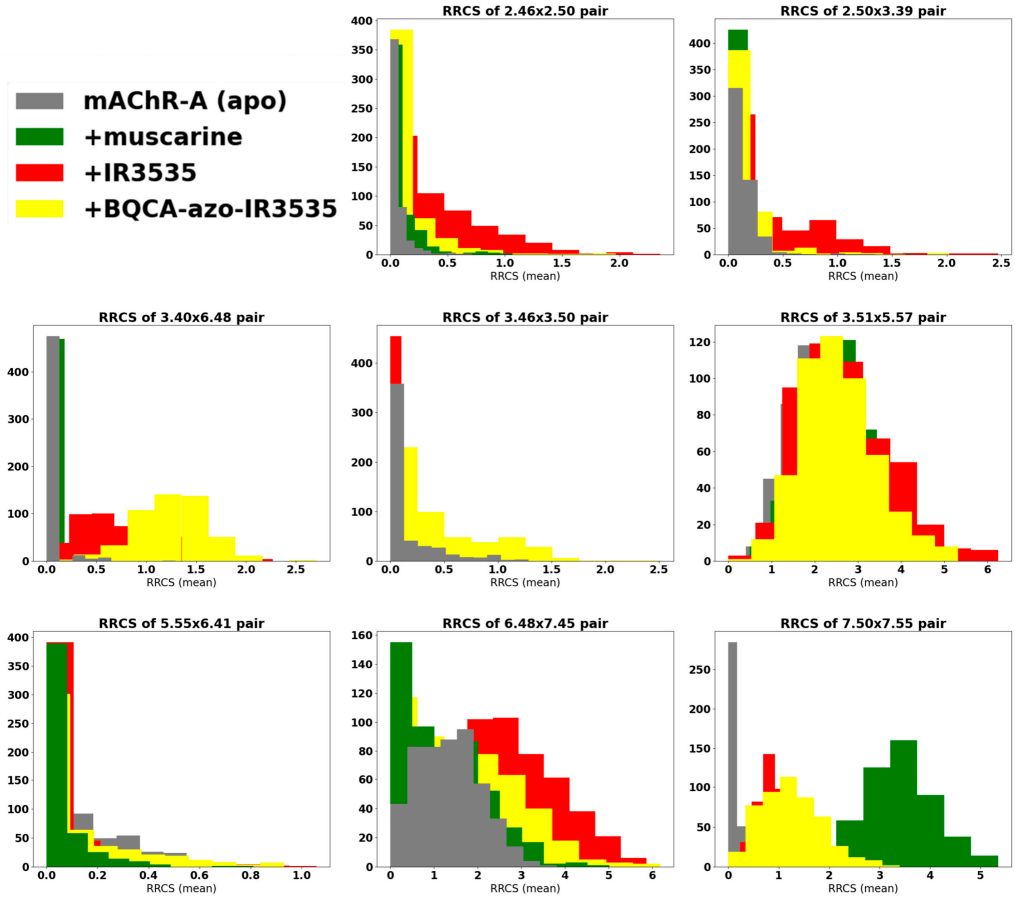

(**a**)

Figure 11. *Cont.*

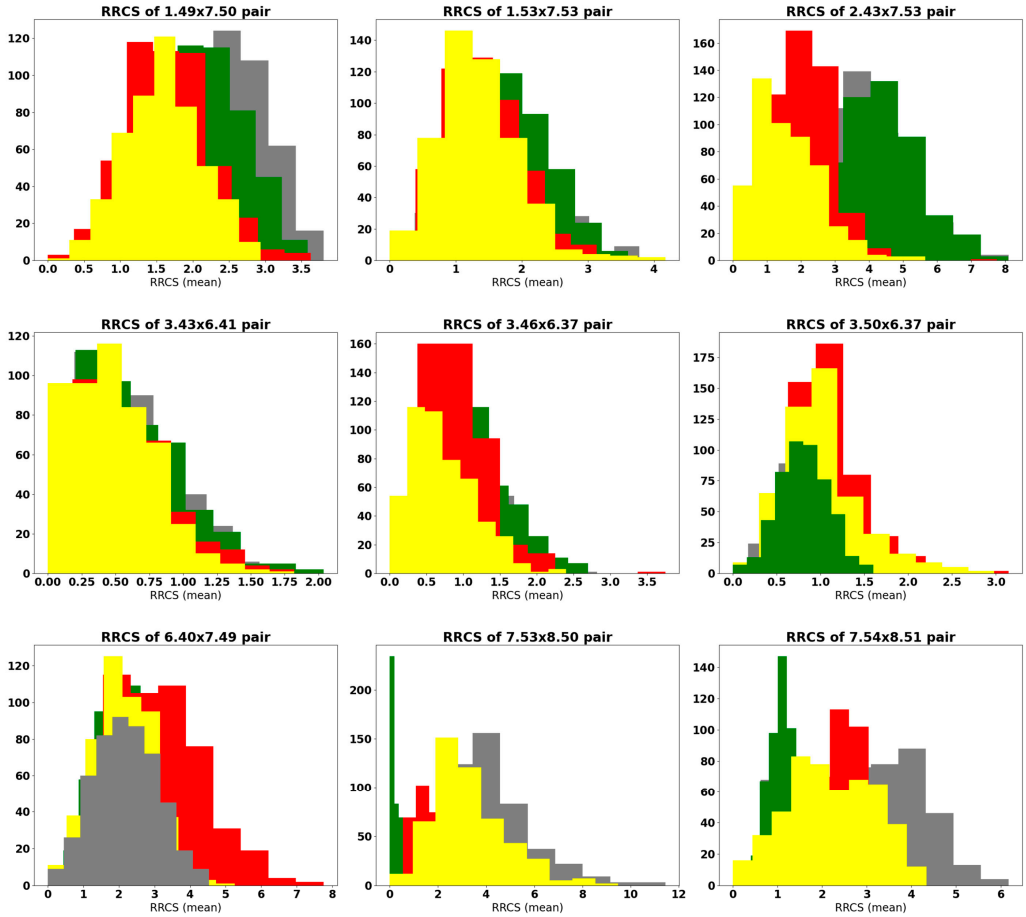

(**b**)

Figure 11. (**a**,**b**) Histograms of residue–residue contact scores (RRCSs) calculated for 1 frame/1 ns of 500 ns MD simulation (average of 3 trajectories) of insect mAChR-A Apo receptor (in grey). Contacts that increase (**a**) and decrease (**b**) RRCS upon activation by a ligand are shown for muscarine in green, IR3535 in red, and for BQCA-azo-IR3535 in yellow.

Quite interesting to note is the behavior of the Gly$^{1.49}$ × Pro$^{7.50}$ pair: in human M1, the large BQCA-azo-IR3535 ligand makes this contact stronger, while in insect mAChR-A those residues are pushed away, and contacts are weaker.

In our detailed, molecular-level analysis, we indicated sensitive spots in the muscarinic GPCRs activation pathway. The characterization of early-stage conformational changes in both human and insect receptors in response to repellent ligand-binding provides ground for the development of new chemicals that would be selective towards insects. Our in silico analysis of a novel, bitopic, and photoswitchable ligand BQCA-azo-IR3535 interactions with mAChRs calls for further experimental studies.

3. Conclusions

MD simulations, despite all known limitations related to simplified models when experimental structures are scarce and limited sampling, are widely used in studies of membrane proteins, including the conformational changes of GPCRs induced by ligands [65,66]. Even though the timescale of GPCR activation by agonists is too long for classical MD, the dynamics of microswitches revealed that relatively short simulations could indicate important allosteric coupling [67].

In this work, for the first time, we provided molecular insights into the early-stage responses of human and insect muscarinic receptors on activation by the safe repellent IR3535 and its bitopic, photoswitchable derivative BQCA-azo-IR3535. The concept of this

ligand was based on the positive allosteric modulation of IR3535 by BQCA we observed in the human M1 receptor. IR3535 was linked to the positive allosteric modulator BQCA part that binds receptor mAChR in the less conserved AS. The ligand proposed here is a molecule that may, hopefully, combine repellent activity with selectivity.

Based on the docking of ligands to the human M1 X-Ray structure and our homology model of the *Drosophila melanogaster* mAChR-A GPCRs and MD simulations, we analyzed the dynamical responses of receptors to the repellents. The recently proposed signal transduction pathway for class A GPCR [43] enumerated 34 pairs critical for receptor activity. After careful analysis of the differences in the close contacts of the RRCS parameters calculated from the 3 × 500 ns MD data sets, we identified pathway pairs that were affected substantially by ligand-binding. The most profound structural effects were localized in the following regions: (a) the tryptophan toggle switch $Trp^{6.48}$ with $Val^{3.40}$, and (b) the residues located at H7 $Pro^{7.50}$ and $Lys^{7.55}$. Substantial loss of contacts was noted in (c) $Lys^{2.43}$ with the tyrosine toggle switch $Tyr^{7.53}$ and (d) in interactions of $Ile^{3.46}$ with the microswitch $Lys^{6.37}$. The MD simulations analysis suggests that the large, bitopic ligand BQCA-azo-IR3535 was bound more tightly to the insect mAChR-A than to the human M1 and, therefore, may increase the rate at which the insect GPCR transition to the active conformational state more profoundly. Thus, based on the presented limited modeling, we believe that the strategy of using simultaneous modulators of both orthosteric and allosteric sites in pest control studies is promising. Such investigations, especially aimed at GPCRs [68], could bring new compounds with reduced toxicity to humans.

4. Materials and Methods

4.1. Molecular Docking

3D structures of the ligands were downloaded from PubChem [69] and docked to the inactive structure of the whole M1 receptor protein (PDB code: 5CXV) using SMINA package [46], a fork of Autodock Vina [47] that provides enhanced support for minimization and scoring. For each ligand, 10 independent docking runs were carried out using default settings, generating up to 100 poses per run. The best-scored poses of the ligands occupying the pockets found using the FTSite [48] and POCASA1.1 [70] were selected and further prepared using Schrödinger Maestro [71] by adding hydrogen and were minimized to obtain optimal conformation.

4.2. Molecular Dynamics (MD)

Topology and parameters files for the ligands were generated by SwissParam [72]. The proper orientation of the receptor in a membrane was found using the PPM OPM server [73]. Each human receptor with a ligand system was placed in a homogenous lipid bilayer environment consisting of approximately 200 (190–207) dioleoylphosphatidylcholine (DOPC) molecules. About 21,000 (20,968) molecules of water were added above and below the lipids to generate a 20 Å thickness layer. The system was neutralized with counterions to the concentration of 0.15 M. Temperature was controlled by the Langevin thermostat with a value of 303.15 K and the target pressure was set to 1.01325 bar (1 atm). We applied the CHARMM36 force field with the TIP3P model for water. Equilibration followed by 150 ns MD simulations of whole systems (receptor + ligand + membrane + ions + water) was performed using NAMD [74] based on the input files generated with the CHARMM-GUI Membrane Builder [75]. Three independent simulations were performed for each system generating a total of 8550 ns trajectory data.

4.3. Homology Modeling

The homology model of the fruit fly (*Drosophila melanogaster*) mAChR-A receptor was built using the SWISS-MODEL [76] based on a UniProtKB P16395 (ACM1_DROME) sequence. As a whole sequence model could not be built properly, the residues 300–700 (part of the intracellular loop 3) were removed to obtain the seven transmembrane helices

model. The inactive state of the human M1 receptor (PDB code: 5CXV) was used as a template due to the highest similarity and the best scoring.

The quality of the mAChR-A model was validated by PROCHECK [77], ERRAT [78], Verify3D [79] and PROVE [80], all of which belong to the structure analysis-validation online server sponsored by the UCLA-DOE Institute for Genomics and Proteomics. The overall quality factor of ERRAT, expressed as the percentage of the protein for which the calculated error value falls below the 95% rejection limit, equals 98.94. Only three residues exceeded the error value (see SM Figure S9). VERIFY3D validation was passed with 99.66% of the residues having averaged 3D-1D score $\geq$ 0.2. PROVE validation was passed with no buried outlier protein atoms found. The Ramachandran plot and the all-residue Chi1-Chi2 plots generated by PROCHECK [77] can be found in the SM Figures S10 and S11, respectively.

Molecular docking and dynamics were performed as described above with changed plasma lipid composition. Approximately 200 lipid molecules were used in the following proportions: 38% DOPE, 18% DOPS, 16% DOPC, 13% POPI, 11% SM (CER180), 3% DOPG and 1% PALO 16:1 fatty acid. For the insect model, three repetitions of 500 ns MD simulation each were collected.

4.4. Analysis

The analysis and visualization were made using the VMD code [81], Python package [82], and homemade scripts. Snake plots of human M1 and insect mAChR-A were made using the Protter server [29].

A residue–residue contact score (RRCS), an atomic distance-based calculation that quantifies the strength of contact between residue pairs, was calculated with the python script provided by Zhou et al. [43] and further analyzed with the NumPy package.

The percentage of MD frames in which any pairs of M1 residues possibly interacted were calculated using the GetContacts server [52]. MOLEonline [62] and CAVER [63] were used to investigate the water tunnels in protein. For CAVER analysis, trajectories were aligned and processed into a series of PDB snapshots (one frame every 5 ns of MD). The parameters used included the probe radius of 0.9 Å to identify internal tunnels. $W^{6.48}$ was used as a starting point residue for calculations.

Supplementary Materials: The following are available online at https://www.mdpi.com/article/10.3390/molecules27103280/s1, Figure S1. Molecular docking of DEET and IR3535 to the human M1 GPCR (PDB code: 5CV) together with the SMINA scoring function (SSF) affinity decomposition. Figures S2–S5. Molecular docking of ligands (DEET, IR3535, muscarine, atropine, BQCA, Oxotremorine-M, pirenzepine, BQZ-12) to the human M1 GPCR (PDB code: 5CV). SMINA scoring function (SSF) shows the minimized affinity of the ligand to the receptor. Figure S6. Histogram plots for residue–residue contact scores (RRCSs) of human M1 receptor in APO form and bound with DEET, IR3535, or muscarine. Figure S7a,b. Histogram plots for residue–residue contact scores (RRCSs) of human M1 receptor in APO form and with IR3535, IR3535 together with BQCA and with bitopic BQCA-azo-IR3535 ligand bound. Figure S8. BQCA-azo-IR3535 interaction with human M1 receptor and insect mAChR-A model. Figures S9–S11. Homology model assessment. Table S1. SSF values of repellents docking to the active structures.

Author Contributions: Conceptualization, W.N., B.N. and B.L.; methodology, W.N.; software, B.N.; validation, W.N., B.N. and B.L.; formal analysis, W.N. and B.L.; investigation, B.N.; resources, W.N.; data curation, B.N. and W.N.; writing—original draft preparation, B.N.; writing—review and editing, B.N., B.L., W.N.; visualization, B.N.; supervision, W.N. and B.L.; project administration, W.N., B.L.; funding acquisition, W.N. All authors have read and agreed to the published version of the manuscript.

Funding: The authors (B.N. and W.N.) acknowledge funding from the National Science Centre, Poland (Grant 2016/23/B/ST4/01770). Support from the project POWR.03.05.00-00-Z302/17 Universitas Copernicana Thoruniensis in Futuro-IDS "Academia Copernicana" is also acknowledged (B.N.).

Institutional Review Board Statement: Not applicable.

Informed Consent Statement: Not applicable.

Data Availability Statement: Ligand docked structures and the structure of Dm type A mAChR are available from B.N. or W.N. upon request.

Acknowledgments: Calculations were performed in the Centre of Informatics—Tricity Academic Supercomputer & Network (CI TASK), and in the Interdisciplinary Centre for Mathematical and Computational Modeling (ICM), University of Warsaw, under grant no. GA76-16. We thank Katarzyna Walczewska-Szewc for her help in preparing the data analysis PYTHON script. B.N. and W.N. are members of #MEMOBIT priority team supported by IDUB NCU.

Conflicts of Interest: The authors declare no conflict of interest.

Sample Availability: Samples of the compounds are not available from the authors.

References

1. Campbell-Lendrum, D.; Manga, L.; Bagayoko, M.; Sommerfeld, J. Climate change and vector-borne diseases: What are the implications for public health research and policy? *Philos. Trans. R. Soc. Lond. B Biol. Sci.* **2015**, *370*, 20130552. [CrossRef]
2. Benelli, G.; Wilke, A.B.; Bloomquist, J.R.; Desneux, N.; Beier, J.C. Overexposing mosquitoes to insecticides under global warming: A public health concern? *Sci. Total Environ.* **2021**, *762*, 143069. [CrossRef]
3. Hemingway, J. Resistance: A problem without an easy solution. *Pestic. Biochem. Physiol.* **2018**, *151*, 73–75. [CrossRef] [PubMed]
4. Liu, N. Insecticide Resistance in Mosquitoes: Impact, Mechanisms, and Research Directions. *Annu. Rev. Entomol.* **2015**, *60*, 537–559. [CrossRef] [PubMed]
5. Miller, J.; Siegert, P.; Amimo, F.; Walker, E. Designation of chemicals in terms of the locomotor responses they elicit from insects: An update of Dethier et al.(1960). *J. Econ. Entomol.* **2009**, *102*, 2056–2060. [CrossRef] [PubMed]
6. Tavares, M.; da Silva, M.R.M.; de Siqueira, L.B.d.O.; Rodrigues, R.A.S.; Bodjolle-d'Almeida, L.; Dos Santos, E.P.; Ricci-Júnior, E. Trends in insect repellent formulations: A review. *Int. J. Pharm.* **2018**, *539*, 190–209. [CrossRef]
7. Lupi, E.; Hatz, C.; Schlagenhauf, P. The efficacy of repellents against *Aedes*, *Anopheles*, *Culex* and *Ixodes* spp.—A literature review. *Travel Med. Infect. Dis.* **2013**, *11*, 374–411. [CrossRef]
8. Corbel, V.; Stankiewicz, M.; Pennetier, C.; Fournier, D.; Stojan, J.; Girard, E.; Dimitrov, M.; Molgo, J.; Hougard, J.M.; Lapied, B. Evidence for inhibition of cholinesterases in insect and mammalian nervous systems by the insect repellent deet. *BMC Biol.* **2009**, *7*, 47. [CrossRef]
9. Swale, D.R.; Sun, B.; Tong, F.; Bloomquist, J.R. Neurotoxicity and mode of action of N, N-diethyl-meta-toluamide (DEET). *PLoS ONE* **2014**, *9*, e103713. [CrossRef]
10. Legeay, S.; Clere, N.; Hilairet, G.; Do, Q.T.; Bernard, P.; Quignard, J.F.; Apaire-Marchais, V.; Lapied, B.; Faure, S. The insect repellent N,N-diethyl-m-toluamide (DEET) induces angiogenesis via allosteric modulation of the M3 muscarinic receptor in endothelial cells. *Sci. Rep.* **2016**, *6*, 28546. [CrossRef]
11. Osimitz, T.; Murphy, J.; Fell, L.; Page, B. Adverse events associated with the use of insect repellents containing N, N-diethyl-m-toluamide (DEET). *Regul. Toxicol. Pharmacol.* **2010**, *56*, 93–99. [CrossRef] [PubMed]
12. Legeay, S.; Clere, N.; Apaire-Marchais, V.; Faure, S.; Lapied, B. Unusual modes of action of the repellent DEET in insects highlight some human side effects. *Eur. J. Pharmacol.* **2018**, *825*, 92–98. [CrossRef] [PubMed]
13. Bohbot, J.D.; Dickens, J.C. Odorant receptor modulation: Ternary paradigm for mode of action of insect repellents. *Neuropharmacology* **2012**, *62*, 2086–2095. [CrossRef] [PubMed]
14. Sanford, J.L.; Barski, S.A.; Seen, C.M.; Dickens, J.C.; Shields, V.D. Neurophysiological and behavioral responses of gypsy moth larvae to insect repellents: DEET, IR3535, and Picaridin. *PLoS ONE* **2014**, *9*, e99924. [CrossRef] [PubMed]
15. DeGennaro, M. The mysterious multi-modal repellency of DEET. *Fly* **2015**, *9*, 45–51. [CrossRef]
16. Sparks, J.T.; Dickens, J.C. Bitter-sensitive gustatory receptor neuron responds to chemically diverse insect repellents in the common malaria mosquito *Anopheles quadrimaculatus*. *Sci. Nat.* **2016**, *103*, 39. [CrossRef]
17. Sparks, J.T.; Dickens, J.C. Mini review: Gustatory reception of chemicals affecting host feeding in aedine mosquitoes. *Pestic. Biochem. Physiol.* **2017**, *142*, 15–20. [CrossRef]
18. Deshayes, C.; Moreau, E.; Pitti-Caballero, J.; Froger, J.-A.; Apaire-Marchais, V.; Lapied, B. Synergistic agent and intracellular calcium, a successful partnership in the optimization of insecticide efficacy. *Curr. Opin. Insect Sci.* **2018**, *30*, 52–58. [CrossRef]
19. Abd-Ella, A.; Stankiewicz, M.; Mikulska, K.; Nowak, W.; Pennetier, C.; Goulu, M.; Fruchart-Gaillard, C.; Licznar, P.; Apaire-Marchais, V.; List, O.; et al. The Repellent DEET Potentiates Carbamate Effects via Insect Muscarinic Receptor Interactions: An Alternative Strategy to Control Insect Vector-Borne Diseases. *PLoS ONE* **2015**, *10*, e0126406. [CrossRef]
20. Moreau, E.; Mikulska-Ruminska, K.; Goulu, M.; Perrier, S.; Deshayes, C.; Stankiewicz, M.; Apaire-Marchais, V.; Nowak, W.; Lapied, B. Orthosteric muscarinic receptor activation by the insect repellent IR3535 opens new prospects in insecticide-based vector control. *Sci. Rep.* **2020**, *10*, 6842. [CrossRef]
21. Jankowska, M.; Lapied, B.; Jankowski, W.; Stankiewicz, M. The unusual action of essential oil component, menthol, in potentiating the effect of the carbamate insecticide, bendiocarb. *Pestic. Biochem. Physiol.* **2019**, *158*, 101–111. [CrossRef] [PubMed]
22. Ihara, M.; Buckingham, S.D.; Matsuda, K.; Sattelle, D.B. Modes of action, resistance and toxicity of insecticides targeting nicotinic acetylcholine receptors. *Curr. Med. Chem.* **2017**, *24*, 2925–2934. [CrossRef] [PubMed]

23. Casida, J.E. Neonicotinoids and other insect nicotinic receptor competitive modulators: Progress and prospects. *Annu. Rev. Entomol.* **2018**, *63*, 125–144. [CrossRef] [PubMed]
24. Matsuda, K.; Ihara, M.; Sattelle, D.B. Neonicotinoid insecticides: Molecular targets, resistance, and toxicity. *Annu. Rev. Pharmacol. Toxicol.* **2020**, *60*, 241–255. [CrossRef] [PubMed]
25. Collin, C.; Hauser, F.; de Valdivia, E.G.; Li, S.; Reisenberger, J.; Carlsen, E.M.; Khan, Z.; Hansen, N.Ø.; Puhm, F.; Søndergaard, L. Two types of muscarinic acetylcholine receptors in *Drosophila* and other arthropods. *Cell. Mol. Life Sci.* **2013**, *70*, 3231–3242. [CrossRef]
26. Xia, R.Y.; Li, M.Q.; Wu, Y.S.; Qi, Y.X.; Ye, G.Y.; Huang, J. A new family of insect muscarinic acetylcholine receptors. *Insect Mol. Biol.* **2016**, *25*, 362–369. [CrossRef]
27. Pilon, A.; Goven, D.; Raymond, V. Pharmacological and molecular characterization of the A-type muscarinic acetylcholine receptor from *Anopheles gambiae*. *Insect Mol. Biol.* **2022**. [CrossRef] [PubMed]
28. Ren, G.R.; Folke, J.; Hauser, F.; Li, S.; Grimmelikhuijzen, C.J. The A-and B-type muscarinic acetylcholine receptors from *Drosophila melanogaster* couple to different second messenger pathways. *Biochem. Biophys. Res. Commun.* **2015**, *462*, 358–364. [CrossRef]
29. Omasits, U.; Ahrens, C.H.; Müller, S.; Wollscheid, B. Protter: Interactive protein feature visualization and integration with experimental proteomic data. *Bioinformatics* **2014**, *30*, 884–886. [CrossRef]
30. Ghosh, E.; Kumari, P.; Jaiman, D.; Shukla, A.K. Methodological advances: The unsung heroes of the GPCR structural revolution. *Nat. Rev. Mol. Cell Biol.* **2015**, *16*, 69–81. [CrossRef]
31. Congreve, M.; de Graaf, C.; Swain, N.A.; Tate, C.G. Impact of GPCR structures on drug discovery. *Cell* **2020**, *181*, 81–91. [CrossRef] [PubMed]
32. Christopoulos, A. Advances in G protein-coupled receptor allostery: From function to structure. *Mol. Pharmacol.* **2014**, *86*, 463–478. [CrossRef] [PubMed]
33. Thal, D.M.; Glukhova, A.; Sexton, P.M.; Christopoulos, A. Structural insights into G-protein-coupled receptor allostery. *Nature* **2018**, *559*, 45–53. [CrossRef]
34. Valant, C.; Gregory, K.J.; Hall, N.E.; Scammells, P.J.; Lew, M.J.; Sexton, P.M.; Christopoulos, A. A Novel Mechanism of G Protein-coupled Receptor Functional Selectivity: MUSCARINIC PARTIAL AGONIST McN-A-343 AS A BITOPIC ORTHOSTERIC/ALLOSTERIC LIGAND∗. *J. Biol. Chem.* **2008**, *283*, 29312–29321. [CrossRef]
35. Davie, B.J.; Christopoulos, A.; Scammells, P.J. Development of M1 mAChR allosteric and bitopic ligands: Prospective therapeutics for the treatment of cognitive deficits. *ACS Chem. Neurosci.* **2013**, *4*, 1026–1048. [CrossRef] [PubMed]
36. Keov, P.; López, L.; Devine, S.M.; Valant, C.; Lane, J.R.; Scammells, P.J.; Sexton, P.M.; Christopoulos, A. Molecular mechanisms of bitopic ligand engagement with the M1 muscarinic acetylcholine receptor. *J. Biol. Chem.* **2014**, *289*, 23817–23837. [CrossRef] [PubMed]
37. Antony, J.; Kellershohn, K.; Mohr-Andrä, M.; Kebig, A.; Prilla, S.; Muth, M.; Heller, E.; Disingrini, T.; Dallanoce, C.; Bertoni, S. Dualsteric GPCR targeting: A novel route to binding and signaling pathway selectivity. *FASEB J.* **2009**, *23*, 442–450. [CrossRef]
38. Mohr, K.; Tränkle, C.; Kostenis, E.; Barocelli, E.; De Amici, M.; Holzgrabe, U. Rational design of dualsteric GPCR ligands: Quests and promise. *Br. J. Pharmacol.* **2010**, *159*, 997–1008. [CrossRef]
39. Agnetta, L.; Kauk, M.; Canizal, M.C.A.; Messerer, R.; Holzgrabe, U.; Hoffmann, C.; Decker, M. A photoswitchable dualsteric ligand controlling receptor efficacy. *Angew. Chem. Int. Ed.* **2017**, *56*, 7282–7287. [CrossRef]
40. Hoorens, M.W.; Szymanski, W. Reversible, spatial and temporal control over protein activity using light. *Trends Biochem. Sci.* **2018**, *43*, 567–575. [CrossRef]
41. Ricart-Ortega, M.; Font, J.; Llebaria, A. GPCR photopharmacology. *Mol. Cell. Endocrinol.* **2019**, *488*, 36–51. [CrossRef]
42. Nargeot, J.; Lester, H.A.; Birdsall, N.; Stockton, J.; Wassermann, N.H.; Erlanger, B.F. A photoisomerizable muscarinic antagonist. Studies of binding and of conductance relaxations in frog heart. *J. Gen. Physiol.* **1982**, *79*, 657–678. [CrossRef]
43. Zhou, Q.; Yang, D.; Wu, M.; Guo, Y.; Guo, W.; Zhong, L.; Cai, X.; Dai, A.; Jang, W.; Shakhnovich, E.I.; et al. Common activation mechanism of class A GPCRs. *eLife* **2019**, *8*, e50279. [CrossRef]
44. Filipek, S. Molecular switches in GPCRs. *Curr. Opin. Struct. Biol.* **2019**, *55*, 114–120. [CrossRef]
45. Katritch, V.; Fenalti, G.; Abola, E.E.; Roth, B.L.; Cherezov, V.; Stevens, R.C. Allosteric sodium in class A GPCR signaling. *Trends Biochem. Sci.* **2014**, *39*, 233–244. [CrossRef]
46. Koes, D.R.; Baumgartner, M.P.; Camacho, C.J. Lessons learned in empirical scoring with smina from the CSAR 2011 benchmarking exercise. *J. Chem. Inf. Modeling* **2013**, *53*, 1893–1904. [CrossRef]
47. Trott, O.; Olson, A.J. AutoDock Vina: Improving the speed and accuracy of docking with a new scoring function, efficient optimization, and multithreading. *J. Comput. Chem.* **2010**, *31*, 455–461. [CrossRef]
48. Ngan, C.-H.; Hall, D.R.; Zerbe, B.; Grove, L.E.; Kozakov, D.; Vajda, S. FTSite: High accuracy detection of ligand binding sites on unbound protein structures. *Bioinformatics* **2012**, *28*, 286–287. [CrossRef]
49. Salentin, S.; Schreiber, S.; Haupt, V.J.; Adasme, M.F.; Schroeder, M. PLIP: Fully automated protein–ligand interaction profiler. *Nucleic Acids Res.* **2015**, *43*, W443–W447. [CrossRef]
50. Hulme, E.; Lu, Z.; Bee, M. Scanning mutagenesis studies of the M 1 muscarinic acetylcholine receptor. *Recept. Channels* **2003**, *9*, 215–228. [CrossRef]

51. Ballesteros, J.A.; Weinstein, H. [19] Integrated methods for the construction of three-dimensional models and computational probing of structure-function relations in G protein-coupled receptors. In *Methods in Neurosciences*; Academic Press: New York, NY, USA, 1995; Volume 25, pp. 366–428. [CrossRef]
52. Venkatakrishnan, A.; Fonseca, R.; Ma, A.K.; Hollingsworth, S.A.; Chemparathy, A.; Hilger, D.; Kooistra, A.J.; Ahmari, R.; Babu, M.M.; Kobilka, B.K. Uncovering patterns of atomic interactions in static and dynamic structures of proteins. *bioRxiv* **2019**, 840694. [CrossRef]
53. Riefolo, F.; Matera, C.; Garrido-Charles, A.; Gomila, A.M.; Sortino, R.; Agnetta, L.; Claro, E.; Masgrau, R.; Holzgrabe, U.; Batlle, M. Optical control of cardiac function with a photoswitchable muscarinic agonist. *J. Am. Chem. Soc.* **2019**, *141*, 7628–7636. [CrossRef] [PubMed]
54. Yuan, X.; Raniolo, S.; Limongelli, V.; Xu, Y. The molecular mechanism underlying ligand binding to the membrane-embedded site of a G-protein-coupled receptor. *J. Chem. Theory Comput.* **2018**, *14*, 2761–2770. [CrossRef] [PubMed]
55. Dawaliby, R.; Trubbia, C.; Delporte, C.; Noyon, C.; Ruysschaert, J.-M.; Van Antwerpen, P.; Govaerts, C. Phosphatidylethanolamine is a key regulator of membrane fluidity in eukaryotic cells. *J. Biol. Chem.* **2016**, *291*, 3658–3667. [CrossRef] [PubMed]
56. Wu, E.L.; Cheng, X.; Jo, S.; Rui, H.; Song, K.C.; Dávila-Contreras, E.M.; Qi, Y.; Lee, J.; Monje-Galvan, V.; Venable, R.M. CHARMM-GUI *Membrane Builder* toward realistic biological membrane simulations. *J. Comput. Chem.* **2014**, *35*, 1997–2004. [CrossRef]
57. Ragoza, M.; Hochuli, J.; Idrobo, E.; Sunseri, J.; Koes, D.R. Protein–ligand scoring with convolutional neural networks. *J. Chem. Inf. Modeling* **2017**, *57*, 942–957. [CrossRef]
58. Chan, H.S.; Wang, J.; Palczewski, K.; Filipek, S.; Vogel, H.; Liu, Z.-J.; Yuan, S. Exploring a new ligand binding site of G protein-coupled receptors. *Chem. Sci.* **2018**, *9*, 6480–6489. [CrossRef]
59. Chan, H.S.; Xu, Y.; Tan, L.; Vogel, H.; Cheng, J.; Wu, D.; Yuan, S. Enhancing the signaling of GPCRs via orthosteric ions. *ACS Cent. Sci.* **2020**, *6*, 274–282. [CrossRef]
60. Draper-Joyce, C.J.; Verma, R.K.; Michino, M.; Shonberg, J.; Kopinathan, A.; Herenbrink, C.K.; Scammells, P.J.; Capuano, B.; Abramyan, A.M.; Thal, D.M. The action of a negative allosteric modulator at the dopamine D 2 receptor is dependent upon sodium ions. *Sci. Rep.* **2018**, *8*, 1208. [CrossRef]
61. Livingston, K.E.; Traynor, J.R. Disruption of the Na+ ion binding site as a mechanism for positive allosteric modulation of the mu-opioid receptor. *Proc. Natl. Acad. Sci. USA* **2014**, *111*, 18369–18374. [CrossRef]
62. Pravda, L.; Sehnal, D.; Toušek, D.; Navrátilová, V.; Bazgier, V.; Berka, K.; Svobodová Vařeková, R.; Koča, J.; Otyepka, M. MOLEonline: A web-based tool for analyzing channels, tunnels and pores (2018 update). *Nucleic Acids Res.* **2018**, *46*, W368–W373. [CrossRef] [PubMed]
63. Chovancova, E.; Pavelka, A.; Benes, P.; Strnad, O.; Brezovsky, J.; Kozlikova, B.; Gora, A.; Sustr, V.; Klvana, M.; Medek, P. CAVER 3.0: A tool for the analysis of transport pathways in dynamic protein structures. *PLoS Comput. Biol.* **2012**, *8*, e1002708. [CrossRef] [PubMed]
64. Frei, J.N.; Broadhurst, R.W.; Bostock, M.J.; Solt, A.; Jones, A.J.; Gabriel, F.; Tandale, A.; Shrestha, B.; Nietlispach, D. Conformational plasticity of ligand-bound and ternary GPCR complexes studied by 19 F NMR of the β 1-adrenergic receptor. *Nat. Commun.* **2020**, *11*, 669. [CrossRef] [PubMed]
65. Hollingsworth, S.A.; Dror, R.O. Molecular dynamics simulation for all. *Neuron* **2018**, *99*, 1129–1143. [CrossRef]
66. Latorraca, N.R.; Venkatakrishnan, A.; Dror, R.O. GPCR dynamics: Structures in motion. *Chem. Rev.* **2017**, *117*, 139–155. [CrossRef]
67. Fleetwood, O.; Carlsson, J.; Delemotte, L. Identification of ligand-specific G protein-coupled receptor states and prediction of downstream efficacy via data-driven modeling. *eLife* **2021**, *10*, e60715. [CrossRef]
68. Birgül Iyison, N.; Shahraki, A.; Kahveci, K.; Düzgün, M.B.; Gün, G. Are insect GPCRs ideal next-generation pesticides: Opportunities and challenges. *FEBS J.* **2021**, *288*, 2727–2745. [CrossRef] [PubMed]
69. Kim, S.; Chen, J.; Cheng, T.; Gindulyte, A.; He, J.; He, S.; Li, Q.; Shoemaker, B.A.; Thiessen, P.A.; Yu, B. PubChem 2019 update: Improved access to chemical data. *Nucleic Acids Res.* **2019**, *47*, D1102–D1109. [CrossRef]
70. Yu, J.; Zhou, Y.; Tanaka, I.; Yao, M. Roll: A new algorithm for the detection of protein pockets and cavities with a rolling probe sphere. *Bioinformatics* **2010**, *26*, 46–52. [CrossRef]
71. Madhavi Sastry, G.; Adzhigirey, M.; Day, T.; Annabhimoju, R.; Sherman, W. Protein and ligand preparation: Parameters, protocols, and influence on virtual screening enrichments. *J. Comput.-Aided Mol. Des.* **2013**, *27*, 221–234. [CrossRef]
72. Zoete, V.; Cuendet, M.A.; Grosdidier, A.; Michielin, O. SwissParam: A fast force field generation tool for small organic molecules. *J. Comput. Chem.* **2011**, *32*, 2359–2368. [CrossRef] [PubMed]
73. Lomize, M.A.; Pogozheva, I.D.; Joo, H.; Mosberg, H.I.; Lomize, A.L. OPM database and PPM web server: Resources for positioning of proteins in membranes. *Nucleic Acids Res.* **2012**, *40*, D370–D376. [CrossRef] [PubMed]
74. Phillips, J.C.; Braun, R.; Wang, W.; Gumbart, J.; Tajkhorshid, E.; Villa, E.; Chipot, C.; Skeel, R.D.; Kale, L.; Schulten, K. Scalable molecular dynamics with NAMD. *J. Comput. Chem.* **2005**, *26*, 1781–1802. [CrossRef] [PubMed]
75. Lee, J.; Cheng, X.; Swails, J.M.; Yeom, M.S.; Eastman, P.K.; Lemkul, J.A.; Wei, S.; Buckner, J.; Jeong, J.C.; Qi, Y. CHARMM-GUI input generator for NAMD, GROMACS, AMBER, OpenMM, and CHARMM/OpenMM simulations using the CHARMM36 additive force field. *J. Chem. Theory Comput.* **2016**, *12*, 405–413. [CrossRef] [PubMed]
76. Waterhouse, A.; Bertoni, M.; Bienert, S.; Studer, G.; Tauriello, G.; Gumienny, R.; Heer, F.T.; de Beer, T.A.P.; Rempfer, C.; Bordoli, L. SWISS-MODEL: Homology modelling of protein structures and complexes. *Nucleic Acids Res.* **2018**, *46*, W296–W303. [CrossRef]

77. Laskowski, R.A.; MacArthur, M.W.; Moss, D.S.; Thornton, J.M. PROCHECK: A program to check the stereochemical quality of protein structures. *J. Appl. Crystallogr.* **1993**, *26*, 283–291. [CrossRef]
78. Colovos, C.; Yeates, T.O. Verification of protein structures: Patterns of nonbonded atomic interactions. *Protein Sci.* **1993**, *2*, 1511–1519. [CrossRef]
79. Lüthy, R.; Bowie, J.U.; Eisenberg, D. Assessment of protein models with three-dimensional profiles. *Nature* **1992**, *356*, 83–85. [CrossRef]
80. Pontius, J.; Richelle, J.; Wodak, S.J. Deviations from standard atomic volumes as a quality measure for protein crystal structures. *J. Mol. Biol.* **1996**, *264*, 121–136. [CrossRef]
81. Humphrey, W.; Dalke, A.; Schulten, K. VMD: Visual molecular dynamics. *J. Mol. Graph.* **1996**, *14*, 33–38. [CrossRef]
82. Van Rossum, G.; Drake, F.L. Python reference manual. In *Department of Computer Science [CS]*; CWI: Amsterdam, The Netherlands, 1995; p. R9525.

9. Article II

Interactions of Sea Anemone Toxins with Insect Sodium Channel —Insights from Electrophysiology and Molecular Docking Studies

molecules

MDPI

Article

Interactions of Sea Anemone Toxins with Insect Sodium Channel—Insights from Electrophysiology and Molecular Docking Studies

Beata Niklas [1,*], Milena Jankowska [2], Dalia Gordon [3], László Béress [4], Maria Stankiewicz [2] and Wieslaw Nowak [1,*]

1 Institute of Physics, Faculty of Physics, Astronomy and Informatics, Nicolaus Copernicus University, Grudziadzka 5, 87-100 Torun, Poland
2 Faculty of Biological and Veterinary Sciences, Nicolaus Copernicus University, Lwowska 1, 87-100 Torun, Poland; mjank@umk.pl (M.J.); stankiew@umk.pl (M.S.)
3 Department of Biomolecular Sciences, Weizmann Institute of Science, Rehovot 76100, Israel; dalia.gordon@gmail.com
4 Department of Internal Medicine, Clinic of Immunology, Division of Experimental and Clinical Peptide Research, Hannover Medical School, 30625 Hannover, Germany; dr.beress@t-online.de
* Correspondence: beata.niklas@doktorant.umk.pl (B.N.); wiesiek@umk.pl (W.N.)

Abstract: Animal venoms are considered as a promising source of new drugs. Sea anemones release polypeptides that affect electrical activity of neurons of their prey. Voltage dependent sodium (Nav) channels are the common targets of Av1, Av2, and Av3 toxins from *Anemonia viridis* and CgNa from *Condylactis gigantea*. The toxins bind to the extracellular side of a channel and slow its fast inactivation, but molecular details of the binding modes are not known. Electrophysiological measurements on *Periplaneta americana* neuronal preparation revealed differences in potency of these toxins to increase nerve activity. Av1 and CgNa exhibit the strongest effects, while Av2 the weakest effect. Extensive molecular docking using a modern SMINA computer method revealed only partial overlap among the sets of toxins' and channel's amino acid residues responsible for the selectivity and binding modes. Docking positions support earlier supposition that the higher neuronal activity observed in electrophysiology should be attributed to hampering the fast inactivation gate by interactions of an anemone toxin with the voltage driven S4 helix from domain IV of cockroach Nav channel (NavPaS). Our modelling provides new data linking activity of toxins with their mode of binding in site 3 of NavPaS channel.

Keywords: anemone toxins; sodium channels; fast inactivation; docking; electrophysiology

Citation: Niklas, B.; Jankowska, M.; Gordon, D.; Béress, L.; Stankiewicz, M.; Nowak, W. Interactions of Sea Anemone Toxins with Insect Sodium Channel—Insights from Electrophysiology and Molecular Docking Studies. *Molecules* **2021**, *26*, 1302. https://doi.org/10.3390/molecules26051302

Academic Editor: Kamil Kuca

Received: 31 January 2021
Accepted: 24 February 2021
Published: 28 February 2021

1. Introduction

Voltage dependent sodium (Nav) channels are cell transmembrane proteins responsible for the depolarizing phase of action potentials which are carriers of information in excitable tissues. Nav channel structure consist of a single polypeptide chain that folds into four domains (DI–DIV) with six transmembrane helices (S1–S6) each. In each domain, helices S1–S4 constitute the so-called voltage-sensing-domain (VSD) with helix S4 acting as a voltage sensor. Helices S5 and S6 contribute to the ion conducting pore. Upon membrane depolarization, the outward movement of positively charged S4 helices generates the gating current which triggers the activation of the sodium channel [1]. A particular function is linked with the upward motion of the S4 segment in DIV since it is coupled to the inactivation gate (IG). When S4 helices are raised outwards, the intracellular IG quickly blocks sodium ions entry into the neuron in a process named fast inactivation (completed within 1–2 ms). Due to this blocking mechanism, neurons exhibit very short action potentials and, therefore, enable a high frequency of signal transmission [2]. It is

accepted that, in vertebrates, the IG gate, located in DIII-DIV linker, consists of Isoleucine-Phenylalanine-Methionine (IFM) motif [3], but consensus identification of IG in insects, as well as molecular details of Nav channel blocking mechanism by the gate, is still elusive.

Many modifications in Nav function result in the disruption of nervous and muscle function and can lead to convulsions, contractive or flaccid paralysis, and even death. In humans, mutations in sodium channels cause several diseases, such as miotonias, myasthenias, epilepsy, and pain and movement disorders [4,5]. Nav channels are quite an old "invention" of evolution [6] and, as such, have become a target for many natural toxins. Years of research on the interaction between sodium channels and natural toxins allowed to classify them into two groups: (1) sodium channel blockers and (2) Nav channel gating modifiers. Toxins bind to seven receptor sites (site 1–site 7) localized in different parts of the Nav protein [7]. Depending on the type of receptor site, toxins induce various modification of the Nav channel function. Toxins that bind to receptor site 3 (site 3 toxins), which is located in the extracellular loop connecting segment S3 and S4 in VSDIV of Nav channel (Figure 1), inhibit the fast inactivation of the sodium channel. Such toxins, usually cysteine-rich peptides [8], were found in the venoms of scorpions [9], spiders [10], sea anemones [11], and venomous sea snails—Conus [12]. Many sea anemone venom neurotoxins immobilize pray and serve as defense against predators. They act by binding to site 3 and inhibiting the fast inactivation phase of Nav channels [13]. Sea anemone toxins are, therefore, of great interest in the research on pain [14] and neuronal conductance modulation.

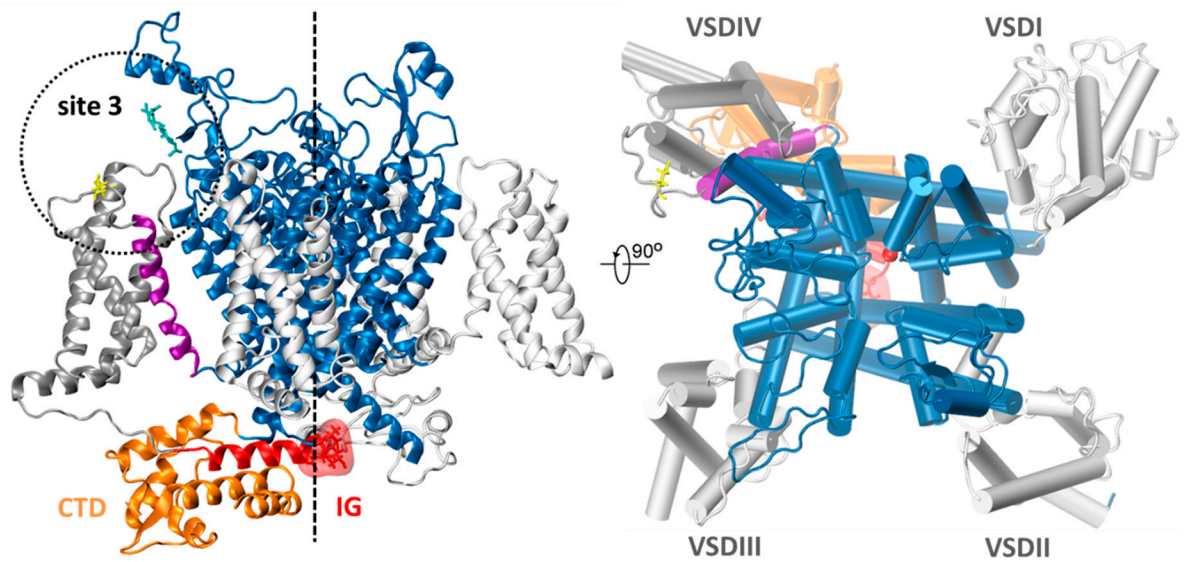

Figure 1. A schematic view of the *Periplaneta americana* voltage dependent sodium channel (NavPaS) based on the Protein Data Bank structure 6A95 [15]. Helices S5 and S6 contributing to the pore formation are shown in blue. Helices S1-S4 forming voltage sensing domains (VSD) are in silver. An approximate location of the pore is indicated by the dashed line. Helix S4 of domain VSDIV is shown in purple. The C-terminal domain (CTD) is presented in orange and located close to it the hypothetical inactivation gate (IG) marked in red (a surface representation) as a part of DIII-DIV linker (red). Toxin binding site 3 region (dotted circle) is delineated by Glu1255 (yellow) and N-acetylglucosamine (NAG) molecule (cyan). In the top view, a single sodium ion is indicated as a red dot.

Since site 3 and IG of Nav channel are located on opposite sides of the cell membrane, in order to affect conductance, the presence of a toxin must be communicated to a distant location in the channel, implying allosteric effects in Nav channels. However, the precise mechanism on the molecular level of changes induced by toxin binding leading to the inhibition of Nav channel inactivation is still elusive. Here, we present data that contribute to a better understanding of the first part of this process, i.e., toxins-Nav channel interactions.

Recent determination of the cryo-electron microscopy (cryo-EM) structure (2.6 Å) of Nav channel from American cockroach, *Periplaneta americana*, (NavPaS) allowed us to perform molecular docking of selected toxins to Nav protein and to monitor toxin-channel interactions [15]. Moreover, based on electrophysiological studies, we were also able to measure effects of these peptides on electrical signaling in isolated cockroach nerves. The aim of our research was to compare interactions of different sea anemone toxins, Av1, Av2, Av3 from *Anemonia viridis* venom (formerly ATX I, ATX II, ATX III from *Anemonia sulcata* venom) and CgNa from *Condylactis gigantea* venom with insect NavPaS channel. Such knowledge will contribute to the understanding of the boundaries of receptor site 3 and may be useful in design of new, natural toxins-derived drugs [16].

2. Results

A schematic structure of NavPaS studied here, based on cryo-EM measurements from 2018 [15], is presented in Figure 1.

2.1. Electrophysiology

The four sea anemone toxins differ in sequence and structure (Supplementary Information (SI), Figure S1); thus, we set to compare their effectiveness in physiological conditions. We used a system for extracellular recordings of isolated cercal nerve activity of the cockroach [17]. Nerve activity was quantified as a size of response to a mechanical stimulus. In control conditions, the level of nerve activity remained constant (94.1–101% of the initial activity) over 20 min of experiment (Figure 2b).

Sea anemone toxins were expected to increase the cockroach nerve activity because, as it was shown in 1984, they prolong considerably action potentials in isolated giant axons [18]. Indeed, in the cercal nerve preparation, all toxins induced a progressive increase of the response to mechanostimulation (Figure 2). As an example of our experimental results, a comparison of nerve activity between the control and Av3 toxin treated preparations is presented in Figure 2a. Within 20 min after application, Av1 toxin caused an increase of nerve activity to 147.3 ± 9.8% of the initial control value (the Fisher's least significant difference (LSD) test, d.f. = 138.189, $p < 0.001$, Figure 2b). The structurally similar toxin Av2 caused a much weaker effect. After 20 min, the nerve activity was only 117.9 ± 10.8% of the initial value and did not significantly differ from the control values (Figure 2b). Application of the structurally unique Av3 toxin resulted in an intermediate increase of the nerve activity. The endpoint activity was raised to 130.0 ± 10.1% of the initial value (LSD test, d.f. = 139.035, $p < 0.001$, Figure 2b). The last toxin tested—CgNa—caused the fastest and greatest increase of activity, to 149.6 ± 10.9% of the initial value (LSD test, d.f. = 139.035, $p < 0.001$, Figure 2b). Notably, the effects of Av2, Av3, and CgNa were fast, visible already in the first few minutes of experiments. In contrast, the impact of Av1 was observed with delay, and the first increase of nerve activity was noticeable only after 10 min of toxin application (Figure 2b).

Among the four toxins tested, the influence of Av2 on the nerve activity was significantly lower than the effects induced by the other toxins (Av1 vs. Av2 d.f. = 138.132, $p < 0.01$; Av3 vs. Av2 d.f. = 139.035, $p < 0.05$; CgNa vs. Av2 d.f. = 139.035, $p < 0.001$; Figure 2c). Thus, the four toxins increased neuronal activity at different efficacies.

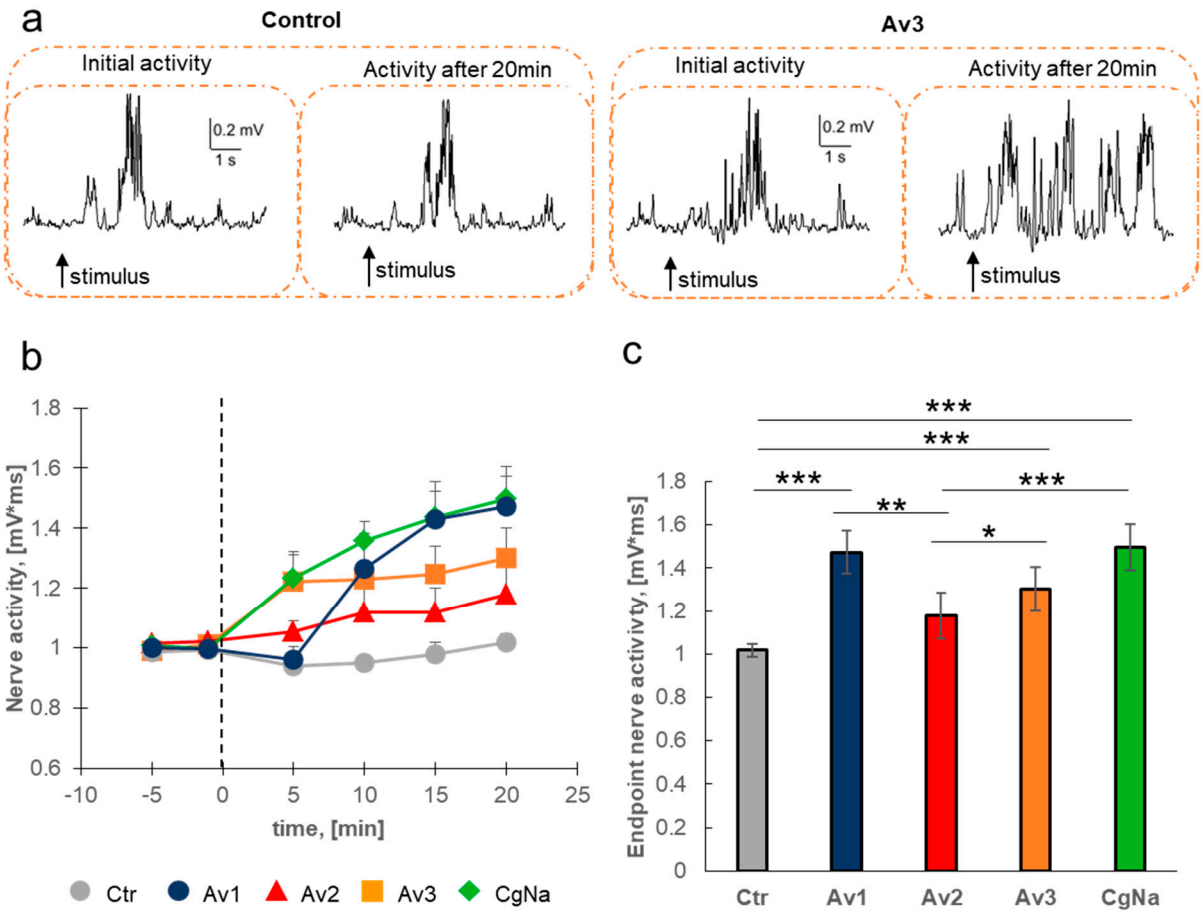

Figure 2. Sea anemone toxins increase the activity of the cockroach (*Periplaneta americana*) cercal nerve. (**a**) Original, representative records of cercal nerve activity are presented for control and after sea anemone toxin (Av3) application. The moment of stimulation is marked by an arrow. (**b**) Normalized nerve activity (measured as a surface under the peaks for response to mechanical stimulation of *cerci*—mV*ms) is presented in time after toxins application. Black dashed line represents the application of toxin in time "0"; the mean of values before toxin application was set as "initial value". Grey dots represent control values, blue circles represent Av1 toxin, red triangles represent Av2 toxin, orange squares represent Av3 toxin, and green diamonds represent CgNa toxin. (**c**) For clarity, statistical differences between all groups were shown for the endpoint (activity in 20 min after application of toxin). The statistically significant differences between control and tested toxins are marked: * $p < 0.05$, ** $p < 0.01$, *** $p < 0.001$. The data is presented as mean values ± SE, $n = 8$.

2.2. Molecular Docking

A schematic structure of NavPaS used for molecular docking is shown in Figure 1. Anemone toxins were docked using Scoring and Minimization with AutoDock Vina (SMINA) software [19] to the whole sodium channel, but only the lowest energy poses localized in the site 3 region (DIV-DI) (see Figure 1) were further scrutinized. Amino acid sequences of Av1, Av2, Av3, and CgNa may be found in Figure S1 (SI). For docking of Av2 the homology model was used (see Materials and Methods). However, for Av1, Av3, and CgNa, where 8, 28, and 20 NMR alternative structures are published in Protein Data Bank (PDB) (codes: 1ATX, 1ANS, 2H9X), respectively, a selection was necessary. We performed preliminary screening docking in order to determine which alternative NMR toxin structure gives the best SMINA score. For example, in the Av1 set, the best SMINA score was −4.89 kcal/mol, and the worst −4.18 kcal/mol, with a standard deviation in this population of 0.30 kcal/mol. The same data for Av3 NMR structures are −9.72, −7.25, and 0.58 kcal/mol, respectively. These numbers show that a toxin structure flexibility may contribute up to 2.5 kcal/mol in SMINA score, related to the energy of binding. Eventually,

for Av1, model 7; for Av3, model 4; for Av3′, (an alternative binding pose of Av3, see below) model 24; and for CgNa, model 19, from PDB database were selected for further analysis.

Structures of the anemone toxins selected are presented in Figure 3. Main residues being in close contacts (distance <2.5 Å) with NavPaS upon docking and their hydrophobic/hydrophilic character are indicated. The charge of the selected residues involved in sodium channel interactions is indicted by coloring in Figure 3. Anemone toxins contain 3–6 charged residues and are, therefore, easily soluble in water.

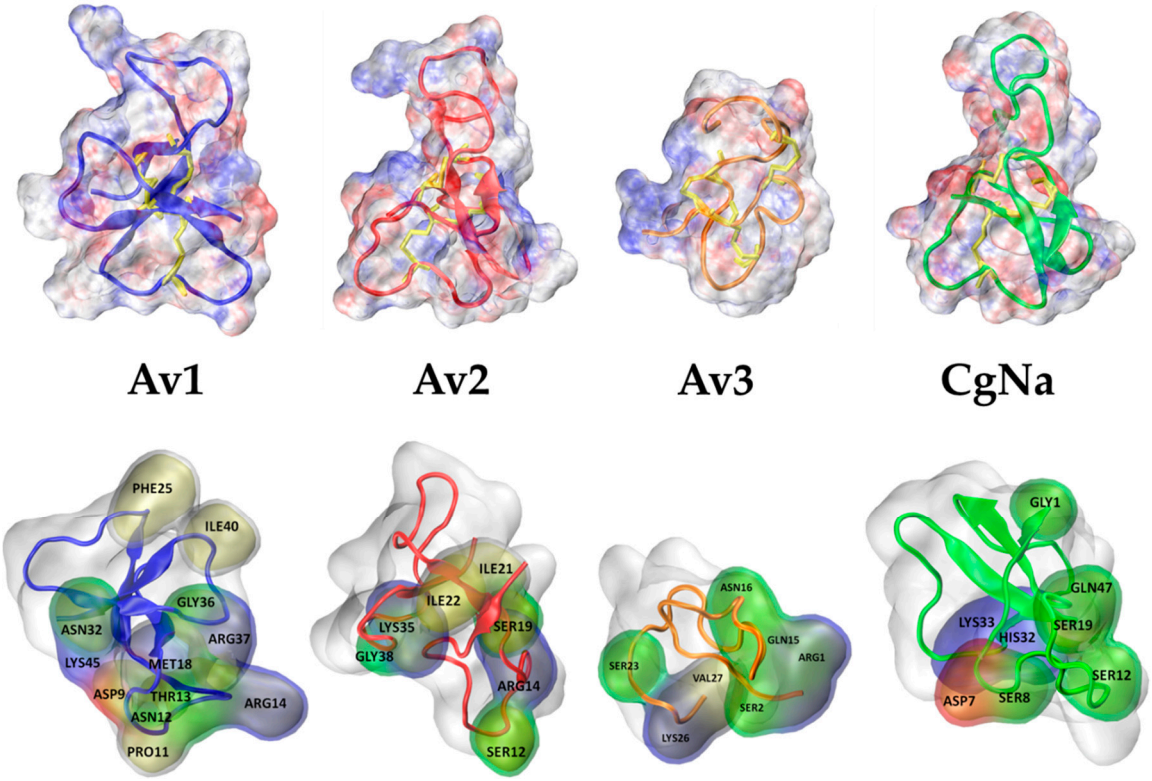

Figure 3. Upper panel: Molecular shapes of anemone toxins studied. In the upper row, electrostatic potential is mapped on a molecular surface; positive = blue, negative = red. In cartoon representation, a peptide backbone is shown, and disulfide bonds are marked in yellow (licorice shapes). Lower panel: Neutral (green), hydrophobic (yellow), and charged (positive = blue, negative = red) residues being in close contacts with NavPaS site 3 residues are indicated.

In Figure 4, electrostatic potentials, calculated using the method based on Poisson-Boltzmann equation [20] implemented in PDB2PQR server, Adaptive Poisson-Boltzmann Solver (APBS) module in Visual Molecular Dynamics (VMD) [21], and projected on the solvent accessible surfaces of the interacting toxins' residues and the site 3 region of NavPaS, are depicted. Coloring facilitates analysis of charges compatibility between toxins (Figure 4a–d) and the site-3 region of NavPaS (Figure 4e).

Toxins are located in a close vicinity of site 3, in the extracellular region of DIV-DI junction (Figure 1, Figure 5). The selected representations showing modes of docking and used for further analysis are presented in Figure 5.

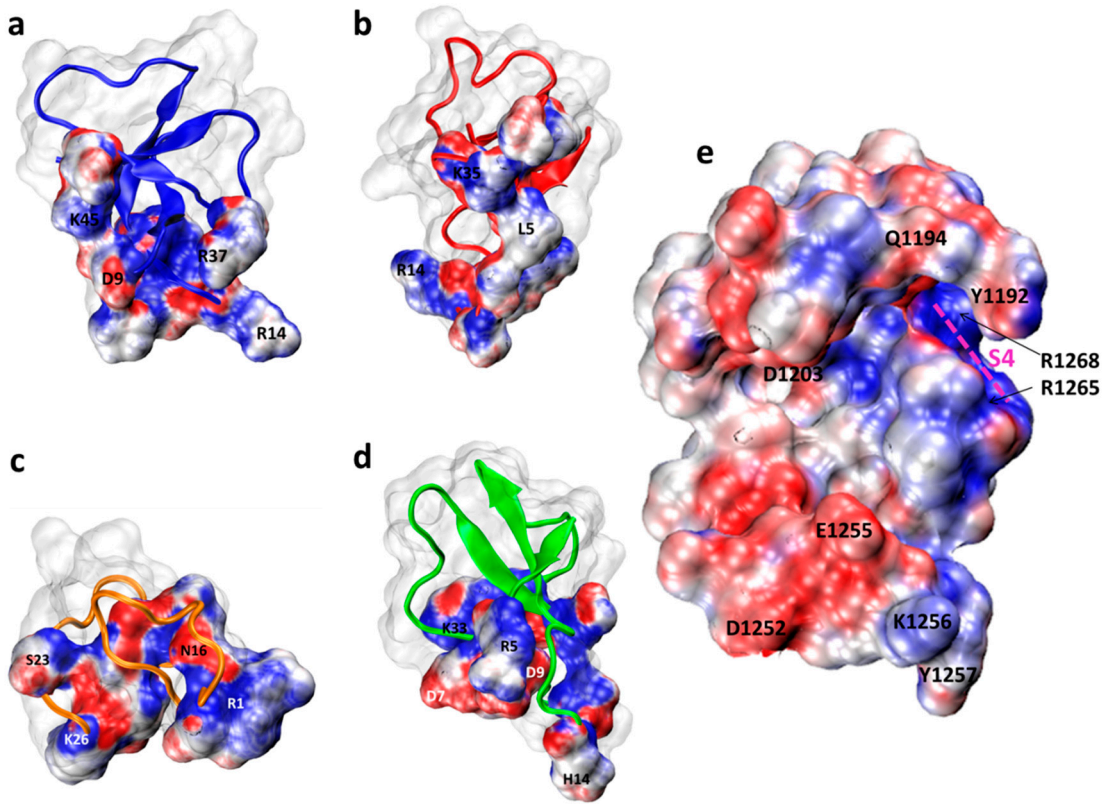

Figure 4. Electrostatic potential maps projected on solvent accessible surfaces of anemone toxins, parts involved in the interface: (**a**) Av1, (**b**) Av2, (**c**) Av3, (**d**) CgNa, and (**e**) the site 3 region of NavPaS visualized from the extracellular side accessible to toxins. In red, negative potential regions are shown, and positive ones are in blue. The neutral regions are white/gray. Note that toxins projections are simply shifted from the docked complexes without mirror reflection. The Visual Molecular Dynamics (VMD) software was used to make these figures [22].

In Table 1, we show parameters calculated to characterize intermolecular interactions of toxins with the channel. SMINA scoring function (SSF) is proportional to the expected binding energy. The negative values indicate that all toxins upon binding are stabilized. Clearly, the binding energy of Av3 is the lowest one (see Table 1, SSF).

Table 1. Parameters (*) characterizing interactions of anemone toxins with NavPaS channel.

Parameter *	Av1	Av2	Av3	Av3′	CgNa
Activity in experiment	$$$	$	$$	$$	$$$
SSF (kcal/mol)	−4.89	−4.98	−9.72	−8.85	−5.53
Total RRCS (AA)	122.10	86.00	152.80	145.90	119.13
Total RRCS for NAG	26.63	19.90	13.90	2.53	38.08
RRCS S4 only	14.80	7.52	21.84	6.51	10.14
Toxin AA in interface (%)	61	55	85	78	70
NAG atoms in interface (%)	68	75	50	46	86
ASA_TI (%)	34	22	46	45	37
ASA_NavI (%)	1.40	1.20	1.40	1.40	1.70
% BSA Glu1255	98	74	43	89	72
% BSA Arg1265 (S4)	77	54	94	31	35
% BSA Arg1268 (S4)	27	0	83	22	0
% BSA NAG	35	42	25	20	42

(*) for description of parameters, see the text.

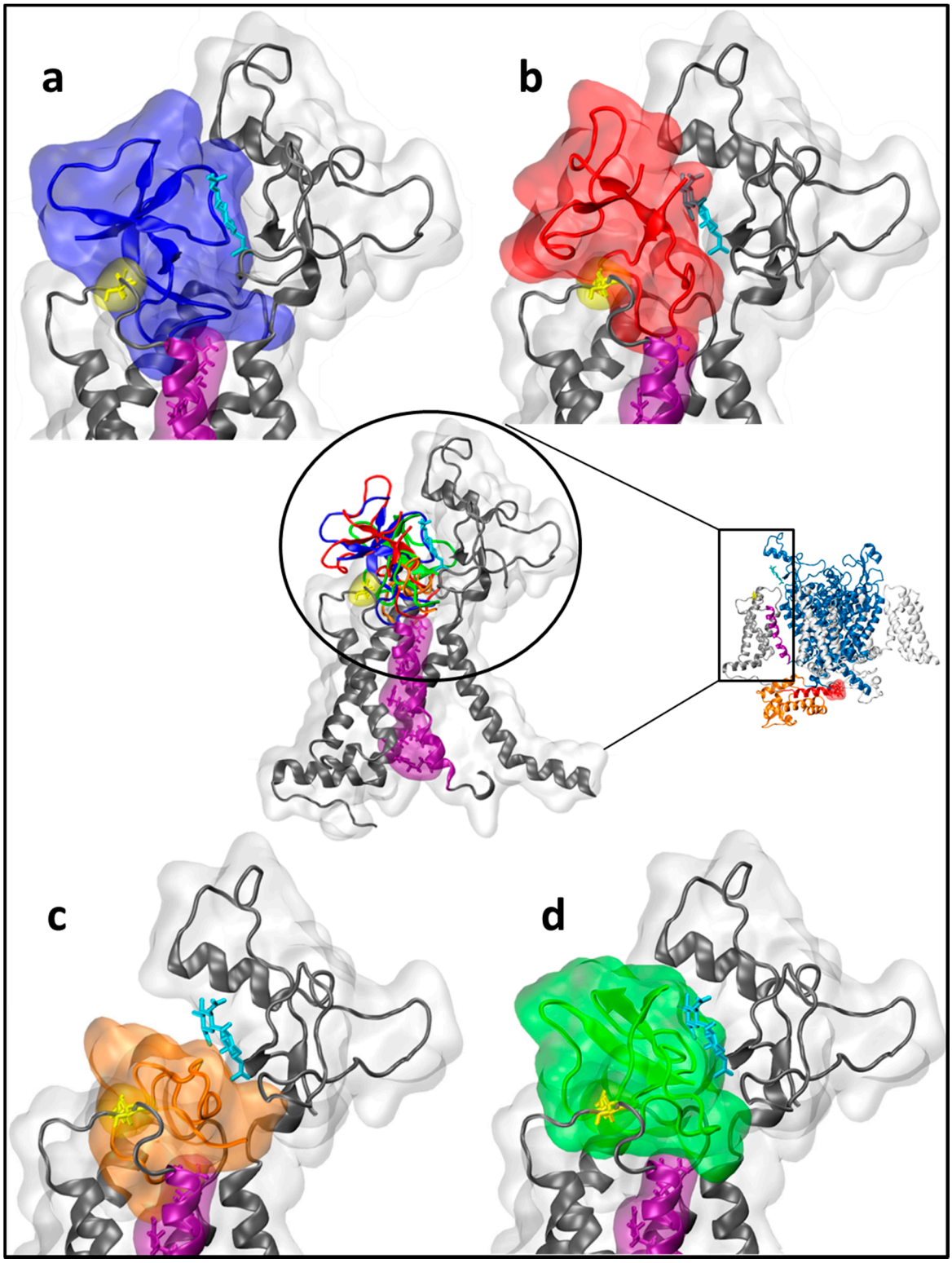

Figure 5. Representations of toxins binding to NavPaS channel site 3: for clarity, only a part of DIV (middle) is presented; (**a**) Av1 = blue, (**b**) Av2 = red, (**c**) Av3 = orange (**d**) CgNa = green. In purple, helix S4 is presented, E1255 is shown in a yellow licorice representation, and N-acetylglucosamine (NAG) is depicted in cyan licorice. A schematic structure of the whole NavPaS structure is presented in the middle right panel.

Recently introduced Residue-Residue Contact Score function (RRCS) (i,j) is defined as a distance based measure of possible interactions between a particular toxin residue i and a channel residue j [23]. Analysis of RRCS may facilitate studies of individual residues impact on NavPaS function. It is purely structural and static parameter but monitoring RRCSs in different stages of the ion channel "life-cycle" may lead to useful data on allosteric interactions and regulation. Here, RRCS allows for estimation of how tight a toxin is in a contact with the channel and how many residues are potentially involved in direct interactions with the toxin. Moreover, the analysis of RRCS shows how deep into the channel structure toxin effects may extend. The total contact score between toxins and the channel vary from RRCS=86 for Av2 to RRCS=152.8 for Av3 (Table 1). Notably, di-N-glycosylated residue Asn330 from NavPaS is a partner in all toxins binding, but to different degrees (Table 1). We denote this particular glycan side chain as NAG (2-acetamino-2-deoxy-beta-D-glucopyranose). The contact of Av3 with this glycan is significantly lower as compared to the other toxins. RRCS values for all scored residue pairs are available in Table S1 (SI). The non-zero RRCS data presented in Table S1 (in SI) delineate a broad site 3 region. Interestingly, the data presented in Table 1 indicate that all docked toxins are in contacts with S4 segment of DIV. This S4 DIV helix is critically important for the IG control [2]. Upon binding, between 55% (Av2) to 85% (Av3) of all amino acids in toxins are located in the channel-toxin interface region and perhaps participate in the binding. Therefore, the solvent has quite reduced contacts with sodium channel bound toxins. We quantified these arrangements by analyzing Solvent Accessible Surface Area (ASA) values. Parameter ASA_TI (in %) quantifies a percentage of toxin ASA coming from residues which contribute to the toxin-channel interface. In each case, ASA_TI is lower than 50% (Table 1). Notably, the ASA_TI value for Av3 is the highest, perhaps due to its high hydrophobic interacting surface [24] and small size. We also show ASA_NavI (in %)—an analogous parameter—showing a percentage of the whole NavPaS present in the interface. As expected, these are quite small numbers; only 1.2–1.7% of total channel ASA is covered by a toxin after binding. If we take into account only the extracellular part, these percentage will be higher by at least a factor of four. Still, we infer that the binding of toxin only weakly screens the channel from water, and this does not affect channel's structure.

We calculated Buried Surface Area (%BSA) for the channel residues Glu1255, Arg1265, Arg1268 which are possibly important for toxins binding and IG dynamics modifications (Table 1). Interestingly, all toxins covered Glu1255, and all are in a contact with top arginines (Arg1265, Arg1268) from voltage sensing helix S4 DIV, supporting their common mode of action on the sodium channel.

The small Av3, in contrast to the other toxins, exhibits four co-localized aromatic residues (Tyr7, Trp8, Trp13, Tyr18) previously suggested to participate in toxin binding [24]. Therefore, we added a relatively low energy pose Av3' having that region more deeply buried in the channel than the standard, i.e., the lowest energy Av3 structure, for further analysis. Data for the alternative binding pose (Av3') of Av3 toxin is presented in Table 1. Notably, whereas the RRCS for amino acid residues (AA) is highly similar to Av3 as is the SSF, the RRCS for NAG is significantly lower for Av3', suggesting weaker interaction with the D1 loop.

It is tempting to search for hot spots in channels structures affecting toxins binding with similar mode of action. A recent study [25] indicated that mutations of a histidine residue in *Drosophila melanogaster* Nav channel, located in analogous position to His392 in NavPaS D1 pore region, affect Av3 toxin modulation of sodium currents. Therefore, we performed several simulations of Av3 toxin docking into the following variants of NavPaS: His392Ala, His392Phe, His392Tyr. Results of docking to those protein variants are presented in Tables S2–S4 and Figure S5. The type of residue in the 392 position of NavPaS affects some close contacts between Av3 and the channel. However, the total RRCS values for Av3-channel residues contacts are similar in wild type (WT) and mutant variants (Table S2). We observed a closer contact of Av3 with NAG of mutated channel, as the pose of the toxin was shifted towards DI domain to which NAG is attached. Positions of Cα

of Av3 in the lowest energy pose in docking to H392F (SFF: −9.41 kcal/mol) and H392Y (−9.05 kcal/mol) overlap, with only differences observed in a region of Cys22-Val27. However, this Av3 terminal part gives a high contribution to the contact with S4 of VSDIV. Val27 of Av3 docked to the H392F Nav channel mutant interacts with Arg1268 from S4, which gives BSA value of this Arg equal to 83%. Similarly, high value of BSA for Arg1265 in H392T variant results from contacts with Val27 and Tyr7 of Av3. However, total BSA value for S4 arginines is the highest in the lowest energy pose of Av3 docked to the WT channel.

Another interesting position in the NavPaS channel is D1252, since mutations in analogous positions in various organisms affected anemone toxin binding [26]. Therefore, we repeated the four toxins docking procedures to D1252E, D1252R, and D1252A channel mutants. SMINA derived binding energies are indeed affected and are collected in Table S5 (SI). The relatively limited changes in toxins interaction to those channel mutants calculated here may suggest that channel mutations might modify its structure under physiological conditions, as have been demonstrated electrophysiologically for Av2 activity on the equivalent to D1252R, monitored on DmNav1-D1701R expressed in oocytes [24].

We determined what WT channel residues contribute the most to anemone toxin binding energy. Detailed contributions, estimated as values of a decomposed SSF score, are presented in Figure 6. According to our docking results, the NAG side group is a major player in anemone toxin binding. The second most important moiety is Glu1255. On average, Tyr1192, Ser1199, Gln1194, Arg1265 contribute approximately in a similar way to each toxin stabilization. The majority of channel amino acids involved in anemone toxin binding are from DIV domain, only two residues (Gln345, Asp303) are from DI. Notably, the roles of particular channel residues vary between toxins, but the list of channel's residues involved with substantial contributions to SFF (Figure 6) is limited (13 AA). Interestingly, the smallest toxin Av3 interacts apparently with 7 residues (Ser1199, Gln1194, Arg1265, Asp1203, Met1196, Tyr1257 and Pro1261) more strongly than the other toxins, in accordance with its highest interacting energy SSF (kcal/mol) (Table 1).

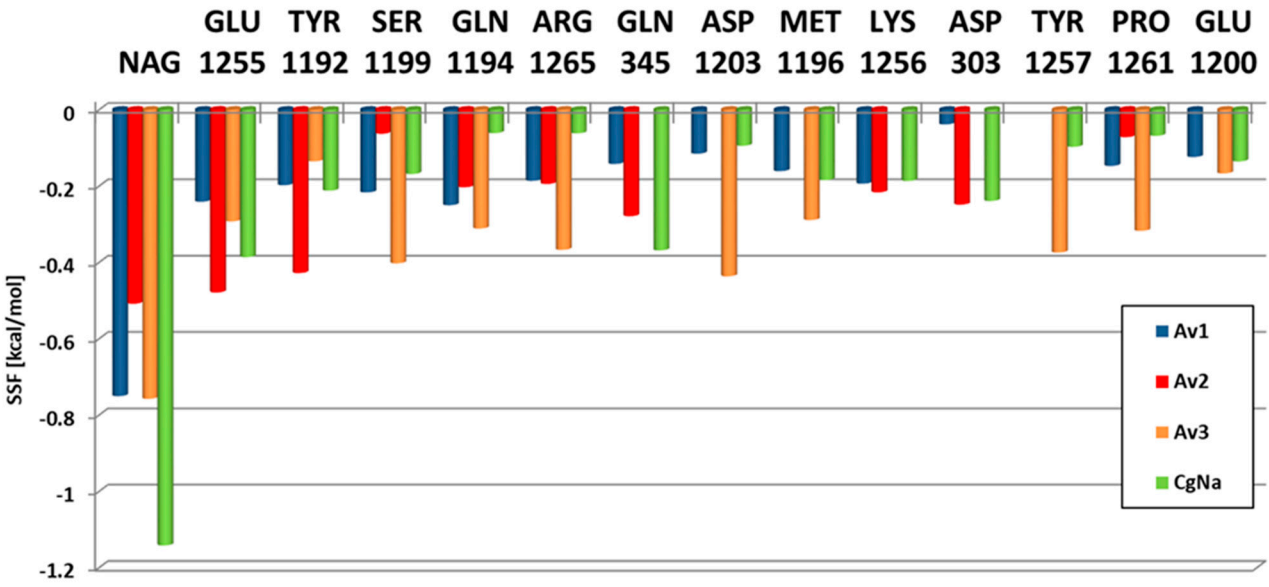

Figure 6. Contributions (in kcal/mol) of NavPaS residues to toxin binding energy measured by the SMINA scoring function (SSF) parameter. The role of each residue varies, depending on the toxin.

Data showing which amino acids from toxins are involved in binding to the NavPaS are presented in Figure S2 (SI). We observed that the toxins in their best poses engage the following residues (contribution to SSF > 1 kcal/mol): **Av1**: Arg14, Thr13, Ile40, Arg37, Pro11, Lys45, Asn12; **Av2**: Ser12, Val13, Asn16, Gln47; **Av3**: Arg1, Val27, Lys26, Trp13, Gln15, Ser23, Tyr18, Asn16, Pro25, Ser2; **CgNa**: Gln47, Trp31, Ser12, Trp23, Val13, Lys33, Gly1, His14, Arg5, His32.

Our best docking poses were further analyzed using server GetContacts [22]. Using this server, we determined possible hydrogen bonds and salt bridges between NavPaS and each toxin. Results are presented in Table 2 and Figure 7. This analysis shows that salt bridges are present in all toxins in poses exhibiting the lowest energy: Glu1255-Lys is seen in Av1 and Av2, while Asp-Lys is present in Av3 and CgNa (Table 2). Dominant interactions, shown in Table 2, are hydrogen bonds. Their number vary from 10 (Av2) to 19 (Av3). So, the high number of hydrogen bonds in Av3 (Table 2) correlates with the highest binding energy calculated by SMINA for this toxin (Table 1). Av3 is the smallest peptide, with only 27 amino acids, and because of that, it docks quite deeply in the site 3 region of NavPaS. Notably, in its alternative Av3′ pose two aromatic ring-cation interactions were discovered: Tyr1192-Arg1 and Tyr1204-Lys26. Interestingly, no aromatic residues of Av3 were involved in that type of interactions. Instead, Trp8 and Trp13 from Av3 oriented in the Av3′ pose participate in hydrophobic interactions with some five hydrophobic patches in the channel.

Table 2. Residue (#NavPaS)-residue (#toxin) interactions responsible for anemone toxin binding to NavPaS channel.

Interaction Type	Av1	Av2	Av3	Av3′	CgNa
salt bridge	ASP 359-ARG 14 GLU 1255-LYS 45 *	GLU 1255-LYS 35	ASP 1190-LYS 26 *		ASP 1203-LYS 33
π-cation				TYR 1192-ARG 1 TYR 1204-LYS 26	HIS 392-HIS 14 TYR 1192-HIS 32
H bond *s—side chain* *b—backbone*	sb MET 281-ARG 14 sb GLY 282-ARG 14 ss GLN 345-ARG 37 sb PHE 358-ARG 14 sb ASP 359-ARG 14 ss ASP 359-ARG 14 ss GLN 1194-THR 13 ss SER 1199-ASN 12 sb SER 1199-THR 13 ss ASP 1203-ASN 12	ss GLN 278-SER 12 ss GLN 345-ASN 16 ss GLN 345-THR 17 ss ASP 1190-SER 12 sb GLN 1194-SER 12 ss ASP 1252-THR 40 sb GLU 1255-LEU 5 ss GLU 1255-LYS 35 sb ARG 1265-GLY 10 s NAG-SER 19	ss GLN 286-ARG 1 ss GLN 286-GLN 15 ss ASN 330-ARG 1 sb SER 331-ARG 1 ss SER 331-ARG 1 sb GLN 345-ASN 16 sb SER 387-ARG 1 bb ALA 388-ARG 1 ss ASP 1190-LYS 26 ss GLN 1194-TYR 18	sb ILE 279-TRP 13 sb HIS 1191-ARG 1 sb GLY 1993-ARG 1 sb GLN 1994-ARG 1 sb GLU 1200-GLY 24 sb ASP 1203-LYS 26 ss ASP 1203-VAL 27 sb LEU 1248-TYR 7 sb GLU 1255-GLY 9	ss GLN 286-SER 12 sb ASP 303-GLY 1 ss TYR 1192-GLN 47 ss SER 1199-LYS 33 ss ASP 1203-LYS 33 sb GLU 1255-ARG 5 sb GLU 1255-ASP 7 b NAG-GLY 1 s NAG-HYP 3 s NAG-THR 21 s NAG-GLN 47
Av3′ hydrophobic	sb VAL 1253-LYS 45 ss GLU 1255-ASP 9 ss GLU 1255-LYS 45 ss LYS 1256-ASN 32 b NAG-GLY 36 b NAG-ILE 39 b NAG-ILE 40 b NAG-GLY 41		sb GLN 1194-VAL 27 ss SER 1199-TYR 18 sb SER 1199-SER 23 ss ASP 1203-SER 23 sb ASP 1203-GLY 24 sb THR 1262-SER 2 ss THR 1262-SER 2 sb ARG 1265-PRO 25 s NAG-ASN 16	*VAL 283-TRP 13* *ALA 388-TRP 13* *PHE 1258-TRP 8* *ILE 1259-TRP 8* *PRO 1261-TRP 8*	

The residues involved in anemone toxin- NavPaS hydrogen-bonded and salt bridges interactions are presented in Figure 7. Interacting pairs in best energy poses were determined by GetContacts server [22]. This presentation highlights the smallest number of Av3-channel interactions, which is in good agreement with our experimental results.

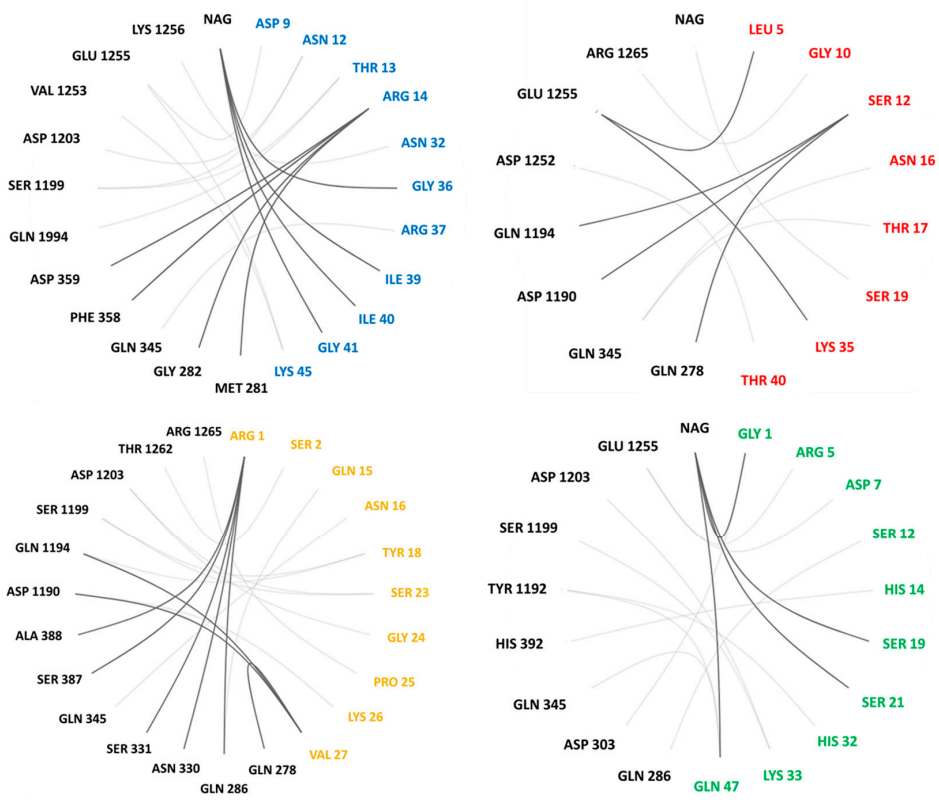

Figure 7. Pairs of residues forming hydrogen bonds and salt bridges between anemone toxins and NavPaS. Av1, Av2, Av3, and CgNa residues are indicated in blue, red, orange, and green, respectively. NavPaS residues are in black. Note that residues from 278–388 belong to DI, the rest to DIV of NavPaS. GetContacts server was used to determine contacts and prepare the plots [22].

3. Discussion

Ion channels are complex multi-domain membrane proteins and, therefore, present a big challenge to structural biology. The first cryo-EM structures of eukaryotic voltage dependent sodium channels were published in 2017 for NavPaS subtype from American cockroach (*Periplaneta americana*) [27] and EeNav1.4 from electric eel (*Electrophorus electricus*) [28]. Those extremely important successes opened up the possibility of (1) defining the structure of other different subtypes of Nav channels, (2) the more detailed studies of the mechanism of Nav channels functioning, (3) study of the effects of point mutations occurring in sodium channels and responsible for many diseases, and (4) determination of the mechanism of interaction between Nav channels and natural and artificial ligands that modify Nav activity. Such structural studies may reveal subtle differences in the Nav channel–ligand interactions for substances with apparently similar mode of action.

In the present study, we selected four sea anemone toxins [29] to compare their effects on the insect preparation containing voltage dependent sodium channels. All these toxins bind to receptor site 3 region in NavPaS [11] and inhibit its fast inactivation (see Figure 8). However, they differ in several aspects. Av1, Av2, and CgNa are larger peptides (46–47 AA, Type I sea anemone toxin) in comparison to the small Av3 (27 AA, Type III). While Av1 and Av2 are quite homologous [30], the amino acid sequence of Av3 is unrelated to Av1 and Av2 [11] (also see Figure S1 in SI). The 3D structures of these toxins are also different [31]. Type I toxins have a four-stranded, anti-parallel β-sheet linked by three loops with a conserved arginine (Figure 3) and three pairs of S-S bound cysteines [32]. The small Av3 lacks any secondary structure (see Figure 3), having a series of four turns (two type I turns and two γ turns) [33] stabilized into a compact form by three disulfide bridges: Cys3-Cys17, Cys4-Cys11, and Cys6-Cys22.

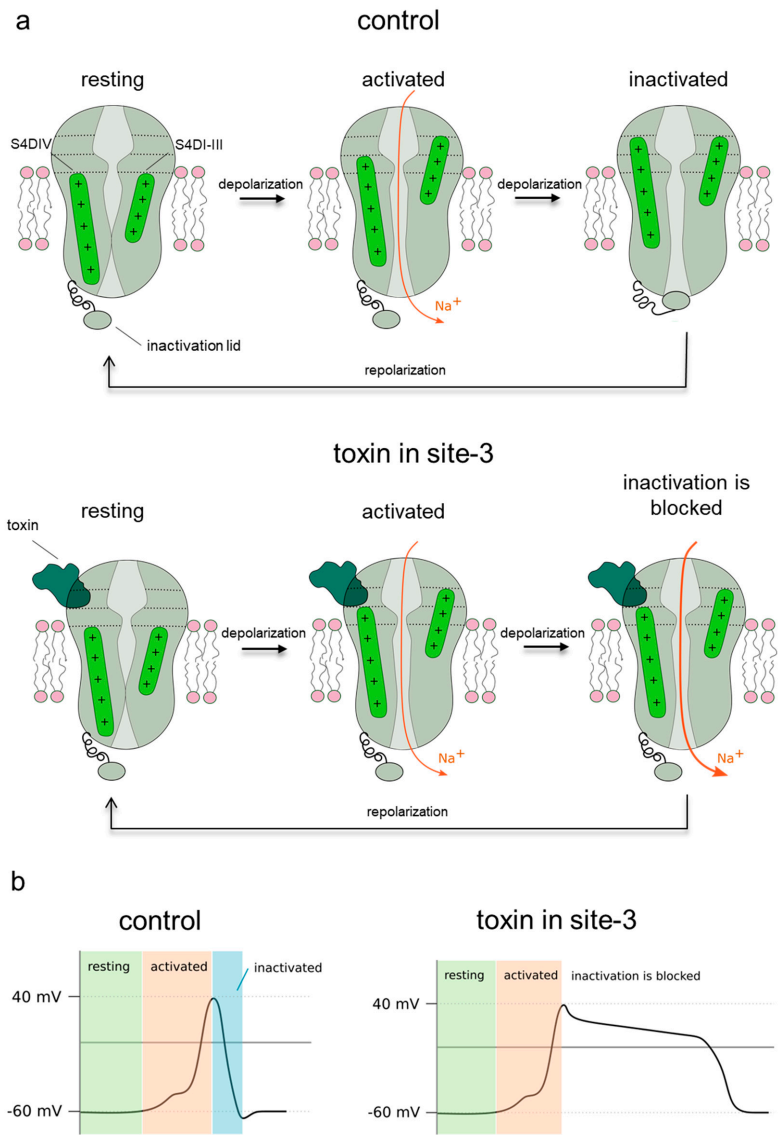

Figure 8. (**a**) Schematic representation of voltage gated sodium channel in control conditions (upper raw) and in the presence of site-3 toxins (lower raw). The inactivation gate and voltage sensors (S4) of domains I-III and domain IV are indicated in green. Depolarization of membrane from resting potential to positive values leads to sodium channel activation, where S4 are moved outward and activation gate is opened, making the sodium channel conductive to sodium ions. Reaching the activation state does not require a full S4 movement in the IV domain. In the next step, S4 of the domain IV makes full outward movement and releases the inactivation gate, which closes the channel. When the membrane potential returns to its resting values (repolarization), all S4s move inward which close channel and push out the inactivation gate from channel pore. In the presence of site-3 toxin (lower panel), the complete movement of S4 in IV domain is not possible, allowing the channel to remain activated, not allowing the inactivation gate to close. As a result, the channels are opened until the membrane potential reaches its resting values. (**b**) Representation of action potential generation in typical, isolated nerve cell: In resting state, the membrane potential is highly negative inside (green area). Depolarization pulse leads to opening of the sodium channels; rapid influx of sodium ion pushes the membrane potential to positive values (red area). Next, fast inactivation blocks the Na^+ conduction and the membrane potential returns to its resting value due to the outflow of potassium ions (blue area). In the presence of site-3 toxin, the inactivation of channels is inhibited; thus, they remain open and positive membrane potential is maintained (the *plateau* action potential is recorded).

All tested toxins induced an increase in the cercal nerve activity recorded under stimulation of the cercal mechanoreceptors (see Figure 2); our results are in accordance with previous research performed on different preparations. Av1, Av2, and Av3 caused repetitive firing in motor axons in the crayfish (*Astacus leptodactylus*) [34]. Av2 induced repetitive activity in the giant axon in situ in the cockroach's nerve chain (own unpublished data) and in frog skeletal muscle fibers [35]. Another anemone toxin (anthopleurin-B) increased nerve activity in frog spinal cord [36].

The excitatory effect of the tested toxins is usually explained by the similar mode of action of toxins that bind to receptor site 3 region on the sodium channel. Av2 and Av3 compete with the site-3 scorpion α-toxin binding to insect neuronal membranes [24,37]. When tested on single cells, they induce a large prolongation of action potential duration (for review, see Reference [11]). Such effect was observed also in an isolated giant axon of a cockroach after application of Av2 (formerly ATX II) and CTX (*Condylactis* toxin) [18]. Prolongation of action potential duration is the consequence of inhibition of sodium channel fast inactivation and an increase in the time constant of Na current decay under depolarization observed with site 3 anemone toxins acting on sodium channels from vertebrates and insects [24,38]. At the single channel level, site 3 anemone toxins prolong the open time of channels and often induce bursting openings [39,40]. It is worth noting that some isoforms of mammalian Nav channel can show quite different sensitivity to sea anemone toxins [41]. Some of them (cloned rNav1.2β_1, rNav1.4β_1, rNav1.7β_1, rNav1.8β_1 channels) appeared to be completely insensitive to CgNa [32].

In our study, we found differences in the efficiency of toxins to increase the cercal nerve activity (Figure 2). Differences in effective toxin concentration have been previously observed when comparing the effects of Av1, Av2, and Av3 sea anemone toxins on various crayfish neuronal preparations [34,42]. Later, three similar anemone toxins (ATX II, AFT II, Bc-III) were tested on six isoforms of mammalian sodium channels [43]. ATX II differs from AFT II by only one amino acid, and toxin Bc-III has 70% similarity with ATX II. Unexpectedly significant differences were found in dose-response modification of sodium current induced by these toxins [43]. Thus, our studies further support earlier observations that, despite similarity of amino acid sequences and structures, and/or similarity in mode of action, the binding modes of toxins to the sodium channel may vary greatly. In the present study, we tried to clarify this challenging matter.

Molecular modeling (MM) is currently a well-established tool for studying modes of ligand-protein binding, which we recently used for elucidating mosquito repellents–G protein-coupled recetor interactions [44,45]. Similar peptide toxins interactions with various Nav channels were recently assessed using MM [46]. Permeation of ions through a channel is important topic [47–50] and studied here NavPaS channel was recently analyzed by molecular dynamics (MD) simulations with respect to that, as well [51]. However, to the best of our knowledge, there were no data on Type I nor Type III anemone toxin docking to insect sodium channels.

Our SMINA based protocol (see Materials and Methods) enabled us to detect that all anemone toxins had low energy poses in a relatively limited fragment of NavPaS exposed to the extracellular medium (Figure 5). The common feature is "capping" S4 VSDIV helix by the docked peptides. Molecular electrostatic potential maps presented in Figure 4 show that binding is rather dominated by electrostatic forces and hydrophobic interactions have a minor role. All toxins form salt bridges between their positively charged lysine residues and negatively charged channel amino acids (Table 2). However, these critical interactions are not identical; Av1: Lys45-Glu1255, Av2: Lys35-Glu1255, Av3: Lys26-Asp1190, CgNa: Lys33-Asp1203. This is in a good agreement with experimental observations underscoring the role of lysines from C-terminal toxin region [13]. Data in Tables 1 and 2 shows that Av1, Av2, and CgNa are quite well stabilized by interactions with the channel residues. The value of SFF, being on the order of -5 kcal/mol, cannot be directly converted into a binding constant since the solvent effects were neglected in our docking; however, it shows similar propensity of these three toxins to the site 3 region.

In Av1, in accordance with previous observations [52], we observe strong involvement of Arg14 hydrogen bond and salt bridge interactions with domain DI region (Met281, Gly281; Phe358, Asp259; Table 2). Interestingly, Arg37 of Av1, involved in interactions with DI through Gln345 (Table 2 and Figure S2), is unique for Av1 sequence in comparison with other type I anemone toxins (see SI in [31]).

Av2 exhibited the lowest ability in modulation of neuronal activity in the cockroach neuronal preparation (Figure 2, Table 1). Its binding to the channel seems to be the weakest one, despite similar to other toxins SSF value, since RRCS of 86 is clearly much below the next smallest calculated value of 119 (CgNa). The surface of contact with the channel (ASA_TI) is only 22%, while, in the other toxins, it is in 34–46% range (Table 1). In Av2 the smallest number of hydrogen bonds is observed (Table 2). Interestingly, Ser12 seems to be a major player here, interacting both with DI (Glu28) and DIV (Asp 1190, Glu1194) residues. This residue was not denoted previously as important for Av2 binding in mutagenesis study [38].

CgNa has 47 amino acids and also has interactions (via Arg5, Table 2) with Glu1255 of NavPaS, which seems as most important for anemone toxins interaction. In this toxin interactions with NAG (via Gly1, Ser19, Thr21, Gln47) are particularly strong. A special role of Lys33 bound both to Ser1199 and Asp1203 is also visible. Despite a relatively small direct contact of CgNa with S4 (Table 2), this toxin is quite well stabilized. In the predicted position, it may block helix's S4 further motion "up" and prevent the fast inactivation of NavPaS.

A much better energetic stabilization of Av3 toxin (SFF ~ −9 kcal/mole) stems from the deeper localization of this small peptide in the DIV cleft. The number of NavPaS residues being in contact with Av3 is the highest in the series, and the total RRCS score (152 vs. 122 and 119 for Av1 and CgNa, respectively) is the highest, as well (see Figure 7, Table 2, Table S1 in SI). Parameters, such as a number of hydrogen bonds, RRCS, and BSA, obtained for Av3 (Table 1) indicate that Av3 exhibits the strongest interaction with S4. Due to its relatively small size, together with loose contacts with Glu1255 and NAG, it is tempting to speculate that Av3 might be partially moving together with S4 upon increase/decrease of the membrane potential. This may explain why the effect of Av3 on insect preparation electrical activity was weaker than that of Av1 and CgNa (Figure 2).

Av3 toxin affects specifically arthropods, while mammalian brain Nav1.2a channels are insensitive to this toxin. In a recent paper [25] mutagenesis studies suggested that in the *Drosophila* DmNav1 channel Trp404 and His405 localized near the membrane surface in D1 are a part of the channel receptor site interacting with Av3. The sequence of insect channels in this region is highly conserved (see Figure S4 in SI) and differs from mammalian Nav channels. Using our protocol, we docked Av3 to His392Ala, His392Phe, His392Tyr variants of NavPaS. The SSF score is similar to those obtained in docking to WT channel (Table S2 in SI) and poses are in the site 3 region, as well (Figure S5 in SI). Analysis of Av3 binding modes (Figure S5 in SI) and toxin-channel close contacts (Tables S3 and S4 in SI) indicate that Av3 indeed has low energy (−9 kcal/mol) poses, being in contact with that DI/SS2–S6 linker region. However, the differences in the calculated Av3 binding energies alone do not explain diverse effects of the toxin on those mutants in a chimeric Nav channel [25], suggesting that perhaps dynamic toxin-channel interactions are missed in our docking models.

By combining results of computational analysis, we selected the most important residues that contribute to anemone toxins binding to NavPaS. For Av1 these are: Asp9, Asn12, Thr13, Arg14, Arg37, and Lys45. For Av2, we found **Leu5**, Gly10, Ser12, **Asn16**, Thr17, Lys35, and Thr40 to have the substantial role. This is in a partial agreement with mutagenesis studies results [38], in which Val2, **Leu5**, **Asn16**, Leu18, and Ile41 were indicated as key players in the binding. Notably, our Thr17 and Thr40 are in the same region of Av2 as Leu18 and Ile41, noted in experiments as important. The involvement of Arg14 in Av2 binding, discussed in [38], is observed only in one of higher energy poses of this toxin. It is plausible that dynamic changes of the toxin in solution upon binding may

differ from the toxin structure in our MM conditions, which may account for some of the differences observed. Analysis of CgNa docking (Table 2, Figure S2) showed that Gly1, Arg5, Asp7, Ser12, His14, Lys33, and Gln47 are the most important CgNa amino acid residues in NavPaS binding. Majority of them are polar or charged residues.

A more complex analysis was required for Av3 toxin, as we found two low energy poses (using different NMR models) that are favorable in terms of electrostatic potential (Av3, model 4) or hydrophobicity (Av3′, model 24). Moran et al. [24] showed that mutation of **Arg1**, **Tyr7**, **Trp8**, Pro12, **Trp13**, **Tyr 18**, Glu20, and Ser23 decreased toxin binding affinity to cockroach neuronal membranes. In our docking study, we found five of these residues (shown in bold) as crucial in binding to NavPaS, distributed in Av3 and Av3′ poses. For Av3, we selected **Arg1**, Ser2, Gln15, Asn16, **Tyr18** and Val27 and for Av3′ **Arg1**, **Tyr7**, **Trp8**, Gly9, **Trp13**, Gly24, Lys26, and Val27. Indeed, our pose Av3′ have aromatic residues buried deeply in the channel groves. We suggest that, in native NavPaS channels, both binding poses (Av3, Av3′) are possible, and both may modulate electrical activity, but in Av3 pose the toxin may have stronger effect on IG through stronger interactions with S4 (see Table 1).

Possible Hot Spots in Toxin Binding to Site 3 of Sodium Channels

In previous experimental research on sodium channels residues critical for toxin binding, the role of a negatively charged aspartic acid residue, the equivalent of NavPaS Asp1252, have been examined. This residue, located in S3–S4 loop of VSDIV, is conserved in insects and some mammals. Mutagenesis study performed on *Xenopus* oocytes expressing *Drosophila melanogaster* Nav (DmNav1) channel showed that substitution of aspartic acid to arginine (D1701R) abolished the effects of Av2 and scorpion site-3 toxin LqhαIT [24]. In contrast, the DmNav1^{D1701R} mutation has only minor effect on Av3 activity. In the rat brain rNav1.2a channel, which is insensitive to Av3 and LqhαIT toxins, there is glutamic acid in the equivalent position. A single substitution E1613D was found to convert rNav1.2a channel from being insensitive to highly sensitive toward scorpion LqhαIT toxin [53]. Interestingly, a single substitution of aspartic acid to glutamic acid in the equivalent position in rat skeletal muscle rNav1.4 channel (D1428E) decreased the effect of LqhαIT [54]. In our molecular docking study, we observe that Asp1252 slightly contributes to the binding energy (SSF) of Av2 (−0.75 kcal/mol) and Av1 (−0.1 kcal/mol) but does not participate in Av3 and CgNa binding. Asp1252 can also form a hydrogen bond with Thr40 of Av2. The higher affinity of Av2 than that of Av3 toxin to NavPaS Asp1252 is in good agreement with mutagenesis studies [24].

The effect of channel mutation D1252X varied between investigated toxins (Table S5 in SI). We observed the most striking impact in Av1, binding of which to the site 3 region of NavPaS mutants was completely abolished (see Table S5 in SI). The D1252R mutation in channel increased the SSF energy of Av2 binding with respect to WT by 0.32 kcal/mol. Although this change in SSF value is limited, dissociation rate of toxin could be increased due to steric interactions in response to depolarization followed by S4 movement [26]. Surprisingly, our D1252R mutation of NavPaS improved CgNa binding by 0.3 kcal/mol, while no effect was observed in binding to neither D1252E nor D1252A mutant variants. Results of SMINA values for D1252X variants should be interpreted with caution, since here we take into account only local, limited to D1252 site, relaxation of NavPaS structure. Possible large scale structural effects of mutations are not included in the modeling. There is also no experimental data providing D1252X structures.

However, our docking results clearly suggest that the most important amino acid residue for the investigated toxins binding is Glu1255 (Figure 6, Table 2). Notably, this residue is conserved in insect and some mammalian Nav channels. Substitution of corresponding Glu by Gln (E1589Q) in human Nav1.7 channel reduced the effects of CvIV4 scorpion toxin [55] and selectively decreased ProTx-II ability to induce sustained currents around 6-fold [56]. Experimental studies on mammalian Nav1.2a channels revealed that substitution of corresponding Glu by Gln or Arg (E1616Q, E1616R) both significantly decreased affinity for Av2 but not for scorpion α-toxin LqTx [26]. Although sea anemone

toxins and scorpion α-toxin bind to overlapping sites, non-identical amino acids of site 3 are crucial for their activity [57].

Possible NavPaS Residues Affecting Anemone Toxin Binding

We found that receptor site 3 on the NavPaS channel comprises a broad region in domains DIV and DI, based on the combined data collected in Table 2, Tables S1a and S3 (SI), and Figure 7. The most detailed information come from RRSC which shows close contacts between toxin and channel atoms without assessing any particular physical interaction. The contacts result from calculated optimum docking poses. The broad site 3 region of cockroach NavPaS channel found in this study, based on RRCS cutoff of 1.0, encompasses the following residues:

- DI: [**S5:** Gln278, Ile279], [**EC3:** Met281, Gly282, Val283, Gln286, Phe301, Asp303, Trp306, Phe307, Gly329, Asn330, NAG1601, NAG1602, Ser331, Gln345, Tyr347, Phe358, Ap359], [**EC4:** Ser387, Ala388, His392]
- DIV: [**S1–S2 loop**: Asp1190, His1191, Tyr1192, Gly1193, Gln1194, Met1196, Ser1199, Glu1200], [**S2:** Leu1202, Asp1203, Tyr1204, Asn1206], [**S3:** Gly1247, Leu1248], [**S3–S4 loop:** Asp1252, Val1253, Ile1254, Glu1255, Lys1256, Tyr1257, Phe1258, Ile1259, Pro 1261, Thr1262], [**S4:** Leu1264, Arg1265, Arg1268].

Important observation from the present analysis is the role of NAG group in anemone toxin binding. NAG1601-NAG1602 form a part of site 3 region (Figure 5). Glycosylation in a position corresponding to Asn330 of NavPaS is conserved in human Nav channels and was recently found to play a role in scorpion AaH2 toxin binding [58]. Increased potency of AaH2 for Nav1.2 over Nav1.7 was linked to the fact that Nav1.2 have glycosylated Asn residue in site 3, while Nav1.7 do not have such modification [58]. It is known that glycosylation is a tool of evolution [59] and affects sodium channels function [60]. It would be interesting to know whether the presence of NAG in places corresponding to the site 3 of NavPaS has any special biological role. Experimental studies focused on NAG might resolve this issue.

The mechanism of anemone toxin impact on NavPaS channel inactivation discussed earlier for site 3 toxins [2] is summarized in Figure 8, and refers to our data, as well.

Now, we ask the basic question: should we expect the full agreement between our modeling and mutagenesis studies [24,38], since both NavPaS channel and toxins' structures are known? The answer is not so straightforward. If one assumes, that the anemone toxins "attack" sodium channels in a single and unique mode, then our results seem to be disappointing. However, toxin peptides are partially flexible structures. NMR results in up to 24 alternative structures [33], with RMS distance up to 2 Å. Our SMINA rigid docking shows that binding energies of Av3 and Av3' differ by less than 1 kcal/mol. Thus, anemone toxins are able to dock in heterogeneous way, and exact distributions of the poses may depend on experimental conditions.

Our MM results are based on several assumptions. One should remember that the SMINA scoring functions, being universally accepted, is one of many theoretical models for toxin-channel binding. For example, other approaches may give different distributions of electrostatic potentials (Figure 4). Since the peptides are quite rich in hydrophilic residues (see Figure 3) we have assumed that water contributes to all toxins in the same way. However, solvent effects may preferably stabilize some toxin poses. The static NavPaS channel structure adopted here is also approximate. We assume that the structure (PDB 6A95) used here, resembles the most abundant natural resting state of this insect channel, but during the working cycle of NavPaS distinct conformations of the site 3 region might be envisaged. Data of RRSC presented in Table S1 should be helpful in tracing allosteric effects in inactivation of sodium channels [58]. How the presence of toxin in the extracellular part of the channel mechanically affects IG located about 80 Å apart cannot be deduced from our docking studies, yet. So, performing extensive molecular dynamics simulations may bring new data on this fascinating but complex systems. We plan to perform such investigations in our lab.

4. Materials and Methods

4.1. Electrophysiology

Material: Electrophysiological experiments were performed on adult, male American cockroaches (*Periplaneta americana*). Insects were reared in our own colony, kept a 29 ± 2 °C, fed with oat flakes, apples, and dog food and water ad libitum. Twenty-four hours before the experiment, the cockroaches were moved to room temperature (21 ± 1 °C).

Chemicals: Physiological saline was prepared with 210 mM NaCl, 3.1 mM KCl, 5 mM $CaCl_2$, 5.4 mM $MgCl_2$, 5 mM Hepes. pH was adjusted to 7.4 with NaOH. All chemicals were purchased from POCH. SA., Gliwice, Poland. The toxins Av1 and Av2 and Av3 were isolated from sea anemone *Anemonia viridis* venom (formely ATX I, ATX II, ATX III from *Anemonia sulcata*) [61], CgNa toxin was isolated from the *Condylactis gigantea* venom [62]. Lyophilized toxins were dissolved in physiological saline to 0.1 mM concentration and then diluted to 1 μM.

Electrophysiological experiments: To determine the effects of anemone toxins on the bioelectrical activity of the cercal nerve, the extracellular recordings were conducted as previously described [17]. Abdominal part of cockroach's escape system was isolated from insect body. The preparation consisted of two *cerci*, cercal nerves, terminal abdominal ganglion, and short part of connective nerves. In the experimental chamber (3.5 cm Petri dish), the preparation was slowly perfused with physiological saline, while *cerci* were kept dry. Compound bioelectrical activity of cercal nerve was recorded using extracellular electrodes (Alpha Omega Engineering LTD, Nof HaGalil, Israel). Signals were amplified by a differential amplifier, observed at oscilloscope (Hameg 507, Hameg Instruments Gmbh, Mainhausen, Germany) and stored in a computer. Data were analyzed using modified Hameg software.

During each recording at first the spontaneous ("resting") activity was recorded during 40 ms. Then, mechanoreceptors covering the *cercus* were stimulated with gentle air puffs, generated by loudspeaker membrane movements controlled by impulse generator with 0.4 Hz frequency. The response to *cercus* stimulation was seen as an increase of cercal nerve activity, appearing just after the stimulation. Usually the response was well defined and its size was estimated as the area under the response peaks. Nerve activity returned to a resting level up to 50 ms (Figure 2a). Each preparation was allowed to stabilize for 10 min before the activity registration. The initial activity was recorded for 5 min and then the physiological saline (in control) or toxin was applied at a concentration of 1 μM. The effects of the toxin were recorded for 20 min.

The treatment effect with anemone toxins on nerve activity was tested by a one-way generalized linear mixed model (GLMM). We included measurement time (minutes of the test) as a continuous variable and replicate as a random factor. Nerve activity was used as a dependent variable while toxin (Av1, Av2, Av3, CgNa) as main factor. Each analysis was followed by multiple comparisons using Fisher's LSD post hoc test. Analysis was conducted in the IBM SPSS 25 Statistics software (IBM Corporation, Armonk, NY, USA). The results were expressed as mean values ± SE. The differences were considered as significant when $p < 0.05$.

4.2. Molecular Modeling and Docking

We performed molecular docking of four toxins to the *Periplaneta americana* voltage-gated sodium channel (PDB: 6A95) using SMINA package [19], a fork of Autodock Vina [63] that provides enhanced support for minimization and scoring. After removing of spider toxin Dc1a present in the original structure. we carried out a single rigid docking run for each NMR derived model of CgNa (PDB: 2H9X), Av1 (PDB: 1ATX), and Av3 (PDB: 1ANS) and selected two best scored models for further studies of each toxin. Then, we performed next round of 5 independent rigid docking runs per each model using default SMINA settings, generating up to 100 poses per run. We build a homology model of Av2 toxin using SWISS-MODEL structure homology-modeling server [64] with the following structures of sea anemone toxins as templates based on highest sequence homology structures with

PDB codes: 1AHL, 1APF, 1SHI. For the best scored homology model of Av2, we performed 10 independent docking runs. Thus, we have obtained more than 5000 docking poses. We added hydrogen atoms using CHARMM-GUI server [65] and then analyzed and visualized results with the VMD code [21] and home-made scripts.

A residue-residue contact score (RRCS) is an atomic distance-based parameter that quantifies the strength of contact between residue pairs by summing up distances in all possible inter-residue heavy atom pairs [23]. For each docked toxin, we calculated RRCS values using the python script provided by Zhou et al. and further analyzed data with NumPy package. We calculated the Accessible Surface Area (ASA), Buried Surface Area (BSA), and percentages of residues corresponding to the toxin-channel interface using PDBePISA server [66]. GetContacts [22] server was used to identify toxin-channel interaction residues and a character of those interactions (hydrogen bonds, salt bridges, etc.). To create maps of electrostatic potential for toxins, we used PDB2PQR server [67] and APBS in VMD [21].

5. Conclusions

Electrophysiological experiments revealed different effects of four sea anemone toxins on *Periplaneta americana* neuronal preparations activity. Av1 and CgNa are the most potent toxins affecting inactivation process of sodium channel, while Av2 has the lowest impact on inactivation.

Our molecular docking with SMINA software [19] provides firm arguments that Av1, Av2, Av3, and CgNa bind in site 3 extracellular part of NavPaS channel. The low energy modes of binding prefer surfaces of toxins that fit the best in terms of a number of hydrogen bonds and salt bridges to the channel surface. We noticed that hydrophobic contacts play less significant role in sea anemone binding to NavPaS. We observe moderate compatibility of electrostatic potentials surfaces between all four toxins and the site 3 NavPaS region. The contact areas toxin-channel moderately correlate with activity modulation effect observed in electrophysiology measurements in cockroach neurons. The docking poses obtained support the molecular model in which the upward motion of S4 helix in DIV domain is hampered by the presence of the anemone toxin in site 3 (Figure 8). The inactivation gate, in this case pivoted by the Alanine-Threonine-Aspartic acid (ATD) triad in the DIII-DIV linker, upon application of any toxin studied here, is locked in an intermediate position and cannot complete the fast inactivation cycle. Docking provided various sets of residues affected by formation of sea anemone toxins and sodium ion channel complex (Table S1 in SI of RRCS). One may expect that mutations in these sites will affect functioning of NavPaS. In several cases, there is a reasonable correspondence between our predicted "hot spots" and earlier mutagenesis based experimental studies [11]. The lack of full agreement is justified by expected heterogeneity in anemone toxin binding modes in physiological conditions. Due to the overall high similarity of human and NavPaS sodium channel structures, the analogous critical regions in the human proteins may be now identified. Such data should facilitate tracking genetic effects in channelopathies.

Supplementary Materials: The following are available online, Figure S1: Multiple sequence alignment of investigated anemones toxins: Av1, Av2, Av3 and CgNa, Figure S2: Contributions of toxins residues to the binding energy to NavPaS, Figure S3: Binding mode of Av3 alternative pose–Av3' in the NavPaS site 3 region, Figure S4: Multiple sequence alignment of DI/SS2-S6 region of selected arthropod voltage-gated sodium (Nav) channels, Figure S5: Representations of Av3 toxin binding modes to the site 3 of NavPaS channel H392X mutant variants, Table S1a: Residue-Residue Contact Score (RRCS) values for possible toxin-NavPaS channel (amino acid residues) contacts, Table S1b: Residue-Residue Contact Score (RRCS) values for possible toxin-NavPaS channel NAG contacts, Table S2: Parameters characterizing interactions of Av3 anemone toxin with NavPaS channel wild type (WT) and H392X mutant variants, Table S3: Residue (# H392X NavPaS)-residue (#Av3 toxin) interactions responsible for anemone toxin binding to NavPaS mutant variants channel, Table S4a: Residue-Residue Contact Score values for possible Av3 toxin-NavPaS channel H392X variants (amino acid residues) contacts, Table S4b: Residue-Residue Contact Score values for possible toxin-NavPaS

channel NAG contacts, Table S5: Values of SMINA Scoring Function (kcal/mol) for anemones toxins binding to NavPaS channel variants (the lowest energy poses of 5 repetitions up to 100 poses).

Author Contributions: Conceptualization, M.S. and W.N.; methodology, ALL; software, B.N.; validation, ALL; investigation, B.N., M.J., M.S.; resources, M.S., W.N., D.G., L.B.; writing—original draft preparation, B.N., M.J., M.S., W.N.; writing—review and editing, ALL; visualization, B.N., M.J.; supervision, M.S., W.N. All authors have read and agreed to the published version of the manuscript.

Funding: This research was funded by POWER program "Academia Copernicana"-project number POWR.03.05.00-00-Z302/17 (B.N.), Excellence Initiative –Research University" N. Copernicus University in Torun (Poland) Program grants MEMO-BIT# (WN) & Emerging Field: New insight into chronic diseases (M.S., M.J.).

Institutional Review Board Statement: According to Polish Law experiments on insects can be performed without approval of the Ethics Committee. The Ethics Committee in Poland operates on the basis of the "Law of 15 January 2015 on the protection of animals used for scientific or educational purposes" (Journal of Laws of 2015, item 266). This Law is based on the DIRECTIVE 2010/63/EU OF THE EUROPEAN PARLIAMENT AND OF THE COUNCIL of 22 September 2010 on the protection of animals used for scientific purposes (Text with EEA relevance)-20.10.2010 Official Journal of the European Union L 276/33. Insects are not included in these documents.

Informed Consent Statement: Not applicable.

Data Availability Statement: The data presented in this study are openly available in FigShare https://doi.org/10.6084/m9.figshare.14128502.v1, accessed date 27 February 2021.

Acknowledgments: Authors thank Ms Jagoda Kaczorek, MSc for collecting some electrophysiology data at the early stage of this project. Calculations were carried out at the Academic Computer Centre in Gdańsk. Facilities of ICNT UMK, Toruń (Poland) are acknowledged. We thankfully acknowledge the support of Pharis Peptide Research Group (Head: Wolf-Georg Forssmann) for the contribution of L. Béress, Hannover Medical School, Department of Internal Medicine, Clinic of Immunology (Director T. Witte) Division of Experimental and Clinical Peptide Research (Head: Wolf-Georg Forssmann).

Conflicts of Interest: The authors declare no conflict of interest. The funders had no role in the design of the study; in the collection, analyses, or interpretation of data; in the writing of the manuscript, or in the decision to publish the results.

Sample Availability: Docked anemone toxin structures are available from the authors upon a reasonable request.

References

1. Catterall, W.A.; Wisedchaisri, G.; Zheng, N. The conformational cycle of a prototypical voltage-gated sodium channel. *Nat. Chem. Biol.* **2020**, *16*, 1314–1320. [CrossRef] [PubMed]
2. Armstrong, C.M. Na channel inactivation from open and closed states. *Proc. Natl. Acad. Sci. USA* **2006**, *103*, 17991–17996. [CrossRef]
3. Vassilev, P.M.; Scheuer, T.; Catterall, W.A. Identification of an intracellular peptide segment involved in sodium channel inactivation. *Science* **1988**, *241*, 1658–1661. [CrossRef]
4. Huang, W.; Liu, M.; Yan, S.F.; Yan, N. Structure-based assessment of disease-related mutations in human voltage-gated sodium channels. *Protein Cell* **2017**, *8*, 401–438. [CrossRef]
5. Ryan, D.P.; Ptáček, L.J. Episodic Neurological Channelopathies. *Neuron* **2010**, *68*, 282–292. [CrossRef]
6. Kasimova, M.; Granata, D.; Carnevale, V. Voltage-gated sodium channels: Evolutionary history and distinctive sequence features. In *Current Topics in Membranes*; Academic Press: Cambridge, MA, USA, 2016; Volume 78, pp. 261–286. [CrossRef]
7. Gordon, D.; Karbat, I.; Ilan, N.; Cohen, L.; Kahn, R.; Gilles, N.; Dong, K.; Stühmer, W.; Tytgat, J.; Gurevitz, M. The differential preference of scorpion α-toxins for insect or mammalian sodium channels: Implications for improved insect control. *Toxicon* **2007**, *49*, 452–472. [CrossRef] [PubMed]
8. Bosmans, F.; Tytgat, J. Animal peptides targeting voltage-activated sodium channels. *Curr. Pharm. Des.* **2008**, *14*, 2492–2502. [CrossRef]
9. Zhu, S.; Gao, B.; Peigneur, S.; Tytgat, J. How a scorpion toxin selectively captures a prey sodium channel: The molecular and evolutionary basis uncovered. *Mol. Biol. Evol.* **2020**, *37*, 3149–3164. [CrossRef] [PubMed]
10. Nicholson, G.M.; Little, M.J.; Birinyi-Strachan, L.C. Structure and function of δ-atracotoxins: Lethal neurotoxins targeting the voltage-gated sodium channel. *Toxicon* **2004**, *43*, 587–599. [CrossRef]

11. Moran, Y.; Gordon, D.; Gurevitz, M. Sea anemone toxins affecting voltage-gated sodium channels–molecular and evolutionary features. *Toxicon* **2009**, *54*, 1089–1101. [CrossRef] [PubMed]
12. Leipold, E.; Hansel, A.; Olivera, B.M.; Terlau, H.; Heinemann, S.H. Molecular interaction of δ-conotoxins with voltage-gated sodium channels. *FEBS Lett.* **2005**, *579*, 3881–3884. [CrossRef]
13. Gilchrist, J.; Olivera, B.M.; Bosmans, F. Animal toxins influence voltage-gated sodium channel function. In *Handbook of Experimental Pharmacology*; Springer International Publishing: Berlin/Heidelberg, Germany, 2014; Volume 221, pp. 203–229. [CrossRef]
14. Cardoso, F.C.; Lewis, R.J. Sodium channels and pain: From toxins to therapies. *Br. J. Pharmacol.* **2018**, *175*, 2138–2157. [CrossRef]
15. Shen, H.; Li, Z.; Jiang, Y.; Pan, X.; Wu, J.; Cristofori-Armstrong, B.; Smith, J.J.; Chin, Y.K.Y.; Lei, J.; Zhou, Q.; et al. Structural basis for the modulation of voltage-gated sodium channels by animal toxins. *Science* **2018**, *362*, eaau2596. [CrossRef]
16. Cardoso, F.C. Multi-targeting sodium and calcium channels using venom peptides for the treatment of complex ion channels-related diseases. *Biochem. Pharmacol.* **2020**, 114107. [CrossRef] [PubMed]
17. Jankowska, M.; Lapied, B.; Jankowski, W.; Stankiewicz, M. The unusual action of essential oil component, menthol, in potentiating the effect of the carbamate insecticide, bendiocarb. *Pestic. Biochem. Physiol.* **2019**, *158*, 101–111. [CrossRef]
18. Pelhate, M.; Laufer, J.; Pichon, Y.; Zlotkin, E. Effects of several sea anemone and scorpion toxins on excitability and ionic currents in the giant axon of the cockroach. *J. Physiol.* **1984**, *79*, 309–317.
19. Koes, D.R.; Baumgartner, M.P.; Camacho, C.J. Lessons learned in empirical scoring with smina from the CSAR 2011 bench-marking exercise. *J. Chem. Inf. Model.* **2013**, *53*, 1893–1904. [CrossRef]
20. Baker, N.A.; Sept, D.; Joseph, S.; Holst, M.J.; McCammon, J.A. Electrostatics of nanosystems: Application to microtubules and the ribosome. *Proc. Natl. Acad. Sci. USA* **2001**, *98*, 10037–10041. [CrossRef]
21. Humphrey, W.; Dalke, A.; Schulten, K. VMD: Visual molecular dynamics. *J. Mol. Graph.* **1996**, *14*, 33–38. [CrossRef]
22. Venkatakrishnan, A.; Fonseca, R.; Ma, A.K.; Hollingsworth, S.A.; Chemparathy, A.; Hilger, D.; Dror, R.O. Uncovering patterns of atomic interactions in static and dynamic structures of proteins. *bioRxiv* **2019**, 840694. [CrossRef]
23. Zhou, Q.; Yang, D.; Wu, M.; Guo, Y.; Guo, W.; Zhong, L.; Cai, X.; Dai, A.; Jang, W.; I Shakhnovich, E.; et al. Common activation mechanism of class A GPCRs. *eLife* **2019**, *8*, 50279. [CrossRef] [PubMed]
24. Moran, Y.; Kahn, R.; Cohen, L.; Gur, M.; Karbat, I.; Gordon, D.; Gurevitz, M. Molecular analysis of the sea anemone toxin Av3 reveals selectivity to insects and demonstrates the heterogeneity of receptor site-3 on voltage-gated Na+ channels. *Biochem. J.* **2007**, *406*, 41–48. [CrossRef]
25. Barzilai, M.G.; Kahn, R.; Regev, N.; Gordon, D.; Moran, Y.; Gurevitz, M. The specificity of Av3 sea anemone toxin for arthropods is determined at linker DI/SS2–S6 in the pore module of target sodium channels. *Biochem. J.* **2014**, *463*, 271–277. [CrossRef] [PubMed]
26. Rogers, J.C.; Qu, Y.; Tanada, T.N.; Scheuer, T.; Catterall, W.A. Molecular determinants of high affinity binding of α-scorpion toxin and sea anemone toxin in the S3-S4 extracellular loop in domain IV of the Na^+ channel α subunit. *J. Biol. Chem.* **1996**, *271*, 15950–15962. [CrossRef]
27. Shen, H.; Zhou, Q.; Pan, X.; Li, Z.; Wu, J.; Yan, N. Structure of a eukaryotic voltage-gated sodium channel at near-atomic resolution. *Science* **2017**, *355*, eaal4326. [CrossRef]
28. Yan, Z.; Zhou, Q.; Wang, L.; Wu, J.; Zhao, Y.; Huang, G.; Peng, W.; Shen, H.; Lei, J.; Yan, N. Structure of the Nav1. 4-β1 complex from electric eel. *Cell* **2017**, *170*, 470–482.e11. [CrossRef]
29. Madio, B.; King, G.F.; Undheim, E.A.B. Sea anemone toxins: A structural overview. *Mar. Drugs* **2019**, *17*, 325. [CrossRef]
30. Béress, L. Biologically active compounds from coelenterates. *Pure Appl. Chem.* **1982**, *54*, 1981–1994. [CrossRef]
31. Norton, R.S. Structures of sea anemone toxins. *Toxicon* **2009**, *54*, 1075–1088. [CrossRef] [PubMed]
32. Billen, B.; Debaveye, S.; Béress, L.; Garateix, A.; Tytgat, J. Phyla- and subtype-selectivity of CgNa, a Na^+ channel toxin from the venom of the giant caribbean sea anemone *Condylactis Gigantea*. *Front. Pharmacol.* **2010**, *1*, 133. [CrossRef]
33. Manoleras, N.; Norton, R.S. Three-dimensional structure in solution of neurotoxin III from the sea anemone *Anemonia sulcata*. *Biochemistry* **1994**, *33*, 11051–11061. [CrossRef]
34. Rathmayer, W.; Béress, L. The effect of toxins from *Anemonia sulcata* (Coelenterata) on neuromuscular transmission and nerve action potentials in the crayfish (*Astacus leptodactylus*). *J. Comp. Physiol. A* **1976**, *109*, 373–382. [CrossRef]
35. Ravens, U.; Schöllhorn, E. The effects of a toxin (ATX II) from the sea anemone *Anemonia sulcata* on the electrical and mechanical activity of the denervated hemidiaphragm of the rat. *Toxicon* **1983**, *21*, 131–142. [CrossRef]
36. Kudo, Y.; Shibata, S. The potent excitatory effect of a novel polypeptide, anthopleurin-B, isolated from a sea anemone (*Anthopleura xanthogrammica*) on the frog spinal cord. *J. Pharmacol. Exp. Ther.* **1980**, *214*, 443–448.
37. Gordon, D.; Zlotkin, E. Binding of an α scorpion toxin to insect sodium channels is not dependent on membrane potential. *FEBS Lett.* **1993**, *315*, 125–128. [CrossRef]
38. Moran, Y.; Cohen, L.; Kahn, R.; Karbat, I.; Gordon, D.; Gurevitz, M. Expression and mutagenesis of the sea anemone toxin Av2 reveals key amino acid residues important for activity on voltage-gated sodium channels. *Biochemistry* **2006**, *45*, 8864–8873. [CrossRef]
39. Chahine, M.; Plante, E.; Kallen, R. Sea anemone toxin (ATX II) modulation of heart and skeletal muscle sodium channel α-subunits expressed in tsA201 cells. *J. Membr. Biol.* **1996**, *152*, 39–48. [CrossRef]

40. Castillo, C.; Piernavieja, C.; Recio-Pinto, E. Interactions between anemone toxin II and veratridine on single neuronal sodium channels. *Brain Res.* **1996**, *733*, 243–252. [CrossRef]
41. Wanke, E.; Zaharenko, A.J.; Redaelli, E.; Schiavon, E. Actions of sea anemone type 1 neurotoxins on voltage-gated sodium channel isoforms. *Toxicon* **2009**, *54*, 1102–1111. [CrossRef] [PubMed]
42. Hartung, K.; Rathmayer, W. *Anemonia sulcata* toxins modify activation and inactivation of Na^+ currents in a crayfish neurone. *Pflügers Arch. Eur. J. Physiol.* **1985**, *404*, 119–125. [CrossRef]
43. Oliveira, J.S.; Redaelli, E.; Zaharenko, A.J.; Cassulini, R.R.; Konno, K.; Pimenta, D.C.; Freitas, J.C.; Clare, J.J.; Wanke, E. Binding specificity of sea anemone toxins to Nav 1.1-1.6 sodium channels. *J. Biol. Chem.* **2004**, *279*, 33323–33335. [CrossRef] [PubMed]
44. Abd-Ella, A.; Stankiewicz, M.; Mikulska, K.; Nowak, W.; Pennetier, C.; Goulu, M.; Fruchart-Gaillard, C.; Licznar, P.; Apaire-Marchais, V.; List, O.; et al. The repellent DEET potentiates carbamate effects via insect muscarinic receptor interactions: An alternative strategy to control insect vector-borne diseases. *PLoS ONE* **2015**, *10*, e0126406. [CrossRef]
45. Moreau, E.; Mikulska-Ruminska, K.; Goulu, M.; Perrier, S.; Deshayes, C.; Stankiewicz, M.; Apaire-Marchais, V.; Nowak, W.; Lapied, B. Orthosteric muscarinic receptor activation by the insect repellent IR3535 opens new prospects in insecticide-based vector control. *Sci. Rep.* **2020**, *10*, 1–15. [CrossRef] [PubMed]
46. Kalina, R.S.; Peigneur, S.; Zelepuga, E.A.; Dmitrenok, P.S.; Kvetkina, A.N.; Kim, N.Y.; Leychenko, E.V.; Tytgat, J.; Kozlovskaya, E.P.; Monastyrnaya, M.M.; et al. New insights into the type II toxins from the sea anemone *Heteractis crispa*. *Toxins* **2020**, *12*, 44. [CrossRef] [PubMed]
47. Chakrabarti, N.; Ing, C.; Payandeh, J.; Zheng, N.; Catterall, W.A.; Pomès, R. Catalysis of Na+ permeation in the bacterial sodium channel NaVAb. *Proc. Natl. Acad. Sci. USA* **2013**, *110*, 11331–11336. [CrossRef]
48. Flood, E.; Boiteux, C.; Lev, B.; Vorobyov, I.; Allen, T.W. Atomistic simulations of membrane ion channel conduction, gating, and modulation. *Chem. Rev.* **2019**, *119*, 7737–7832. [CrossRef] [PubMed]
49. Vargas, E.; Yarov-Yarovoy, V.; Khalili-Araghi, F.; Catterall, W.A.; Klein, M.L.; Tarek, M.; Roux, B. An emerging consensus on voltage-dependent gating from computational modeling and molecular dynamics simulations. *J. Gen. Physiol.* **2012**, *140*, 587–594. [CrossRef] [PubMed]
50. Demarco, K.R.; Bekker, S.; Vorobyov, I. Challenges and advances in atomistic simulations of potassium and sodium ion channel gating and permeation. *J. Physiol.* **2019**, *597*, 679–698. [CrossRef]
51. Zhang, J.; Mao, W.; Ren, Y.; Sun, R.-N.; Yan, N.; Gong, H. Simulating the ion permeation and ion selection for a eukaryotic voltage-gated sodium channel NaVPaS. *Protein Cell* **2018**, *9*, 580–585.
52. Khera, P.K.; Blumenthal, K.M. Importance of highly conserved anionic residues and electrostatic interactions in the activity and structure of the cardiotonic polypeptide Anthopleurin B. *Biochemistry* **1996**, *35*, 3503–3507. [CrossRef] [PubMed]
53. Gur, M.; Kahn, R.; Karbat, I.; Regev, N.; Wang, J.; Catterall, W.A.; Gordon, D.; Gurevitz, M. Elucidation of the molecular basis of selective recognition uncovers the interaction site for the core domain of scorpion α-toxins on sodium channels*. *J. Biol. Chem.* **2011**, *286*, 35209–35217. [CrossRef]
54. Leipold, E.; Lu, S.; Gordon, D.; Hansel, A.; Heinemann, S.H. Combinatorial interaction of scorpion toxins Lqh-2, Lqh-3, and LqhαIT with sodium channel receptor sites-3. *Mol. Pharmacol.* **2004**, *65*, 685–691. [CrossRef] [PubMed]
55. Rowe, A.H.; Xiao, Y.; Scales, J.; Linse, K.D.; Rowe, M.P.; Cummins, T.R.; Zakon, H.H. Isolation and characterization of CvIV4: A pain inducing α- scorpion toxin. *PLoS ONE* **2011**, *6*, e23520. [CrossRef]
56. Xiao, Y. The tarantula toxins ProTx-II and huwentoxin-IV differentially interact with human Nav1.7 voltage sensors to inhibit channel activation and inactivation. *Mol. Pharmacol.* **2010**, *78*, 1124–1134. [CrossRef]
57. Bosmans, F.; Tytgat, J. Sea anemone venom as a source of insecticidal peptides acting on voltage-gated Na^+ channels. *Toxicon* **2007**, *49*, 550–560. [CrossRef] [PubMed]
58. Clairfeuille, T.; Cloake, A.; Infield, D.T.; Llongueras, J.P.; Arthur, C.P.; Li, Z.R.; Jian, Y.; Martin-Eauclaire, M.-F.; Bougis, P.E.; Ciferri, C.; et al. Structural basis of α-scorpion toxin action on Nav channels. *Science* **2019**, *363*, eaav8573. [CrossRef]
59. Lauc, G.; Krištić, J.; Zoldoš, V. Glycans–the third revolution in evolution. *Front. Genet.* **2014**, *5*, 145. [CrossRef]
60. Baycin-Hizal, D.; Gottschalk, A.; Jacobson, E.; Mai, S.; Wolozny, D.; Zhang, H.; Krag, S.S.; Betenbaugh, M.J. Physiologic and pathophysiologic consequences of altered sialylation and glycosylation on ion channel function. *Biochem. Biophys. Res. Commun.* **2014**, *453*, 243–253. [CrossRef] [PubMed]
61. Béress, L.; Béress, R.; Wunderer, G. Purification of three polypeptides with neuro and cardiotoxic activity from the sea anemone Anemonia sulcata. *Toxicon* **1975**, *13*, 359–368. [CrossRef]
62. Ständker, L.; Béress, L.; Garateix, A.; Christ, T.; Ravens, U.; Salceda, E.; Soto, E.; John, H.; Forssmann, W.-G.; Aneiros, A. A new toxin from the sea anemone *Condylactis gigantea* with effect on sodium channel inactivation. *Toxicon* **2006**, *48*, 211–220. [CrossRef] [PubMed]
63. Trott, O.; Olson, A.J. AutoDock Vina: Improving the speed and accuracy of docking with a new scoring function, efficient optimization, and multithreading. *J. Comput. Chem.* **2010**, *31*, 455–461. [CrossRef] [PubMed]
64. Waterhouse, A.; Bertoni, M.; Bienert, S.; Studer, G.; Tauriello, G.; Gumienny, R.; Heer, F.T.; de Beer, T.A.P.; Rempfer, C.; Bordoli, L.; et al. SWISS-MODEL: Homology modelling of protein structures and complexes. *Nucleic Acids Res.* **2018**, *46*, W296–W303. [CrossRef]

65. Jo, S.; Kim, T.; Iyer, V.G.; Im, W. CHARMM-GUI: A web-based graphical user interface for CHARMM. *J. Comput. Chem.* **2008**, *29*, 1859–1865. [CrossRef] [PubMed]
66. Krissinel, E.; Henrick, K. Inference of macromolecular assemblies from crystalline state. *J. Mol. Biol.* **2007**, *372*, 774–797. [CrossRef] [PubMed]
67. Dolinsky, T.J.; Nielsen, J.E.; McCammon, J.A.; Baker, N.A. PDB2PQR: An automated pipeline for the setup of Poisson-Boltzmann electrostatics calculations. *Nucleic Acids Res.* **2004**, *32*, W665–W667. [CrossRef]

10. Article III

Toward overcoming pyrethroid resistance in mosquito control: the role of sodium channel blocker insecticides

Toward overcoming pyrethroid resistance in mosquito control: the role of sodium channel blocker insecticides

Beata Niklas [1], Jakub Rydzewski [1], Bruno Lapied [2] and Wieslaw Nowak [1],*

[1] Institute of Physics, Faculty of Physics, Astronomy and Informatics, Nicolaus Copernicus University, Grudziadzka 5, 87-100 Torun, Poland;
[2] University Angers, INRAE, SIFCIR, SFR QUASAV, F-49045 Angers, France
* E-mail: wiesiek@umk.pl

ABSTRACT

Diseases spread by mosquitoes lead to death of 700,000 people each year. The main way to reduce transmission is vector control by biting prevention with chemicals. However, the most commonly used insecticides lose efficacy due to the growing resistance. Voltage-gated sodium channels (VGSCs), membrane proteins responsible for the depolarizing phase of an action potential, are targeted by a broad range of neurotoxins, including pyrethroids and sodium channel blocker insecticides (SCBIs). Reduced sensitivity of the target protein due to the point mutations threatened malaria control with pyrethroids. Although SCBIs – indoxacarb (a pre-insecticide bioactivated to DCJW in insects) and metaflumizone – are used in agriculture only, they emerge as promising candidates in mosquito control. Therefore, a thorough understanding of molecular mechanisms of SCBIs action is urgently needed to break the resistance and stop disease transmission. In this study, by performing an extensive combination of equilibrium and enhanced sampling molecular dynamics simulations (3.2 µs in total), we found the DIII-DIV fenestration to be the most probable entry route of DCJW to the central cavity of mosquito VGSC. Our study revealed that F1852 is crucial in limiting SCBI access to their binding site. Result explain the role of the F1852T mutation found in resistant insects and the increased toxicity of DCJW compared to its bulkier parent compound, indoxacarb. We also delineated residues that contribute to both SCBIs and non-ester pyrethroid etofenprox binding and thus could be involved in the target site cross-resistance.

Key words: voltage-gated sodium channel, insecticide, mosquito, fenestration

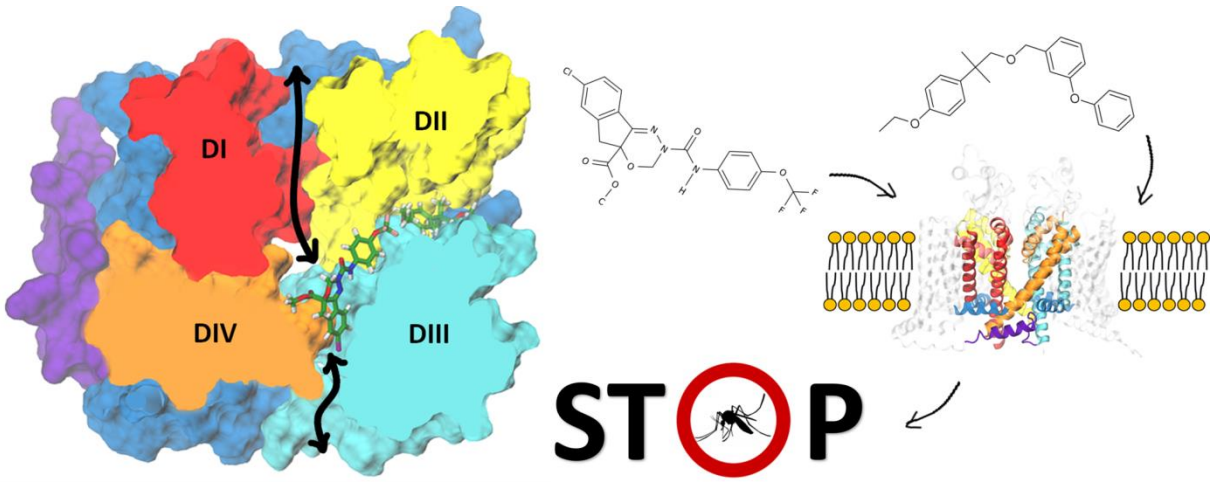

1. INTRODUCTION

The World Health Organization (WHO) warns that more than half of the human population is currently at risk of mosquito-borne diseases. It is predicted that progressive climate change will increase the extent of outbreaks [1, 2]. Malaria is a life-threatening disease caused by *Plasmodium* parasites transmitted to people through the bites of infected female *Anopheles* mosquitoes. In 2021, an estimated 247 million malaria cases led to approximately 619 000 deaths, with a tremendous toll on children under 5 years old (WHO, World Malaria Report 2022).

The primary way to reduce transmission is biting prevention with chemicals. Vector control relies heavily on insecticides and thus can be compromised by resistance [3, 4]. Resistance to pyrethroids, the only insecticide class integrated into bed nets, is widespread globally [5]. To find new ways to control insect populations, a thorough understanding of molecular mechanisms of insecticide action and resistance is required.

The voltage-gated sodium channels (VGSCs) represent one of the major molecular targets of insecticide action. These multi-domain transmembrane proteins are responsible for the depolarizing phase of action potentials in nerves and muscles [6]. While nine subtypes of VGSCs are expressed in humans (hNav1.1-hNav1.9), a single copy of gene coding a sodium channel protein (~2,050 amino acids) can be found in most insects [7, 8]. The α-subunit comprises four homologous domains (DI-DIV) including six transmembrane helices (S1-S6) each (Figure 1a). Helices S1-S4 constitute the voltage-sensing domain (VSD) with a positively charged S4 helix acting as a voltage sensor, while helices S5 and S6 linked by membrane-reentrant pore loop (P-loop) contribute to the ion-conducting pore domain (PD). Due to the crucial role of VGSCs in regulating neuronal membrane excitability, they are targeted by a broad range of naturally occurring and synthetic neurotoxins that alter sodium conductance by blocking the ion-conducting pore or altering gating (opening and closing of a channel) [9]. Some of them – DDT, pyrethroids, and sodium channel blocker insecticides (SCBIs) – are known for their insecticidal activity [10].

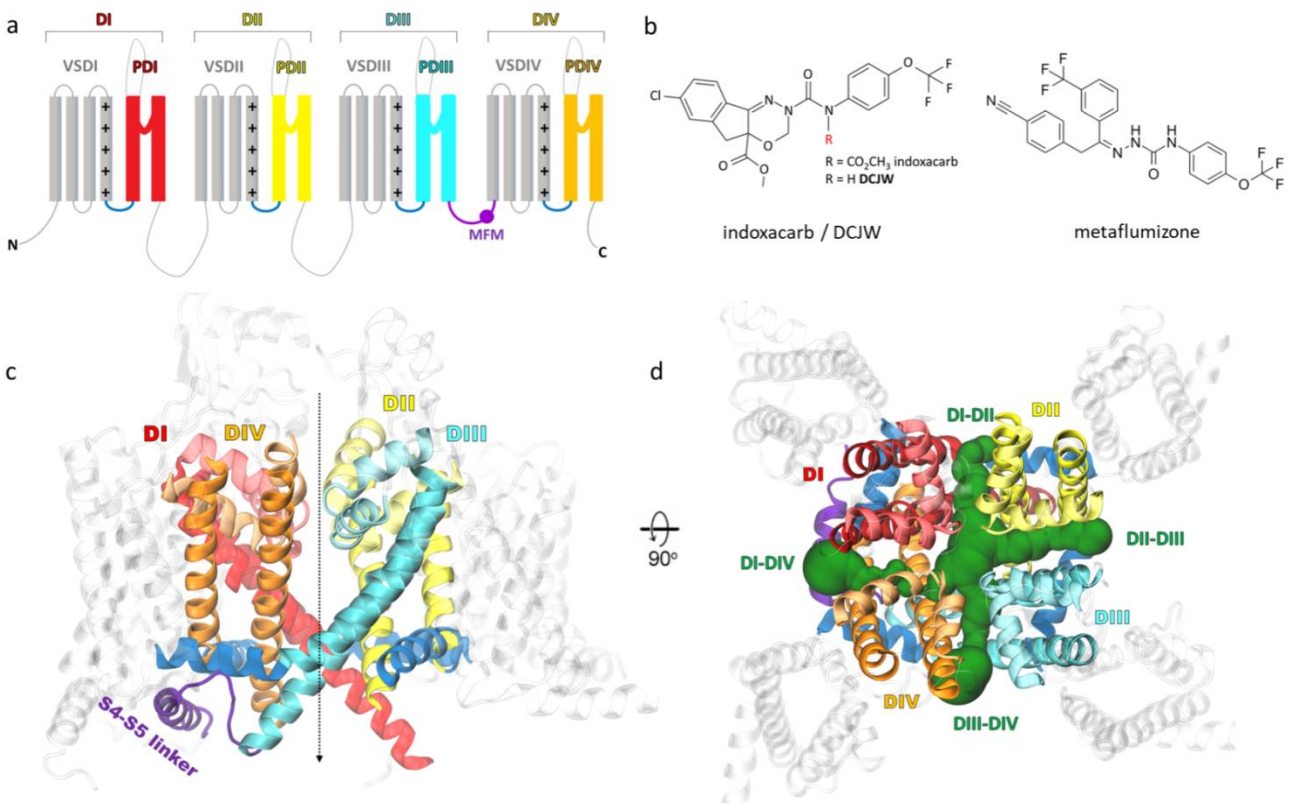

Figure 1. a) Topology of the pseudotetrameric α-subunit of the mosquito *Anopheles gambiae* voltage-gated sodium channel shows four domains consisting of six transmembrane helices each (S1-S6). Helices 1-4 contribute to the voltage-sensor domain (VSD, grey), with a positively charged S4 helix acting as a voltage sensor, and helices S5-S6 create the pore domain (PD). The S4-S5 linkers are shown in dark blue. The inactivation gate MFM motif, as a part of the DIII-DIV linker, is marked in violet. b) Structures of sodium channel blocker insecticides: indoxacarb/DCJW (left) and metaflumizone (right). c) Homology model of the mosquito channel based on the inactivated-state structure of the hNav1.7 channel (PDB code: 6J8G [11]). The approximate location of the pore is indicated by the dashed line. d) The side (left) and top (right) view of the channel with the four lateral fenestrations found by MOLE shown in green.

The extensive use of pyrethroids for the last 50 years has led to the development of knockdown resistance (kdr) in insects worldwide. Over 50 mutations that reduce neuronal sensitivity to DDT and pyrethroids were reported in the α-subunit of VGSC in arthropod species [8]. Due to the reduced sensitivity of target protein by point mutation and/or metabolic resistance (i.e., overexpression of detoxifying enzymes), the effectiveness of long-lasting insecticidal nets and indoor residual spraying treatment of houses with pyrethroid formulations are under threat. No alternative is recommended by WHO Pesticide Evaluation Scheme (WHOPES) for use on mosquito nets. Therefore, there is an urgent need to develop new chemicals for efficient vector control.

SCBIs are relatively new and highly selective insecticides. Two compounds of this group – indoxacarb and metaflumizone – were commercialized [12]. These potent inhibitors of VGSCs have an overlapping binding site with local anesthetics (e.g., lidocaine) [12]. SCBIs preferably bind to and trap VGSC in the slow-inactivated, nonconducting state and block neuronal action potentials in both peripheral and central nervous systems [13, 14].

Indoxacarb (Figure 1b), an oxadiazine SCBI, was developed in 1992 by DuPont by optimizing pyrazoline analogs to limit non-target activity in mammals and other organisms and to increase environmental safety while maintaining insecticidal efficacy [15]. It was registered in 2000 as a reduced-risk compound. In insects, indoxacarb undergoes rapid bioactivation to the more neurotoxic DCJW (N-decarbomethoxyllated JW062) derivative [14], leading to uncoordinated movement, tremors, and pseudoparalysis - a state characterized by violent convulsions in paralyzed insects when disturbed. The differences between mammalian and arthropodic metabolism of indoxacarb partially account for its selectivity towards insects and the consequent widespread usage in agriculture.

Metaflumizone (Figure 1b), a semicarbazone SCBI, was registered to use on Chinese cabbage fields in 2009 as it provides high-efficiency control of the most economically important pests. Formulated with amitraz, metaflumizone controls fleas, ticks, and mites on dogs and cats [16]. It is considered a low-risk chemical to non-target organisms, including pollinators, safe for mammals and the environment [17].

To this date, all the active ingredients used for malaria vector control are spin-offs from agricultural uses [18]. Screening existing registered pesticides provides a rapid route to identifying chemicals of potential value to public health. In the evaluation of 81 commercial agrochemicals for mosquito control, metaflumizone, acetamiprid, thiamethoxan, and thiocyclam were the most promising candidates [18]. Both metaflumizone and indoxacarb were selected in a testing cascade against adult female *Anopheles gambiae* mosquitoes as compounds of high interest as vector control agents [19]. In tunnel tests, indoxacarb induced delayed mortality over 24-96 h against both pyrethroids-sensitive and resistant *An. gambiae*, but there was no protection regarding blood-feeding inhibition [20]. Neither synergism nor antagonism was observed between indoxacarb and pyrethroid [20]. In further tunnel tests and bioassays, indoxacarb was highly effective in both

mortality and reducing the blood feeding by a pyrethroid-susceptible strain of *An. gambiae* and pyrethroid-susceptible and resistant strains of *C. quinquefasciatus* mosquitoes [21]. Mixtures of indoxacarb with pyrethroid alphacypermethrin conferred far greater protection than the single treatments for mortality and blood-feeding inhibition [21]. Thus, the combination of SCBIs and pyrethroids is certainly worth further investigation in terms of both efficacy in vector control and potential cross-resistance. Resistance may involve multiple mechanisms within the insect, e.g., cuticular permeability, metabolic degradation, behavioral resistance or point mutation in the target protein [22]. Although SCBIs and pyrethroids bind to distinct sites on VGSC, mutagenesis data suggest that their binding regions may partially overlap [23]. It is necessary to investigate the role of the target-site in the development of cross-resistance between pyrethroids and SCBIs.

The hydrophobic access pathway for small molecules from the plasma membrane to the center of the ion-conducting pore referred to as the central cavity (CC) of VGSC is *via* four lateral fenestrations (Figure 1d) [24]. These tunnels are delineated by interfaces between the S5 and S6 helices of two adjacent PDs, named DI-DII, DII-DIII, DIII-DIV, and DI-DIV. Multiple structures of eukaryotic VGSC have shown that fenestrations are not symmetrical. Their size changes during the gating cycle and differs across VGSC subtypes [25]. A hypothetical pathway of metaflumizone to the central cavity of VGSC *via* DIII-DIV fenestration was proposed [26]. However, the dynamical modeling of SCBIs' entrance to the central cavity of VGSC was not provided yet. DCJW has a rigid, tricyclic core (Figure 1b), which makes the ligand entrance to the CC of the channel through the fenestration questionable. It is necessary to estimate to what extent fluctuations of the fenestration shape enable the access of SCBIs to modulate VGSC and thus insect physiology.

Ligand-protein association is known to occur on timescales far exceeding the capabilities of equilibrium molecular dynamics (MD) simulations [27, 28]. Therefore, in this study, we perform an extensive combination of equilibrium and enhanced MD simulations of a total aggregate simulation time of 3.2 µs to alleviate the sampling problem [29] and to find the entry route of DCJW to the CC of mosquito VGSC. We investigate the binding interactions of DCJW, metaflumizone, and a non-ester pyrethroid etofenprox within the AgNav1 channel to assess the impact of target site insensitivity conferring resistance to pyrethroids (kdr) on SCBIs action on mosquito channel.

2. RESULTS AND DISCUSSION

2.1 Docking of DCJW and Metaflumizone to the *An. gambiae* VGSC

The binding of SCBIs to the slow-inactivated channel state is favored over the open state not due to the conformation of the VGSC itself but rather due to the very slow kinetics of the channel-ligand association [30]. This is supported by the observation that upon removing slow and fast-inactivation, the block of fast-inactivated and open channels by the pyrazoline RH-1211 proceeds as quickly as the block of slow-inactivated channels [31]. Bearing this in mind, we built three models of mosquito AgNav1 VGSC: open, inactivated, and closed, based on the templates of experimental structures captured in those states [11, 32, 33].

We found that in the lowest energy docking poses in both open- and inactivated-state models, DCJW and metaflumizone extend between the DIII-DIV fenestration, CC, and the entrance to the DII-DIII fenestration from the interior of the channel. The root-mean-square deviation (RMSD) values between the open- and inactivated-state models are 1.7 Å for DCJW and 2.81 Å for metaflumizone. The binding energy of docking to the inactivated model, measured by the smina

scoring function (SSF), equals -9.61 kcal/mol for DCJW and -10.18 kcal/mol for metaflumizone (Figure 2). We found no poses of either DCJW or metaflumizone in the PD of the closed AgNav1 model. However, in their lowest energy poses (SSF=-8.05 kcal/mol for DCJW and -8.42 kcal/mol for metaflumizone), both ligands approach the DIII-DIV fenestration from the plasma membrane; see Figure S1 in the Supporting Information (SI). As the inactivated-state model (Figure 1c,d) reflects the most physiological binding condition, we focus on this model further.

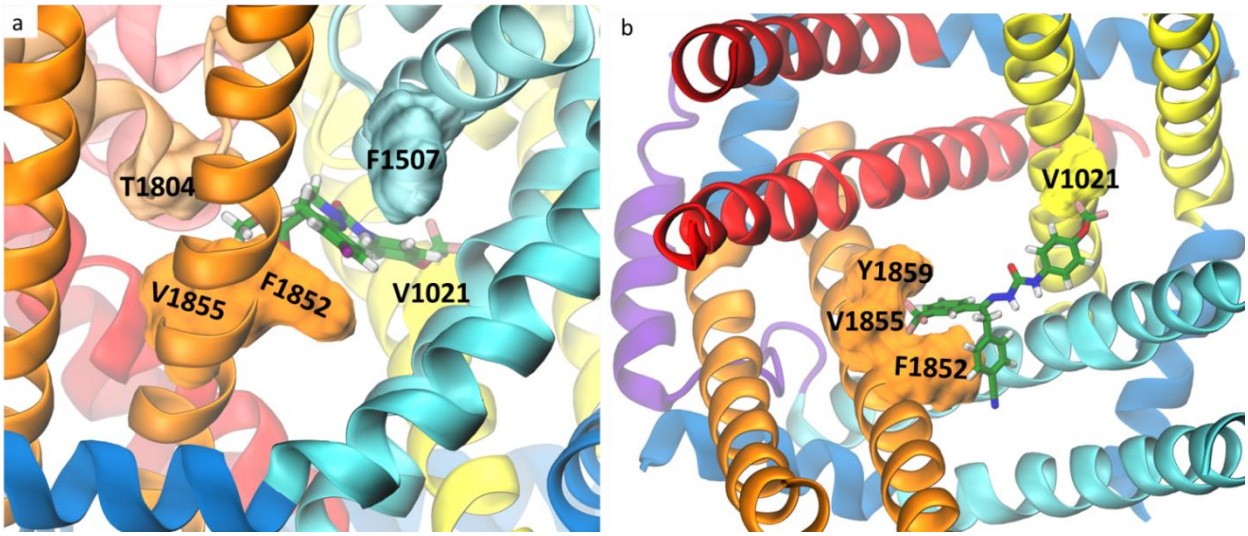

Figure 2. Docking of DCJW (a) and metaflumizone (b) to the mosquito voltage-gated sodium channel (VGSC). Residues known to affect channel sensitivity to these insecticides are shown in a surface representation. Ligands are shown in a stick representation with carbon atoms in green, nitrogen in blue, oxygen in red, fluor in pink, chloride in purple, and hydrogen atoms in white. Side view is presented in (a) and top view with the P-loop removed for clarity in (b). Coloring of the channel helices refers to Figure 1.

A common structural backbone for SCBIs, which may play a key role in their insecticidal activity, consists of two aromatic rings connected by five atoms including three nitrogens and one carbonyl group [34]. In our docking, nitrogen atoms from both ligands form hydrogen bonds with S1552 from the DIII S6 helix, while the carbonyl group faces the channel axis to potentially block the flow of the sodium ions through the pore. The highest contribution to the docking binding energy of both DCJW (21%) and metaflumizone (22%) comes from π-stacking interactions with F1852, which has been found in SCBIs-resistant insects [35, 36]. Further contacts are primarily hydrophobic, and most of them include residues from S6 helices and P-loops from DIII and DIV. Among them, we found F1507, T1555, T1804, V1855, and Y1859, the substitution of which affected SCBIs activity on VGSCs [26, 37, 38]. While the trifluoromethyl group of DCJW approaches but does not penetrate the DII-DIII fenestration, the trifluoromethyl group of metaflumizone is buried in the tunnel. Both ligands interact with V1021 from DII S6, the substitution of which was found to affect the rNav1.4 channel sensitivity to indoxacarb and metaflumizone but not DCJW [39]. To validate this result upon fluctuating channel conformations, we run three 250 ns MD simulations of DCJW-bound AgNav1. In all three MD simulations, DCJW stayed tightly bound and its energy (rescored after the simulations using the docking function SSF) reached -10.96 kcal/mol due to more favorable side chain orientations. We found a hydrogen bond between S1552 and the ligand in >50% of all snapshots. We also observed that the sodium ion and the carbonyl group of DCJW stayed close to each other in all three MD simulations (Figure S2 in the SI). For a list of the channel-DCJW contacts observed in our MD simulations, see the SI Table S1.

2.2 DCJW Binding Pathway to the Central Cavity

As protein tunnels can be transient and heterogeneous, which may lead to spontaneous closing and opening [40, 41], we aimed to find possible entry and exit routes for DCJW using MD simulations instead of analyzing only the static structures of VGSC. To assess fluctuations of the fenestrations and compare their bottleneck radius distributions, we ran three 250 ns unbiased MD simulations of the inactivated-state AgNav1 model. From Figure 3a, we can see that the DI-II and DIII-DIV fenestrations are the widest, with average bottleneck radii of around 2 Å, making them the most accessible and probable entry route for ligands. This result agrees with a similar analysis performed on human Nav1.1, Nav1.2, Nav1.4, Nav1.5, and Nav1.7 inactivated-state VGSCs [25]. Then, we ran 30 enhanced sampling MD simulations in which we biased the positions of DCJW to search for possible channel entry and exit routes. We found that DCJW could migrate outside the channel only through the DI-DII, DII-DIII, and DIII-DIV fenestrations. For the DI-DIV tunnel, we did not observe any dissociation event (i.e., pathways). As the DII-DIII fenestration is less likely to serve as the entry route for DCJW to reach the CC (Figure 3a), we focused our further investigation on the DI-DII and DIII-DIV fenestrations.

As the binding reaction coordinates, we selected DCJW conformations from the shortest trajectories that ended in dissociation along the DI-DII and DIII-DIV fenestrations. Next, we estimated the free-energy profiles by biasing path-collective variables [42], i.e., the progress along (s) and distance from the identified binding reaction coordinates (z) along the DI-DII and DIII-DIV fenestrations, during which DCJW could move between the associated and dissociated states in both directions. For each binding reaction coordinate, we performed a 500 ns well-tempered metadynamics simulation. During these enhanced sampling simulations, we observed many transitions across the path-collective variables, suggesting that the simulations converged.

The free-energy profiles as functions of the progress along the DI-DII and DIII-DIV fenestrations, are shown in Figure 3b. Entering the channel, DCJW encounters a free-energy barrier of about 20 kcal/mol when approaching the DIII-DIV fenestration (Figure 3c) and a barrier higher than 30 kcal/mol in the case of the DI-DII fenestration (Figure 3b). Moreover, while the profile along the DII-DIII tunnel is flat, the ligand can get stuck in the free-energy minimum observed in the middle of the pathway *via* the DI-DII fenestration. Also, as the DCJW binding site is located at the intersection of the CC and the DIII-DIV fenestration, the route *via* this tunnel is shorter when compared to the pathway through DI-DII, which includes traveling through the middle of the ion-conducting pore. These observations suggest that the entry to the CC of VGSC through the DIII-DIV fenestration is preferable. Interestingly, after reaching the CC, the ligand faces a high free-energy barrier of about 30 kcal/mol to unbind, which can be explained by a high affinity of DCJW-channel interactions that stabilize the ligands in its binding site (Figure 3e). The height of free-energy barriers seen along the DCJW pathway in both fenestrations agrees well with the very slow kinetics of pyrazolines entry to the binding site and their inability to block open channels [31].

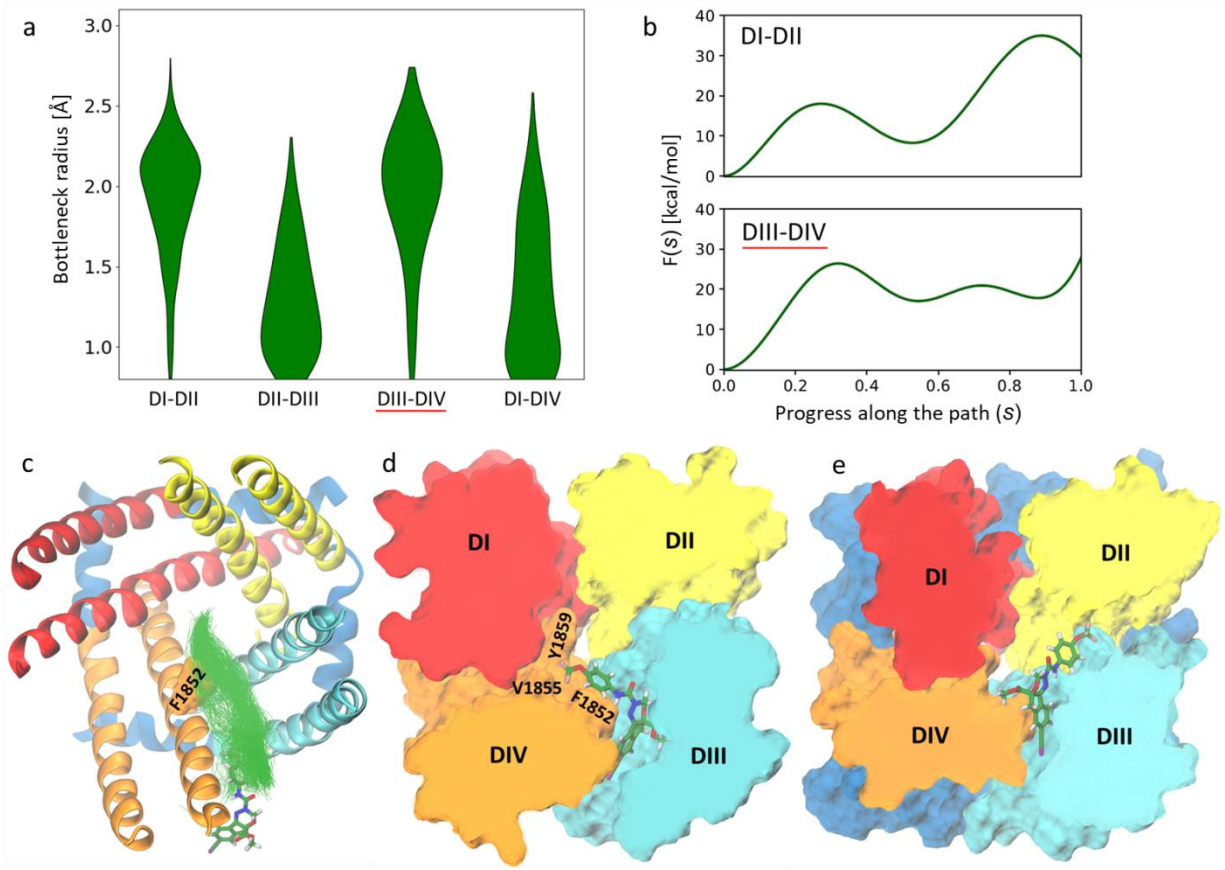

Figure 3. a) The bottleneck radius distributions of the four lateral fenestrations in the inactivated-state model of the mosquito sodium channel calculated using CAVER3.0 [43] based on three 250 ns MD trajectories combined. b) Free energy profiles of DCJW crossing the DI-DII (top) and DIII-DIV (bottom) fenestration. The path starts (0.0) at the DCJW binding site found in docking (shown in e) and ends (1.0) at the channel-membrane interface (indicated by a ligand in sticks representation in c). c) Tunnel clusters found by CAVER in the metadynamics simulations of DCJW crossing the DIII-DIV fenestration are presented as green lines. d) The representative snapshot of the most densely populated cluster of ligand positions along the binding pathway, corresponding to the local energy minimum, where DCJW interacts with Y1852, V1855, and Y1859, known to affect SCBIs' efficacy on VGSCs.

The dynamical variability in the bottleneck radius of fenestration conditionalizes the entry of pore blockers to the CC with the kinking at the midpoint of S6 helices, identified as important in channel gating [44], appearing to be restrictive [25]. In the AgNav1 channel, F1852 is the key hydrophobic residue bottlenecking the DIII-DIV fenestration (Figure 2 and Figure 3c,d). Substitution of the corresponding residue to the F1852 by a bulkier tyrosine had been found in SCBIs-resistant populations of the tomato leafminer and the diamondback moth [35, 36]. The substantial reduction of VGSC sensitivity to indoxacarb due to F1852Y mutation has also been functionally validated by electrophysiological studies in *Xenopus* oocytes [37]. Furthermore, the alanine substitution (F1817A in the cockroach $BgNa_v$) enhanced the ability of both DCJW and metaflumizone to interact with inactivated VGSCs. It also provided an easier escape route for metaflumizone to leave its receptor site during recovery from inactivation [38]. We suggest that the resistance could be explained by the reduced frequency of reaching the binding site due to the higher free-energy barrier of crossing the DIII-DIV fenestration.

Interestingly, in docking of indoxacarb, the proinsecticide that undergoes bioactivation to the more toxic DCJW, we obtained the lowest energy poses in the DIII-DIV fenestration (SI Figure S3). We

postulate that the higher probability of passing the fenestration due to a decrease of the ligand size upon metabolization may partially explain the increased toxicity of DCJW when compared to indoxacarb.

2.3 Comparison of the SCBIs and etofenprox binding region. Implications for the target site cross-resistance with pyrethroids.

Recently, high cross-resistance with deltamethrin, the most important pyrethroid in malaria prevention, was observed in an indoxacarb-resistant population of the fall armyworm, *Spodoptera frugiperda* [45]. Little positive cross-resistance between indoxacarb and pyrethroids was also found in the diamondback moth, *Plutella xylostella* L. [46-48]. Negative cross-resistance observed in fenvalerate- and cypermethrin-selected populations of *Helicoverpa armigera* was explained by the elevated level of carboxyl esterase in pyrethroids-resistant insects, which may increase the enzymatic activation of indoxacarb to more toxic DCJW derivative [49]. It is in agreement with a study on the same species, where high resistance to cypermethrin and deltamethrin but not to the non-ester pyrethroid etofenprox and indoxacarb, was observed together with the positive correlation with esterase activity. The lack of resistance to DDT, which acts on the same site as pyrethroids, excludes the involvement of target site resistance in this population [50]. Contradicting results suggest multiple mechanisms involved in indoxacarb resistance. Clearly, there is a shortage of data describing the involvement of the target-site sensitivity in cross-resistance development.

Etofenprox (Figure 4a) is a pyrethroid derivative with an ether linkage instead of an ester linkage present in traditional pyrethroid insecticides, making it less prone to metabolic degradation by esterases. Experiments performed with heterologous VGSC expression in the *Xenopus* oocyte suggest that etofenprox displays a pyrethroid-like effect [51]. It exhibits comparable toxicity to the *Anopheles* mosquito [52] but is considered less toxic to fish [53]. We have chosen this compound to assess the impact of target site insensitivity conferring resistance to pyrethroids on SCBIs action on VGSCs. Type I pyrethroids are known to modify resting or inactivated channels, while type II pyrethroids preferably bind to the open state of sodium channels [10]. As etofenprox, a non-ester pyrethroid, represents a separate type, we docked this insecticide to both open and inactivated models of mosquito VGSC.

The lowest energy poses in the open and inactivated models overlap but are not identical with the SSF values -9.97 kcal/mol and -9.71 kcal/mol, respectively. Etofenprox penetrates the DII-DIII fenestration deeper than it was proposed before in docking to the prokaryotic NavMs-based model [51, 54]. Deep binding results in interactions with 16 kdr residues (Table 1), accounting for 68% and 60% of the total SSF found for the open and inactivated model, respectively. The highest contribution to the binding energy (-2.0 kcal/mol for the open and -2.42 kcal/mol for inactivated model) comes from F1553, which was found as a key bottlenecking residue in the DII-DIII fenestration [25]. In the inactivated-state model, ligand position is stabilized by parallel π-stacking interactions with F1553 and F1025 (that are both kdr, see Table 1). As both overall binding energy and the contribution from the kdr residues were more negative in docking to the open model, we further refer to this pose, presented in Figure 4c,d.

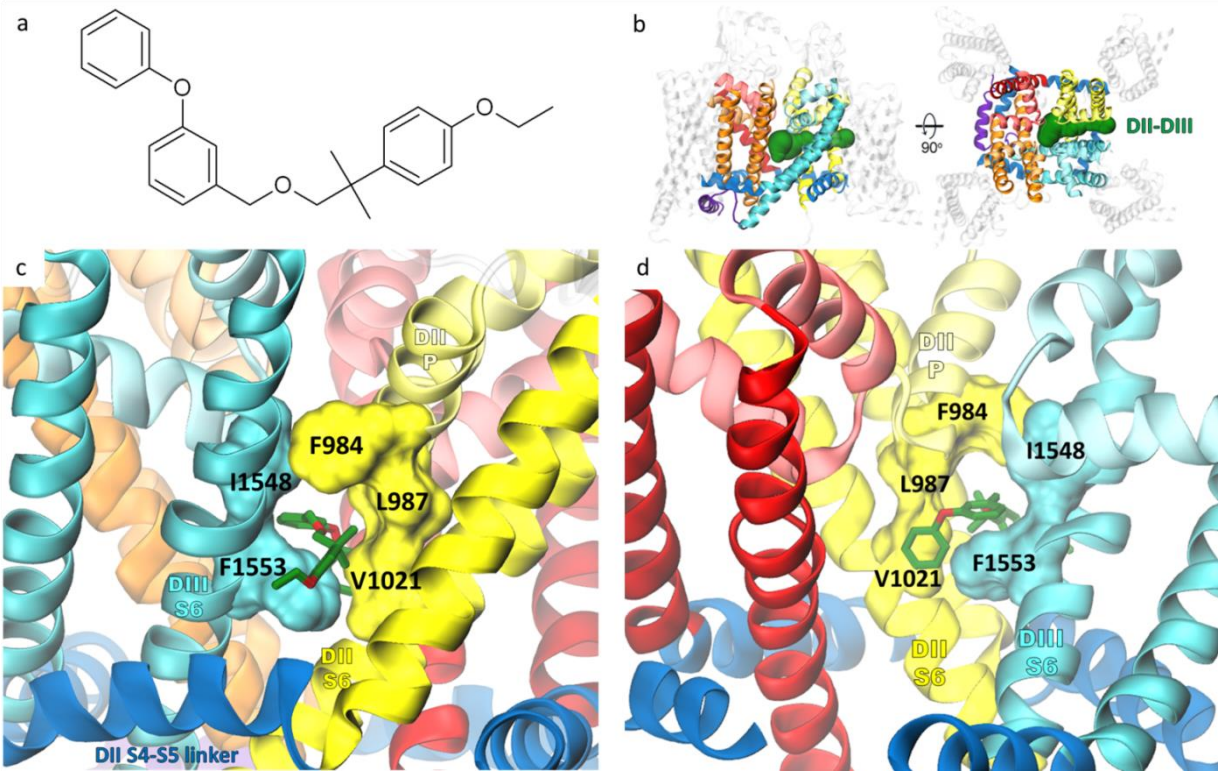

Figure 4. a) Chemical structure of non-ester pyrethroid insecticide etofenprox. b) The DII-DIII fenestration tunnel, found in docking as a ligand binding region, is presented in green in a voltage-gated sodium channel model in a side (left) and a top (right) view. c-d) The lowest energy pose of etofenprox (in green stick representation) bound in the open model. View from the channel/membrane interface is shown in (c), while the fenestration entrance to the central cavity of the channel is visualized in (d), with the PDIII helices removed for clarity. Residues that were found as kdr contributing to both etofenprox and SCBIs binding are shown in a surface representation. The coloring of the channel refers to Figure 1.

We found 10 residues to contribute to etofenprox and both SCBIs binding (Table 1). Additional four are shared in etofenprox and metaflumizone but not in the DCJW docking region. Mutation of five residues participating in the binding of all three insecticides (F984, L987, V1021, I1548, and F1553) are found in pyrethroid-resistant insects. We show them in a surface representation in Figure 4c,d. The contribution to the binding energy from kdr residues is higher for metaflumizone than indoxacarb (24% and 15% of total SSF, respectively).

Table 1. Etofenprox binding region. DCJW and metaflumizone interactions with given residues are marked with D and M, respectively.

VGSC domain	*Anopheles gambiae*	*Musca domestica*	Kdr ref.	Overlap with SCBIs binding region
DII, S4-S5 linker	M923	M918	[55-57]	-
	T926	T921	-	-
	M927	M922	-	-
DII S5	T934	T929	[55, 58]	-
	L937	L932	[59-62]	M
	C938	C933	[55]	-
	I941	I936	[61, 63]	-
DII P	**F984**	**F979**	**[57, 64]**	**D, M**
	L987	**L982**	**[65, 66]**	**D, M**
	C988	C983	-	D, M
DII S6	N1018	N1013	[67]	M
	V1021	**V1016**	**[65, 68-75]**	**D, M**
	L1022	L1017	[76]	M
	L1024	L1019	-	-
	F1025	F1020	[77, 78]	-
DIII P	A1510	A1494	-	D, M
	F1512	F1496	-	D, M
DIII S6	**I1548**	**I1532**	**[75, 79-81]**	**D, M**
	I1549	I1533	[82]	D, M
	F1550	F1534	[74, 75, 83]	-
	S1552	S1536	-	D, M
	F1553	**F1537**	**[82, 84]**	**D, M**
	F1554	F1538	[85, 86]	-
	L1556	L1540	-	D, M

V1021I/G (V1016 in house fly VGSC) is one of the most frequently reported kdr mutations in pyrethroids-resistant insects worldwide. It has been found in disease-spreading *Aedes* mosquitoes in Indonesia [65], Thailand [68, 69], Taiwan [70], Singapore [71], China [72], and Latin America [73]. In mosquitoes, a concomitant S989P+V1016G kdr mutation confers resistance to 17 structurally diverse pyrethroids with the highest level (107 fold) to etofenprox. Cross-resistance to both indoxacarb and DCJW was reported in this study [23]. In *Aedes aegypti* mosquito, the level of resistance to DCJW conferred by the *kdr* allele 410L+1016I+1534C (house fly numbering) was higher than in mosquitoes carrying the 1534C allele alone [87], suggesting the direct role of the V1016I mutation on DCJW action on VGSC. The lysine substitution of the corresponding residue in the rat rNav1.4 channel (V787K) completely abolished mutated VGSC inhibition by metaflumizone [39]. To test the impact of V1021 substitution on SCBI binding, we performed docking to the following VGSC mutants: V1021I, V1021G, and V1021K.

Table 2. The affinity of insecticides to the V1021 substituted VGSC. Binding energy calculated with smina scoring function is shown in kcal/mol.

VGSC	DCJW	metaflumizone	etofenprox
WT	-9.61	-10.16	-9.97
V1021I	≈	-9.96	-9.30
V1021G	-9.38	-9.66	-8.99
V1021K	-9.06	no WT-like poses	-8.30

Substitution of V1021 did not affect DCJW binding significantly – RMSD values for a ligand shifted by 0.16 Å and 1.0 Å for isoleucine and glycine, respectively, which are kdr mutations found in nature. Only the lysine substitution pulled the trifluoromethyl group of DCJW out of the CC entrance to the DII-DIII fenestration (RMSD=2.28 Å), reducing the binding affinity by 0.55 kcal/mol (Table 2). A higher effect was observed for metaflumizone. While isoleucine and glycine substitutions only slightly shifted the ligand positions (RMSD ~1.7 Å), in the V1021K substituted channel WT-like binding poses were not found. Our results are in agreement with the previous mutagenesis study on the rNav1.4 channel, where sensitivity to inhibition by 10 µM metaflumizone was abolished entirely in the rNav1.4/V787K channels, but no significant effect was observed for DCJW [39]. V1021K substitution disabled etofenprox binding deep into the DII-DIII fenestration. In this mutant, we obtained a binding pose similar to that presented before [54], with the SSF reduced by 1.7 kcal/mol when compared to the WT (SI Figure S4).

V1021 clearly contributes to SCBI binding. However, neither the isoleucine nor glycine substitution found in resistant insects affects ligand binding to the extent that could substantially decrease the inhibitory effect on mutated channels. As lysine substitution itself enhances slow inactivation [39], the V1021K mutant should not be expected in insects.

3. CONCLUSIONS

In this work, we found the binding poses of DCJW and metaflumizone located in the CC of mosquito VGSC, where they interact with residues known to affect channel sensitivity to SCBIs. We analyzed the possible pathways of DCJW entrance to its binding site and found the DIII-DIV fenestration to be the most probable route. The phenylalanine at the midpoint of the DIV S6 helix (F1852), mutated to tyrosine in SCBI-resistant insects, bottlenecks the fenestration and play a key role in stabilization of the ligand in its binding site. Based on our docking and metadynamics studies we postulate that the reduced sensitivity to DCJW in resistant insects, and the increased toxicity of DCJW when compared to its bulkier parent compound, indoxacarb, can be explained by the impeded access of the ligands to their binding site in the CC. Furthermore, by docking etofenprox, we delineated residues that contribute to SCBI and pyrethroid binding sites simultaneously and thus could be responsible for target site cross-resistance. Our study is a step towards better understanding the action of SCBIs on insect VGSCs that should facilitate the fight against insect vector-borne diseases.

4. METHODS

4.1 Homology Modeling

The homology models of an α subunit of the *Anopheles gambiae* sodium channel protein AgNav1 in open, inactivated, and closed states were built using the SWISS-MODEL server [88], using rat rNav1.5 (PDB: 7FBS [32]), human hNav1.7 (PDB: 6J8G [11]), and cockroach NavPas (PDB code: 6A90 [33]) crystallographic structures, respectively, as templates. The models were built based on the A5I843_ANOGA amino acid sequence provided by the UniProtKB database [89]. Two long, disordered intracellular loops (ICL1 – 338 residues, ICL2 – 240 residues), not present in any sodium channel protein experimental structures, were removed from each model. The quality of the models was validated using ERRAT [90] and PROCHECK [91]. The protein preparation module of Schrodinger Maestro [92] was used to assign protonation states, add hydrogen atoms, and minimize all three models. 95.7% of the inactivated model residues fall below the 95% rejection limit in the ERRAT analysis. Only 8 residues were found in disallowed regions by PROCHECK, all of them belonging to the intracellular or extracellular loops. Mutations of V1021 were introduced using Schrodinger Maestro, followed by minimization of mutated models.

4.2 Docking

3D structures of all ligands were downloaded from PubChem [93] and minimized using Schrodinger Maestro LigPrep. Molecular docking was performed using the smina package [94], a fork of Autodock Vina [95] that provides enhanced support for minimization and scoring. Ten independent runs (yielding up to 100 poses each) of flexible ligand docking to each model with default parameters were conducted.

4.3 Equilibrium MD Simulations

Inputs for equilibrium MD simulations were generated using the CHARMM-GUI membrane builder [96-98]. To mimic an insect-like membrane, a heterogeneous bilayer model composed of 500 lipid molecules in proportions: 38% DOPE, 18% DOPS, 16% DOPC, 13% POPI, 11% SM (CER180), 3% DOPG, and 1% PALO 16:1 fatty acid was built as proposed for an insect muscarinic GPCR before [99]. Water molecules in the TIP3P model were added above and below the lipids to generate a 20 Å thickness layer further neutralized with Na^+ and Cl^- ions to the concentration of 0.15 M. Six steps of equilibration simulations in the NVT ensemble followed by the NPT ensemble with gradually decreased restraint force constants to various components were run using NAMD 2.13 [100] with the CHARMM36 force field applied. Three independent simulations of 250 ns each were run for the inactivated-state model. Temperature, controlled by the Langevin thermostat, was set to 303.15 K and pressure to 1.01325 bar (1 atm). All MD simulations employed a 2 fs time step.

The MD trajectories were processed into protein-only PDB snapshots saving a frame every 1 ns. DCJW and metaflumizone were docked to each snapshot as described above for the static models, generating up to 750000 poses in total. The lowest energy poses were selected for the starting points of MD simulations of ligand-bound protein. Equilibration followed by 250 ns MD simulations were run as described for the apo protein. Topology and parameters files for DCJW were generated by SwissParam [101]. Results were visualized with the VMD code [102].

4.4 Enhanced Sampling MD Simulations

Enhanced sampling MD simulations were run using the Gromacs 2020.7 software [103] patched with the PLUMED 2.8 plugin [104, 105]. The simulations were run in the NVT ensemble using the stochastic velocity rescaling thermostat [106] at 303.15 K with a relaxation time of 1 ps. Hydrogen bonds were constrained using P-LINCS [107]. The voltage-sensor domains of VGSC were removed and neutral groups were added to cap S4-S5 linkers termini. The system preparation (e.g., equilibration) and the rest of simulation parameters were the same as for equilibrium MD simulations (Section 2.3).

To find possible reaction coordinates for DCJW binding in the fenestrations, we used the maze module of PLUMED [108] and followed the protocol described in Refs. [41, 108]. DCJW was biased to move with a constant velocity of 10 Å/ns with a bias height of 240 kcal/mol. The direction of biasing was found by minimizing a loss function describing contacts between the ligand and VGSC every 1 ns using simulated annealing. The implemented loss function was $Q= \Sigma_{kl}[1+\exp(r_{kl}-r_0)]^{-1}$, where r_{kl} is the distance between the i-th atom of DCJW and the j-th atom of VGSC and r_0 is set to 4 Å. In total, 30 such MD simulations were run. The simulations were terminated when DCJW dissociated from VGSC or the simulation time exceeded 100 ns. The average length of these MD simulations was around 23 ns.

To reconstruct free-energy profiles along the identified reaction coordinates, for each, we ran a 500-ns well-tempered metadynamics simulation [109]. DCJW conformations and VGSC Cα atoms within 8 Å of any atom of DCJW taken from the reaction coordinates were used to define path-collective variables—progress along the reaction coordinate (s) and the distance from the reaction coordinate (z) [42]. To prohibit DCJW from escaping to the membrane, additional constraints for the progress along the reaction coordinate and the distance from the reaction coordinate with force constants equal to 1000 kJ/mol were added. Both path-collective variables were biased using an initial Gaussian height of 2 kJ/mol, a width of 0.12, and a bias factor of 50. Gaussians were deposited every 1 ps, and the time-dependent constant c(t) was updated every 10 Gaussian depositions. The free-energy profiles were reweighted using the Tiwary-Parrinello algorithm [110], taking into account the metadynamics bias potential and the constraints.

4.5 Fenestration Analysis

Fenestration analysis was performed using CAVER 3.0 [43] with default parameters, except for a probe radius of 0.8 Å, shell radius of 15 Å, and shell depth of 15 Å. Three MD trajectories of the inactivated model were processed into a series of PDB snapshots containing pore domain and S4-S5 linkers only, taking a frame every 1 ns. The following residues were used as starting points for tunnel search: Phe416 (S6 DI), Gly1015 (S6 DII), Phe1553 (S6 DIII), and Phe1852 (S6 DIV).

Supporting Information Available

Supporting Information is available free of charge at XXXXXX.

- Docking of DCJW and metaflumizone to the closed-state AgNav1
- DCJW interaction with sodium ion
- DCJW-channel contacts found in MD simulations
- Docking of indoxacarb
- Docking of etofenprox to the V1016K mutant

Acknowledgements

This research was funded by the National Science Centre, Poland, under grants no. 2021/41/N/NZ3/02165 (BN) and Sonata 2021/43/D/ST4/00920 (JR). J.R. acknowledges funding from the Polish Science Foundation (START) and the Ministry of Science and Higher Education in Poland. Simulations were carried out using computing clusters at the Centre of Informatics Tricity Academic Supercomputer & Network and the Interdisciplinary Centre for Mathematical and Computational Modeling (ICM), University of Warsaw, under grant no. GA76-16. Facilities of UMK/ICNT were used during this project. BN, JR, and WN are members of #MEMO-BIT and EF IDUB UMK teams.

Contributions

BN: Conceptualization; Data curation; Formal analysis; Investigation; Methodology; Resources; Software; Validation; Visualization; Writing - original draft
JR: Data curation; Formal analysis; Investigation; Methodology; Software; Validation; Writing - review & editing
BL: Conceptualization; Supervision; Writing - review & editing
WN: Conceptualization; Funding acquisition; Project administration; Resources; Supervision; Validation; Writing - review & editing

Competing interests

Authors declare no competing interests.

References

1. Ryan, S.J., et al., *Global expansion and redistribution of Aedes-borne virus transmission risk with climate change.* PLoS neglected tropical diseases, 2019. **13**(3): p. e0007213.
2. Iwamura, T., A. Guzman-Holst, and K.A. Murray, *Accelerating invasion potential of disease vector Aedes aegypti under climate change.* Nature communications, 2020. **11**(1): p. 2130.
3. Ranson, H., *Current and future prospects for preventing malaria transmission via the use of insecticides.* Cold Spring Harbor perspectives in medicine, 2017. **7**(11): p. a026823.
4. Suh, P.F., et al., *Impact of insecticide resistance on malaria vector competence: a literature review.* Malaria Journal, 2023. **22**(1): p. 1-11.
5. Liu, N., *Insecticide resistance in mosquitoes: impact, mechanisms, and research directions.* Annual review of entomology, 2015. **60**: p. 537-559.
6. Jiang, D., J. Zhang, and Z. Xia, *Structural Advances in Voltage-Gated Sodium Channels.* Frontiers in Pharmacology, 2022. **13**.
7. Scott, J.G., *Life and death at the voltage-sensitive sodium channel: evolution in response to insecticide use.* Annual review of entomology, 2019. **64**: p. 243-257.
8. Dong, K., et al., *Molecular biology of insect sodium channels and pyrethroid resistance.* Insect biochemistry and molecular biology, 2014. **50**: p. 1-17.
9. Catterall, W.A., et al., *Voltage-gated ion channels and gating modifier toxins.* Toxicon, 2007. **49**(2): p. 124-141.
10. Silver, K.S., et al., *Voltage-gated sodium channels as insecticide targets.* Advances in insect physiology, 2014. **46**: p. 389-433.
11. Shen, H., et al., *Structures of human Nav1.7 channel in complex with auxiliary subunits and animal toxins.* Science, 2019. **363**(6433): p. 1303-1308.
12. Silver, K., K. Dong, and B. S Zhorov, *Molecular Mechanism of Action and Selectivity of Sodium Channel Blocker Insecticides.* Current medicinal chemistry, 2017. **24**(27): p. 2912-2924.

13. Silver, K.S., et al., *Mechanism of action of sodium channel blocker insecticides (SCBIs) on insect sodium channels.* Pesticide biochemistry and physiology, 2010. **97**(2): p. 87-92.
14. Wing, K.D., et al., *A novel oxadiazine insecticide is bioactivated in lepidopteran larvae.* Archives of Insect Biochemistry and Physiology: Published in Collaboration with the Entomological Society of America, 1998. **37**(1): p. 91-103.
15. McCann, S.F., et al., *The discovery of indoxacarb: oxadiazines as a new class of pyrazoline-type insecticides.* Pest Management Science: formerly Pesticide Science, 2001. **57**(2): p. 153-164.
16. Rust, M.K., D. Rugg, and D. Rock, *Metaflumizone—a new ectoparasiticide for dogs and cats.* Veterinary Parasitology, 2007. **3**(150): p. 175-176.
17. Hempel, K., et al., *Toxicological properties of metaflumizone.* Veterinary Parasitology, 2007. **150**(3): p. 190-195.
18. Hoppé, M., et al., *Evaluation of commercial agrochemicals as new tools for malaria vector control.* Chimia, 2016. **70**(10): p. 721-721.
19. Lees, R., et al., *A testing cascade to identify repurposed insecticides for next-generation vector control tools: screening a panel of chemistries with novel modes of action against a malaria vector.* Gates open research, 2019. **3**: p. 1464.
20. N'Guessan, R., et al., *Evaluation of indoxacarb, an oxadiazine insecticide for the control of pyrethroid-resistant Anopheles gambiae (Diptera: Culicidae).* Journal of medical entomology, 2007. **44**(2): p. 270-276.
21. Oxborough, R.M., et al., *A new class of insecticide for malaria vector control: evaluation of mosquito nets treated singly with indoxacarb (oxadiazine) or with a pyrethroid mixture against Anopheles gambiae and Culex quinquefasciatus.* Malaria journal, 2015. **14**: p. 1-8.
22. Nannan, L., et al., *Behavioral change, physiological modification, and metabolic detoxification: mechanisms of insecticide resistance.* Kun chong xue bao. Acta entomologica Sinica, 2006. **49**(4): p. 671-679.
23. Smith, L.B., S. Kasai, and J.G. Scott, *Voltage-sensitive sodium channel mutations S989P+ V1016G in Aedes aegypti confer variable resistance to pyrethroids, DDT and oxadiazines.* Pest management science, 2018. **74**(3): p. 737-745.
24. Martin, L.J. and B. Corry, *Locating the route of entry and binding sites of benzocaine and phenytoin in a bacterial voltage gated sodium channel.* PLoS computational biology, 2014. **10**(7): p. e1003688.
25. Tao, E. and B. Corry, *Characterizing fenestration size in sodium channel subtypes and their accessibility to inhibitors.* Biophysical Journal, 2022. **121**(2): p. 193-206.
26. Zhang, Y., et al., *The receptor site and mechanism of action of sodium channel blocker insecticides.* Journal of Biological Chemistry, 2016. **291**(38): p. 20113-20124.
27. Baron, R. and J.A. McCammon, *Molecular recognition and ligand association.* Annual review of physical chemistry, 2013. **64**: p. 151-175.
28. Rydzewski, J. and W. Nowak, *Ligand diffusion in proteins via enhanced sampling in molecular dynamics.* Physics of Life Reviews, 2017. **22**: p. 58-74.
29. Valsson, O., P. Tiwary, and M. Parrinello, *Enhancing important fluctuations: Rare events and metadynamics from a conceptual viewpoint.* Annual review of physical chemistry, 2016. **67**: p. 159-184.
30. Salgado, V. and J. Hayashi, *Metaflumizone is a novel sodium channel blocker insecticide.* Veterinary parasitology, 2007. **150**(3): p. 182-189.
31. Salgado, V., *Slow voltage-dependent block of sodium channels in crayfish nerve by dihydropyrazole insecticides.* Molecular pharmacology, 1992. **41**(1): p. 120-126.
32. Jiang, D., et al., *Open-state structure and pore gating mechanism of the cardiac sodium channel.* Cell, 2021. **184**(20): p. 5151-5162. e11.
33. Shen, H., et al., *Structural basis for the modulation of voltage-gated sodium channels by animal toxins.* Science, 2018. **362**(6412): p. eaau2596.
34. Takagi, K., et al., *Discovery of metaflumizone, a novel semicarbazone insecticide.* Veterinary Parasitology, 2007. **150**(3): p. 177-181.
35. Roditakis, E., et al., *Identification and detection of indoxacarb resistance mutations in the para sodium channel of the tomato leafminer, Tuta absoluta.* Pest management science, 2017. **73**(8): p. 1679-1688.
36. Wang, X.L., et al., *Two novel sodium channel mutations associated with resistance to indoxacarb and metaflumizone in the diamondback moth, Plutella xylostella.* Insect science, 2016. **23**(1): p. 50-58.

37. Jiang, D., et al., *Mutations in the transmembrane helix S6 of domain IV confer cockroach sodium channel resistance to sodium channel blocker insecticides and local anesthetics.* Insect biochemistry and molecular biology, 2015. **66**: p. 88-95.
38. Silver, K.S., et al., *Role of the sixth transmembrane segment of domain IV of the cockroach sodium channel in the action of sodium channel blocker insecticides.* Neurotoxicology, 2009. **30**(4): p. 613-621.
39. von Stein, R.T. and D.M. Soderlund, *Compound-specific effects of mutations at Val787 in DII-S6 of Nav1. 4 sodium channels on the action of sodium channel inhibitor insecticides.* Neurotoxicology, 2012. **33**(5): p. 1381-1389.
40. Rydzewski, J., et al., *Kinetics of huperzine A dissociation from acetylcholinesterase via multiple unbinding pathways.* Journal of Chemical Theory and Computation, 2018. **14**(6): p. 2843-2851.
41. Rydzewski, J. and O. Valsson, *Finding multiple reaction pathways of ligand unbinding.* The Journal of Chemical Physics, 2019. **150**(22): p. 221101.
42. Branduardi, D., F.L. Gervasio, and M. Parrinello, *From A to B in free energy space.* The Journal of chemical physics, 2007. **126**(5): p. 054103.
43. Chovancova, E., et al., *CAVER 3.0: a tool for the analysis of transport pathways in dynamic protein structures.* 2012.
44. Barber, A.F., et al., *Hinge-bending motions in the pore domain of a bacterial voltage-gated sodium channel.* Biochimica et Biophysica Acta (BBA)-Biomembranes, 2012. **1818**(9): p. 2120-2125.
45. Hafeez, M., et al., *Characterization of Indoxacarb Resistance in the Fall Armyworm: Selection, Inheritance, Cross-Resistance, Possible Biochemical Mechanisms, and Fitness Costs.* Biology, 2022. **11**(12): p. 1718.
46. Nehare, S., et al., *Inheritance of resistance and cross resistance pattern in indoxacarb-resistant diamondback moth Plutella xylostella L.* Entomological research, 2010. **40**(1): p. 18-25.
47. Marak, R., et al., *Mode of inheritance of indoxacarb resistance in diamondback moth, Plutella xylostella (L.) and cross resistance to different groups of pesticides.* Phytoparasitica, 2017. **45**(4): p. 549-558.
48. Zhang, S., et al., *Cross-resistance and biochemical mechanisms of resistance to indoxacarb in the diamondback moth, Plutella xylostella.* Pesticide Biochemistry and Physiology, 2017. **140**: p. 85-89.
49. Ramasubramanian, T. and A. Regupathy, *Pattern of cross-resistance in pyrethroid-selected populations of Helicoverpa armigera Hübner (Lep., Noctuidae) from India.* Journal of Applied Entomology, 2004. **128**(9-10): p. 583-587.
50. Achaleke, J., et al., *Esterase-mediated resistance to pyrethroids in field populations of Helicoverpa armigera (Lepidoptera: Noctuidae) from Central Africa.* Pest Management Science: formerly Pesticide Science, 2009. **65**(10): p. 1147-1154.
51. Sun, H., et al., *Characterization of two kdr mutations at predicted pyrethroid receptor site 2 in the sodium channels of Aedes aegypti and Nilaparvata lugens.* Insect Biochemistry and Molecular Biology, 2022. **148**: p. 103814.
52. Hemingway, J., *Efficacy of etofenprox against insecticide susceptible and resistant mosquito strains containing characterized resistance mechanisms.* Medical and veterinary entomology, 1995. **9**(4): p. 423-426.
53. Matsuo, N., *Discovery and development of pyrethroid insecticides.* Proceedings of the Japan Academy, Series B, 2019. **95**(7): p. 378-400.
54. Wu, S., et al., *Molecular basis of selective resistance of the bumblebee BiNav1 sodium channel to tau-fluvalinate.* Proceedings of the National Academy of Sciences, 2017. **114**(49): p. 12922-12927.
55. Usherwood, P., et al., *Mutations in DIIS5 and the DIIS4–S5 linker of Drosophila melanogaster sodium channel define binding domains for pyrethroids and DDT.* Febs Letters, 2007. **581**(28): p. 5485-5492.
56. Panini, M., et al., *Presence and impact of allelic variations of two alternative s-kdr mutations, M918T and M918L, in the voltage-gated sodium channel of the green peach aphid Myzus persicae.* Pest Management Science, 2015. **71**(6): p. 878-884.
57. Criniti, A., et al., *Biochemical and molecular diagnosis of insecticide resistance conferred by esterase, MACE, kdr and super-kdr based mechanisms in Italian strains of the peach potato aphid, Myzus persicae (Sulzer).* Pesticide Biochemistry and Physiology, 2008. **90**(3): p. 168-174.
58. Araújo, R.A., et al., *Pyrethroid resistance in Sitophilus zeamais is associated with a mutation (T929I) in the voltage-gated sodium channel.* Insect Molecular Biology, 2011. **20**(4): p. 437-445.
59. Lee, S.H., et al., *Sodium channel mutations associated with knockdown resistance in the human head louse, Pediculus capitis (De Geer).* Pesticide Biochemistry and Physiology, 2003. **75**(3): p. 79-91.

60. Hodgdon, H.E., et al., *Determination of knockdown resistance allele frequencies in global human head louse populations using the serial invasive signal amplification reaction.* Pest management science, 2010. **66**(9): p. 1031-1040.
61. Sugiura, M., et al., *Novel CONCOMITANT mutations L932F and I936V in the voltage-gated sodium channel and its association with pyrethroid resistance in Culex quinquefasciatus (Diptera: Culicidae).* Journal of Medical Entomology, 2021. **58**(2): p. 798-806.
62. Gao, J.-R., et al., *Increased frequency of the T929I and L932F mutations associated with knockdown resistance in permethrin-resistant populations of the human head louse, Pediculus capitis, from California, Florida, and Texas.* Pesticide Biochemistry and Physiology, 2003. **77**(3): p. 115-124.
63. Hopkins, B. and P. Pietrantonio, *The Helicoverpa zea (Boddie)(Lepidoptera: Noctuidae) voltage-gated sodium channel and mutations associated with pyrethroid resistance in field-collected adult males.* Insect biochemistry and molecular biology, 2010. **40**(5): p. 385-393.
64. Cassanelli, S., et al., *Use of the RFLP-PCR diagnostic test for characterizing MACE and kdr insecticide resistance in the peach potato aphid Myzus persicae.* Pest Management Science: formerly Pesticide Science, 2005. **61**(1): p. 91-96.
65. Brengues, C., et al., *Pyrethroid and DDT cross-resistance in Aedes aegypti is correlated with novel mutations in the voltage-gated sodium channel gene.* Medical and veterinary entomology, 2003. **17**(1): p. 87-94.
66. Kasai, S., et al., *Discovery of super–insecticide-resistant dengue mosquitoes in Asia: Threats of concomitant knockdown resistance mutations.* Science advances, 2022. **8**(51): p. eabq7345.
67. Tan, W.L., et al., *First detection of multiple knockdown resistance (kdr)-like mutations in voltage-gated sodium channel using three new genotyping methods in Anopheles sinensis from Guangxi Province, China.* Journal of medical entomology, 2014. **49**(5): p. 1012-1020.
68. Srisawat, R., et al., *Field-collected permethrin-resistant Aedes aegypti from central Thailand contain point mutations in the domain IIS6 of the sodium channel gene (kdr).* 2012.
69. Stenhouse, S.A., et al., *Detection of the V1016G mutation in the voltage-gated sodium channel gene of Aedes aegypti (Diptera: Culicidae) by allele-specific PCR assay, and its distribution and effect on deltamethrin resistance in Thailand.* Parasites & vectors, 2013. **6**(1): p. 1-10.
70. Chang, C., et al., *A novel amino acid substitution in a voltage-gated sodium channel is associated with knockdown resistance to permethrin in Aedes aegypti.* Insect biochemistry and molecular biology, 2009. **39**(4): p. 272-278.
71. Pang, S., et al., *Low efficacy of delthamethrin-treated net against Singapore Aedes aegypti is associated with kdr-type resistance.* Trop Biomed, 2015. **32**(1): p. 140-50.
72. Li, C.-X., et al., *Relationship between insecticide resistance and kdr mutations in the dengue vector Aedes aegypti in Southern China.* Parasites & vectors, 2015. **8**(1): p. 1-9.
73. Saavedra-Rodriguez, K., et al., *A mutation in the voltage-gated sodium channel gene associated with pyrethroid resistance in Latin American Aedes aegypti.* Insect molecular biology, 2007. **16**(6): p. 785-798.
74. Kawada, H., et al., *Co-occurrence of point mutations in the voltage-gated sodium channel of pyrethroid-resistant Aedes aegypti populations in Myanmar.* PLoS neglected tropical diseases, 2014. **8**(7): p. e3032.
75. Zhou, X., et al., *Knockdown resistance (kdr) mutations within seventeen field populations of Aedes albopictus from Beijing China: first report of a novel V1016G mutation and evolutionary origins of kdr haplotypes.* Parasites & vectors, 2019. **12**: p. 1-16.
76. Punchihewa, R., et al., *Insecticide resistance mechanisms with novel 'kdr'type gene mutations in the tropical bed bug Cimex hemipterus.* Parasites & vectors, 2019. **12**: p. 1-8.
77. Pridgeon, J.W., et al., *Variability of resistance mechanisms in pyrethroid resistant German cockroaches (Dictyoptera: Blattellidae).* Pesticide Biochemistry and Physiology, 2002. **73**(3): p. 149-156.
78. Endersby, N., et al., *Widespread pyrethroid resistance in Australian diamondback moth, Plutella xylostella (L.), is related to multiple mutations in the para sodium channel gene.* Bulletin of entomological research, 2011. **101**(4): p. 393-405.
79. Wei, Y., et al., *Insecticide susceptibility status and knockdown resistance (kdr) mutation in Aedes albopictus in China.* Parasites & Vectors, 2021. **14**(1): p. 1-9.
80. Xu, J., et al., *Multi-country survey revealed prevalent and novel F1534S mutation in voltage-gated sodium channel (VGSC) gene in Aedes albopictus.* PLoS neglected tropical diseases, 2016. **10**(5): p. e0004696.

81. Gao, J.-P., et al., *Correlation between adult pyrethroid resistance and knockdown resistance (kdr) mutations in Aedes albopictus (Diptera: Culicidae) field populations in China.* Infectious diseases of poverty, 2018. **7**(05): p. 37-45.
82. Du, Y., et al., *Identification of a cluster of residues in transmembrane segment 6 of domain III of the cockroach sodium channel essential for the action of pyrethroid insecticides.* Biochemical Journal, 2009. **419**(2): p. 377-385.
83. Kushwah, R.B.S., et al., *A new knockdown resistance (kdr) mutation, F1534L, in the voltage-gated sodium channel of Aedes aegypti, co-occurring with F1534C, S989P and V1016G.* Parasites & Vectors, 2020. **13**: p. 1-12.
84. Katsavou, E., et al., *Identification and geographical distribution of pyrethroid resistance mutations in the poultry red mite Dermanyssus gallinae.* Pest management science, 2020. **76**(1): p. 125-133.
85. He, H., et al., *Identification of a point mutation in the para-type sodium channel gene from a pyrethroid-resistant cattle tick.* Biochemical and biophysical research communications, 1999. **261**(3): p. 558-561.
86. De Beer, B., et al., *High-Resolution Genetic Mapping Combined with Transcriptome Profiling Reveals That Both Target-Site Resistance and Increased Detoxification Confer Resistance to the Pyrethroid Bifenthrin in the Spider Mite Tetranychus urticae.* Biology, 2022. **11**(11): p. 1630.
87. Silva, J.J., C.N. Kouam, and J.G. Scott, *Levels of cross-resistance to pyrethroids conferred by the Vssc knockdown resistance allele 410L+ 1016I+ 1534C in Aedes aegypti.* PLoS Neglected Tropical Diseases, 2021. **15**(7): p. e0009549.
88. Waterhouse, A., et al., *SWISS-MODEL: homology modelling of protein structures and complexes.* Nucleic acids research, 2018. **46**(W1): p. W296-W303.
89. *UniProt: the universal protein knowledgebase in 2021.* Nucleic acids research, 2021. **49**(D1): p. D480-D489.
90. Colovos, C. and T.O. Yeates, *Verification of protein structures: patterns of nonbonded atomic interactions.* Protein science, 1993. **2**(9): p. 1511-1519.
91. Laskowski, R.A., et al., *PROCHECK: a program to check the stereochemical quality of protein structures.* Journal of applied crystallography, 1993. **26**(2): p. 283-291.
92. Madhavi Sastry, G., et al., *Protein and ligand preparation: parameters, protocols, and influence on virtual screening enrichments.* Journal of computer-aided molecular design, 2013. **27**(3): p. 221-234.
93. Kim, S., et al., *PubChem in 2021: new data content and improved web interfaces.* Nucleic acids research, 2021. **49**(D1): p. D1388-D1395.
94. Koes, D.R., M.P. Baumgartner, and C.J. Camacho, *Lessons learned in empirical scoring with smina from the CSAR 2011 benchmarking exercise.* Journal of chemical information and modeling, 2013. **53**(8): p. 1893-1904.
95. Trott, O. and A.J. Olson, *AutoDock Vina: improving the speed and accuracy of docking with a new scoring function, efficient optimization, and multithreading.* Journal of computational chemistry, 2010. **31**(2): p. 455-461.
96. Wu, E.L., et al., *CHARMM-GUI membrane builder toward realistic biological membrane simulations*. 2014, Wiley Online Library.
97. Jo, S., et al., *CHARMM-GUI: a web-based graphical user interface for CHARMM.* Journal of computational chemistry, 2008. **29**(11): p. 1859-1865.
98. Brooks, B.R., et al., *CHARMM: the biomolecular simulation program.* Journal of computational chemistry, 2009. **30**(10): p. 1545-1614.
99. Niklas, B., B. Lapied, and W. Nowak, *In search of synergistic insect repellents: Modeling of muscarinic GPCR interactions with classical and bitopic photoactive ligands.* Molecules, 2022. **27**(10): p. 3280.
100. Phillips, J.C., et al., *Scalable molecular dynamics with NAMD.* Journal of computational chemistry, 2005. **26**(16): p. 1781-1802.
101. Zoete, V., et al., *SwissParam: a fast force field generation tool for small organic molecules.* Journal of computational chemistry, 2011. **32**(11): p. 2359-2368.
102. Humphrey, W., A. Dalke, and K. Schulten, *VMD: visual molecular dynamics.* Journal of molecular graphics, 1996. **14**(1): p. 33-38.
103. Abraham, M.J., et al., *GROMACS: High performance molecular simulations through multi-level parallelism from laptops to supercomputers.* SoftwareX, 2015. **1**: p. 19-25.
104. Tribello, G.A., et al., *PLUMED 2: New feathers for an old bird.* Computer physics communications, 2014. **185**(2): p. 604-613.

105. *Promoting transparency and reproducibility in enhanced molecular simulations.* Nature methods, 2019. **16**(8): p. 670-673.
106. Bussi, G., D. Donadio, and M. Parrinello, *Canonical sampling through velocity rescaling.* The Journal of chemical physics, 2007. **126**(1): p. 014101.
107. Hess, B., *P-LINCS: A parallel linear constraint solver for molecular simulation.* Journal of chemical theory and computation, 2008. **4**(1): p. 116-122.
108. Rydzewski, J., *maze: Heterogeneous ligand unbinding along transient protein tunnels.* Computer Physics Communications, 2020. **247**: p. 106865.
109. Barducci, A., G. Bussi, and M. Parrinello, *Well-tempered metadynamics: a smoothly converging and tunable free-energy method.* Physical review letters, 2008. **100**(2): p. 020603.
110. Tiwary, P. and M. Parrinello, *A time-independent free energy estimator for metadynamics.* The Journal of Physical Chemistry B, 2015. **119**(3): p. 736-742.

11. Summary and future prospects

The presented doctoral dissertation aimed to characterize the molecular basis of repellents and insecticides' action on their target proteins. The results obtained during the implementation of the above-mentioned studies made it possible to achieve the following goals:

- By the precise analysis of the dynamic evolution of residue-reside contact scores, we described the first-stage allosteric pathway of conformational changes in mAChRs in response to agonist binding. This enabled us to design and test the action of the bitopic, photoswitchable compound with a potential repellent activity and reduced mammalian toxicity.
- We compared the binding modes of four peptide toxins from sea anemones on the cockroach voltage-gated sodium channel. Our modeling results were further validated experimentally by electrophysiological investigation of toxins' efficacy on neuronal preparations of *Periplaneta americana*. The different potency of toxins to inhibit the fast inactivation process of insect channels manifested through the prolongation of the action potential, could not be explained by docking energy term but rather the combination of various parameters contributing to the blockage of the channel' S4 helix.
- We found that the most probable entry route of DCJW blocker insecticide to the central cavity of VGSC is *via* the DIII-DIV fenestration. We explain the role of the F1852T mutation found in resistant insects and the increased toxicity of DCJW compared to its bulkier parent compound, indoxacarb. We also indicated the channels' residues contributing to SCBIs and non-ester pyrethroid etofenprox binding that could be involved in the target site cross-resistance.
- We confirmed that computer modeling linked with electrophysiological experiments are effective tools in the understanding of neurotoxin actions at the molecular level. The computational pipeline is ready for further studies of similar systems.

As a part of my doctoral project, we performed docking, MD, and enhanced sampling simulations on pyrethroid insecticide – deltamethrin – binding to the VGSC of *Periplaneta americana*. We described the ligand interactions with the residues carrying

knockdown resistance when mutated. We also investigated the role of fluctuations of the fenestrations shape in deltamethrin action on cockroach channels. Free energy barriers found in the fenestration greatly correlate with mutations found in resistant insects. In collaboration with the team of Prof. Bruno Lapied (University of Angers, France), we conducted an extensive electrophysiological investigation on the synergistic effects of insecticides. We also discovered the biochemical pathway of insects' response to stress caused by insecticide and their novel mechanism of adaptation. The results will be of great importance in insect control. The manuscript is in preparation, we plan to submit it to *Nature*.

Under the NCN Preludium grant, I am working on designing a new class of insecticides with acyl sulfonamide moiety and azobenzene functional group. We target a VSD domain of sodium channel that is less conserved than an inner pore. New compounds will block the arginine residues of S4 helices to inhibit the fast inactivation process thus prolonging the action potentials (the effect observed under treatment with the toxins from sea anemones).

We also plan to investigate in detail the molecular basis of the fast inactivation process. We use the steered MD to get a full picture of the occluding inner pore by the inactivation gate particle. A thorough understanding of this mechanism may result in finding new ways to modulate sodium conductance and thus action potentials.

12. Appendix:

Declarations of co-authors

UNIWERSYTET
MIKOŁAJA KOPERNIKA
W TORUNIU

Katedra Biofizyki
Instytut Fizyki
Prof. dr hab. Wiesław Nowak

April 3rd, 2023

Prof. dr hab. Wiesław Nowak
Department of Biophysics
Faculty of Physics, Astronomy and Informatics
Nicolaus Copernicus University
Grudziadzka 5
87-100 Torun, Poland
wiesiek@umk.pl

To whom it may concern

I hereby declare that my contributions to the articles included in the doctoral thesis of Beata Niklas, MSc were the following:

In Search of Synergistic Insect Repellents: Modeling of Muscarinic GPCR Interactions with Classical and Bitopic Photoactive Ligands,
Molecules 2022, 27 (10), 3280
Conceptualization, methodology, validation, formal analysis, resources, data curation, writing—review and editing, supervision

Interactions of Sea Anemone Toxins with Insect Sodium Channel—Insights from Electrophysiology and Molecular Docking Studies,
Molecules 2021, 26 (5), 1302
Conceptualization, methodology, validation, resources, writing—original draft co-preparation, writing—review and editing, supervision

Toward overcoming pyrethroid resistance in mosquito control: the role of sodium channel blocker insecticides,
Deposited in the bioRxiv (DOI: 10.1101/2023.03.29.534712); submitted for publication in International Journal of Biological Macromolecules (Elsevier, IF= 8.02) on March 29th , 2023
Conceptualization, validation, funding acquisition, project administration, resources, supervision, writing - review & editing

W. Nowak

KATEDRA BIOFIZYKI, Chair of Biophysics
Wydział Fizyki, Astronomii i Informatyki Stosowanej
Instytut Fizyki
UNIWERSYTET MIKOŁAJA KOPERNIKA W TORUNIU
ul. Grudziądzka 5, 87-100 Toruń, Polska
tel. +48 56 611 32 04, NIP: 879-017-72-91, REGON: 000001324
e-mail: wiesiek@umk.pl, strona internetowa: https://www.ifiz.umk.pl/instytut/struktura/kb/

Laboratoire SiFCIR
UPRES EA 2647 / USC INRA 1330
SFR 4207 QUASAV

Institut National de la Recherche Agronomique

To whom it may concern

I hereby declare that my contribution to the article « *In Search of Synergistic Insect Repellents: Modeling of Muscarinic GPCR Interactions with Classical and Bitopic Photoactive Ligands*" by Niklas et al., Molecules 2022, 27 (10), 3280 was: Conceptualization; validation; formal analysis; writing—review and editing; supervision; project administration and the article "*Toward overcoming pyrethroid resistance in mosquito control: the role of sodium channel blocker insecticides*" by Niklas et al. Deposited in the bioRxiv (DOI: 10.1101/2023.03.29.534712) was: Conceptualization; Supervision; Writing - review & editing.

University of Angers, 31/03/2023

Professor B. Lapied

Tél: 02 41 73 54 38 - Fax: 02 41 73 52 15 - e-mail: bruno.lapied@univ-angers.fr
www.med.univ-angers.fr/discipline/labo_neuro/

NICOLAUS COPERNICUS
UNIVERSITY
IN TORUŃ
Faculty of Biological
and Veterinary Sciences

Toruń, 4 kwietnia 2023

dr Milena Jankowska
Uniwersytet Mikołaja Kopernika w Toruniu
Wydział Nauk Biologicznych i Weterynaryjnych
Katedra Fizjologii Zwierząt i Neurobiologii
ul. Lwowska 1, 87-100 Toruń

OŚWIADCZENIE

Oświadczam, że mój udział w realizacji pracy: **Niklas, B.; Jankowska, M.; Gordon, D.; Béress, L.; Stankiewicz, M.; Nowak, W. Interactions of Sea Anemone Toxins with Insect Sodium Channel—Insights from Electrophysiology and Molecular Docking Studies, Molecules 2021, 26 (5), 1302** polegał na przygotowaniu protokołów doświadczeń, walidacji, przeprowadzaniu doświadczeń elektrofizjologicznych, udział w przygotowywaniu pierwszego draftu manuskryptu, jego korekcie i edycji oraz przygotowywaniu wizualizacji zebranych danych.

dr Milena Jankowska

2nd April, 2023

To whom it may concern

I hearby declare that my contribution to the article "Interactions of Sea Anemone Toxins with Insect Sodium Channel—Insights from Electrophysiology and Molecular Docking Studies", Molecules 2021, 26 (5), 1302, was: methodology, validation, resources, writing—review and editing.

Sincerely

Dr. Dalia Gordon
Academic consultant
Weizmann Institute of Science
Dept. of Biomolecular Sciences
The Laboratory of Prof. Mike Fainzilber
Rehovot 76100, Israel

Hannover, 02.11.2022

CERTIFICATION OF CONTRIBUTION

To whom it may concern,

Herewith I certify, that my own scientific contribution to the article "Interactions of Sea Anemone Toxins with Insect Sodium Channel—Insights from Electrophysiology and Molecular Docking Studies" (*Molecules* 26 (5), 1302) was equal to 1 %. I contributed merely the pure sea anemone toxins to this work. I highly appreciate the great work of our first author, and it is a great honor for me that I was invited to be a coauthor in such a distinguished work.

Prof. Dr. László Béress
Department of Internal Medicine, Clinic of Immunology
Division of Experimental and Clinical Peptide Research
Hannover Medical School
30625 Hannover, Germany
Phone:(49)(0)4321-12528

Prof. Dr. László Béress
Färberstraße 28
D-24534 Neumünster
Phone/Fax 49-(0)4321-12528

3 April 2023

Jakub Rydzewski
Institute of Physics
Nicolaus Copernicus University
87-100 Toruń, Poland

Declaration of Contribution

I hereby state that my contribution to the article:

“Toward overcoming pyrethroid resistance in mosquito control: the role of sodium channel blocker insecticides”

deposited on bioRxiv (DOI: 10.1101/2023.03.29.534712) consists of data curation; formal analysis; investigation; methodology; software; validation; writing - review & editing.

Jakub Rydzewski